International Scientific-Technical and Production Journal

The Paton WELDING JOURNAL

December
2007
12

English translation of the monthly «Avtomaticheskaya Svarka» (Automatic Welding) journal published in Russian since 1948

Founders: *E.O. Paton Electric Welding Institute of the NAS of Ukraine*
International Association «Welding»

Publisher: *International Association «Welding»*

Address:
E.O. Paton Electric Welding Institute,
International Association «Welding»,
11, Bozhenko str., 03680, Kyiv, Ukraine
Tel.: (38044) 287 67 57
Fax: (38044) 528 04 86
E-mail: journal@paton.kiev.ua
http://www.nas.gov.ua/pwj

State Registration Certificate
KV 4790 of 09.01.2001

Subscriptions:
$324, 12 issues per year,
postage and packaging included.
Back issues available.

CONTENTS

METHOD FOR EVALUATION OF FRACTURE TOUGHNESS OF WELDED ASSEMBLIES BY COMBINING MATHEMATICAL MODELLING AND MEASUREMENTS ON SMALL-SECTION SPECIMENS

V.I. MAKHNENKO, E.A. VELIKOIVANENKO and **A.P. SEMYONOV**
E.O. Paton Electric Welding Institute, NASU, Kiev, Ukraine

The improved method, being an outgrowth of the B.Z. Margolin method for evaluation of fracture toughness of structural steels through a more exact modelling of deformation processes within the crack zone of a test specimen, is suggested for plotting the K_{IC} versus temperature probability curves for specimens of embrittled steel 15Kh2NMFA, 50 mm thick, based on the results of testing 10 mm thick specimens at a temperature of –100 °C.

Keywords: fracture toughness, probability of fracture by microcleavage, Weibull distribution parameters, stresses in crack zone, characteristics of deformation of material

It is a known fact that reliable data on characteristics of resistance of a material to brittle fracture of the type of fracture toughness K_{IC} for modern structural steels, particularly within the zone of a welded joint, are difficult to generate, as this involves testing of large-section specimens, which is not always possible for «hot spots» of welded structures in operation.

According to the standard, test specimens for evaluation of K_{IC} should have thickness B (length of a crack along its base) at a level of $B > (1.0\text{–}2.5)(K_{IC} / \sigma_y)^2$, where σ_y is the yield strength of a material. At $K_{IC} / \sigma_y > (5\text{–}8)$ mm$^{1/2}$, the required values are $B \geq 50$–150 mm, which is difficult for testing, especially for performing technical examination of welded structures in operation.

In this connection, approaches are gaining acceptance, which are based on replacement of hard-to-perform experimental measurement of K_{IC} by a set of simple measurements with subsequent generation of a desired result by using appropriate recalculation models [1–3, etc.]. These approaches differ in characteristics of a material being measured and in recalculation models.

It might be noted here that researchers are trying to compensate for the lack of experimental information by appropriate mathematical modelling of characteristic phenomena associated with fracture of specimens.

From these standpoints, of special notice is an approach suggested in [4] and further developed in the studies by B.Z. Margolin [5, 6] and others, the point of which is as follows.

Consider a specimen for evaluation of K_{IC} subjected to tension or three-point bending (Figure 1). The stressed state at the crack apex depends upon the loading conditions (load P, geometry of the specimen, test temperature, and properties of the specimen material to resist elasto-plastic deformation). In turn, load P and geometry of the specimen determine the value of stress intensity factor K_I according to the known dependencies [7].

Polycrystalline material of the specimen at the crack apex is assumed to be a set of elementary cells, the ρ size of which corresponds to an average size of grains of the polycrystalline material. The following probability criterion of brittle fracture by the mechanism of initiation of a crack of the type of microcleavage is used for an elementary cell:

$$P(\sigma_1) = 1 - \exp\left[-\left(\frac{\sigma_1 - A}{\sigma_d}\right)^{\eta}\right], \quad (1)$$

where σ_1 is the maximal main stress in a given cell under a load determined by K_I; $A = S_k(\omega)$ or $A = \sigma_{d0}$ (which is higher); σ_{d0}, σ_d and η are the Weibull distribution parameters (assumed to be independent of temperature T and deformation degree ω for the given material); and $S_k(\omega)$ is the tear resistance that depends upon ω.

Hardening parameter ω (Odqvist parameter) is determined by the plastic strain accumulated in loading, i.e.

$$\omega = \int d\varepsilon_i^p, \quad (2)$$

where $d\varepsilon_i^p$ is found at each step in increments of the plastic strains

$$d\varepsilon_i^p = \frac{2}{3}\sigma_i d\lambda, \quad (3)$$

where σ_i is the equivalent stress; $d\lambda$ is the parameter of the Prandtle–Reiss law for elasto-plastic flow of a material associated with the Mises flow condition, i.e. deformation stress $\sigma_s(T, \omega)$ at a given test temperature T also depends upon ω:

$$\sigma_i = \frac{1}{\sqrt{2}}\,[(\sigma_{xx} - \sigma_{yy})^2 + (\sigma_{xx} - \sigma_{zz})^2 + (\sigma_{yy} - \sigma_{zz})^2 + 6(\sigma_{xy}^2 + \sigma_{xz}^2 + \sigma_{yz}^2)\,]^{0.5}, \quad (4)$$

where σ_{xx}, σ_{yy}, σ_{zz}, σ_{xy}, σ_{xz} and σ_{yz} are the components of the stress tensor.

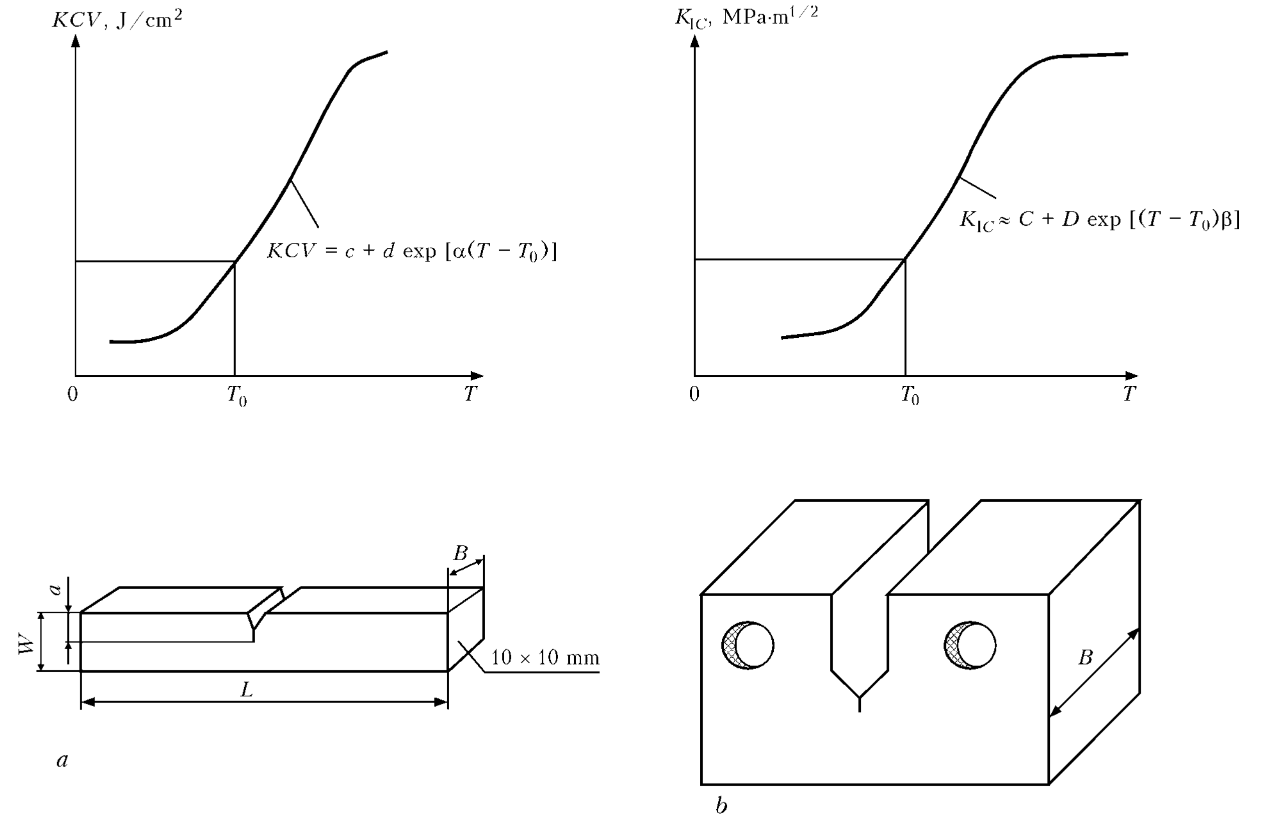

Figure 1. Schematic diagram of the results of impact toughness tests on Charpy specimens (a) and evaluation of K_{IC} on a specimen $B \geq$ $\geq$ 100–150 mm thick (b): T_0, c, d and a — experimental parameters for curve KCV (T); C, D and β — same for curve K_{IC} (T); a — crack depth; L and W — specimen length and height

In a case of i = 1, 2, ..., N cells, the probability that at least in one of them the fracture would occur by the said mechanism is determined by the following expression:

$$P_f(K_I) = 1 - \exp\left[-\sum_i^N \left(\frac{\sigma_1^i - A}{\sigma_d}\right)^\eta\right], \qquad (5)$$

where summation by n is actually made only by the cells, where $\sigma_1^i > A$.

The value of σ_1^i at different stages of testing of a specimen at temperature T can be determined by solving the corresponding boundary value problem of elasto-plastic deformation at the preset geometrical dimensions (Figure 1), elasticity characteristics (E — Young modulus; ν — Poisson's ratio) and deformation stress $\sigma_s(T, \omega)$.

Naturally, this approach for specimens that are similar to those shown in Figure 1 requires the 3-D statement of the deformation problem, allowing for the physical, and geometrical in some cases, non-linearity, which is not that difficult to do now, unlike the time when studies [5, 6] were published. Their authors employed mainly the elastic solution in the context of plane deformation with the corresponding, not very strict, amendments, which artificially allowed for plastic strains at different test temperatures, while this discredits the approach considered and causes strong objections among the critics of this direction.

From this standpoint, the present study is not related to the above simplification in generating the information on σ_1, which provides a substantial increase in its correctness and makes the procedure attractive for practical application. Available software packages of the type of «Ansis», «Sysweld» and «Marc» make it possible to sufficiently effectively derive the solution to the deformation problem through tracing loading on the specimens (see Fi-

Parameters of strain hardening of steel 15Kh2NMFA

Parameter	Ò, °Ñ								
	–196	–100	–60	–20	20	100	200	350	450
D_0, MPa	679/765	635/732	622/718	629/727	590/700	357/740	–/764	537/742	–/586
n	0.49/0.41	0.47/0.36	0.46/0.36	0.49/0.39	0.49/0.43	0.49/0.44	–/0.47	0.50/0.49	–/0.45

Note. Numerator gives data on a specimen in the initial state, and denominator — on a specimen in the embrittled state.

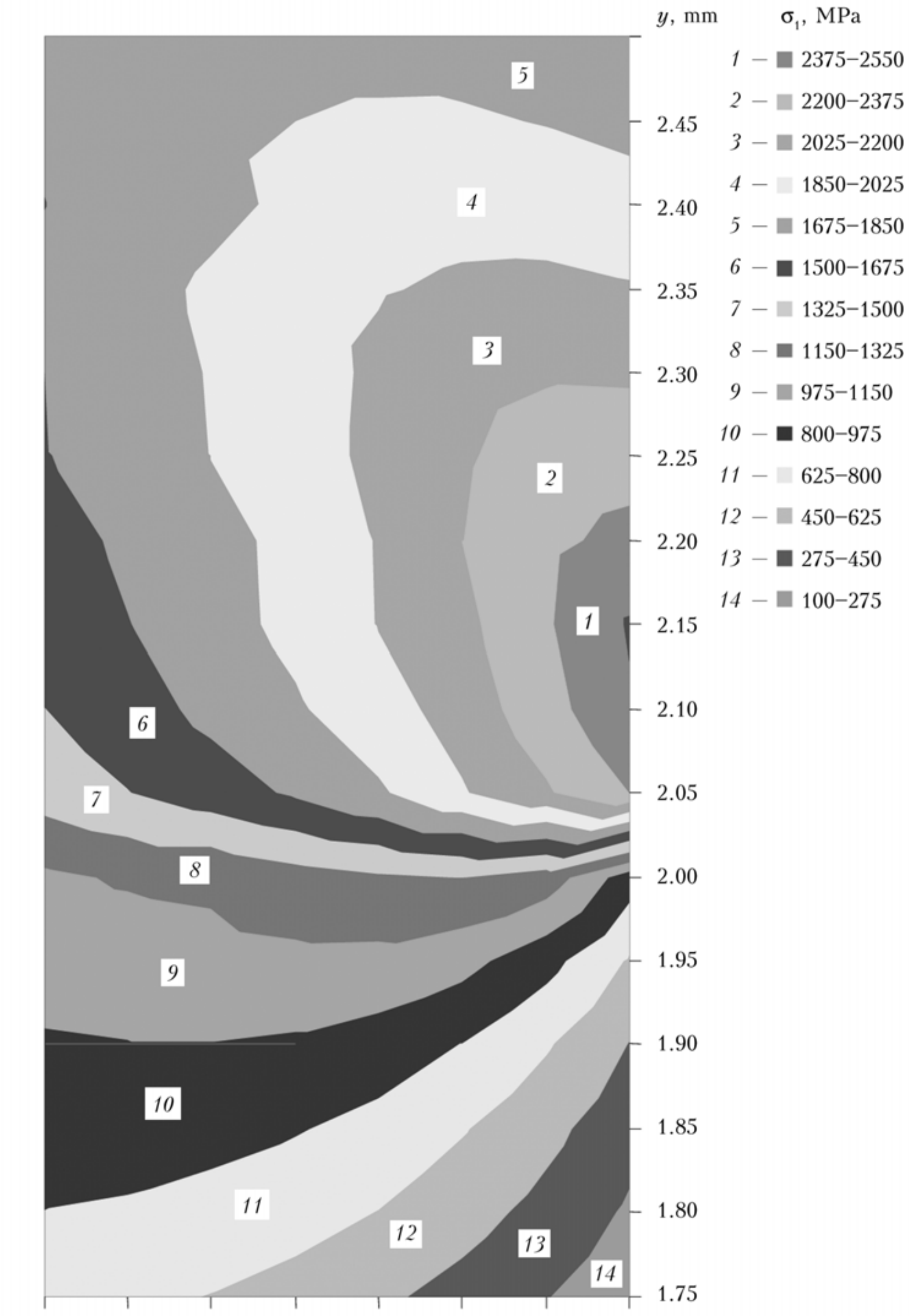

Figure 2, *a*. Results of calculation of σ_1 for specimens with $B = W = 10$ mm at $T = -100$ °C and $K_I = 62$ MPa·m$^{1/2}$ in the vicinity of a crack 2 mm deep for section $z = 0$ (crack apex $y = 2.05$ mm, $P_f = 0.05$)

gure 1) of specific dimensions, by fixing the 3-D field of main stresses σ_1 at each loading step.

As follows from the above-said, the dependence of fracture toughness K_{IC} for probability P_f upon temperature T and specimen thickness B for this structural steel at a given degradation degree can be found by the calculation method through modelling the deformation of a specimen (determination of the fields of σ_1) in combination with a very limited number of the tests (10–12) for the direct estimation of K_{IC} (on small-section specimens at low temperature), in order to generate data on Weibull distribution parameters σ_{d0}, σ_d and η. The latter are determined by the results of scatter of the experimental values of K_{IC} , i.e. at the known values of K_{IC} ($P_f = 0.95$), K_{IC} ($P_f = 0.50$) and K_{IC} ($P_f = 0.05$) for the performed series of the experiments based on the known fields of $\sigma_1(x, y, z)$ using approaches of the highest likelihood method [8].

The E.O. Paton Electric Welding Institute developed a package of calculation algorithms and computer programs for solving both 3-D deformation problem for a case of specimen loading, as shown in Figure 1, and direct and inverse problems associated with calculation of P_f from (5) and evaluation of Weibull distribution parameters σ_{d0}, σd and η.

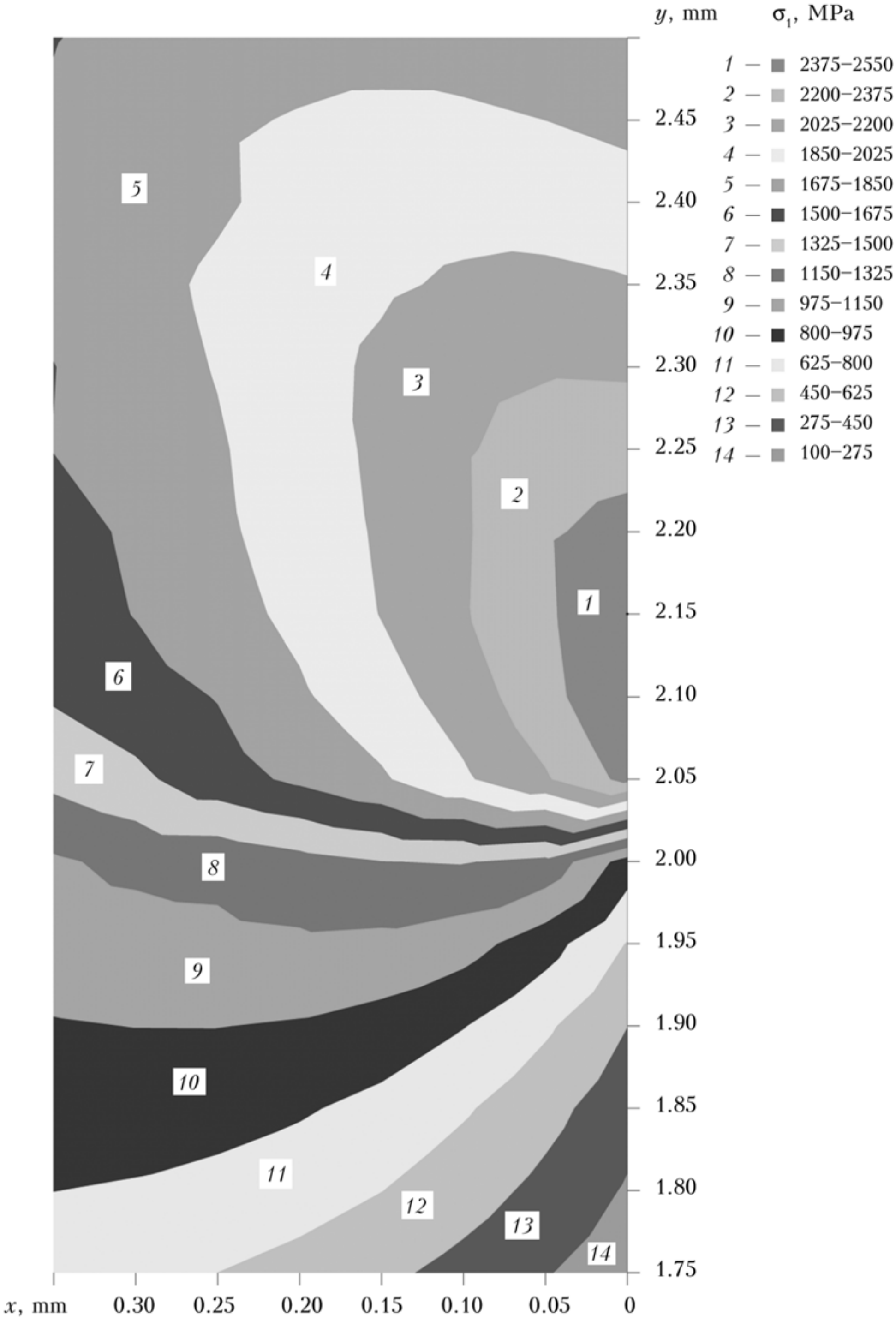

Figure 2, *b*. The same as in Figure 1, *a*, but for section $z = 2.5$ mm

Consider now the results of application of this development for the specimens subjected to three-point bending (see Figure 1, *b*). Because of symmetry, investigations were limited to a calculation area of $0 \le z \le B / 2$, $0 \le x \le L / 2$, $0 \le y \le W$.

To relate K_I and load P at the set values of a, B and W, the use was made of relationship [7] at $L = 4W$

$$K_I = \frac{6P\sqrt{a}}{W}\,[1.93 - 3.07(a/W) + 14.53(a/W)^2 - 25.11(a/W)^3 + 25.8(a/W)^4]. \quad (6)$$

The investigations were conducted on specimens of casing steel 15Kh2NMFA in the initial and embrittled states, and it was assumed that $\rho = 0.05$ mm.

Deformation stress $\sigma_s(T, \omega)$ or proof stress at a given temperature, allowing for strain hardening, was calculated, like in study [9], using the following equation:

$$\sigma_s(T, \omega) = r - c(T + 273) + b \exp[h(T + 273)] + D_0\omega^n, \quad (7)$$

where r, c, b and h are the material constants independent of temperature T; D_0 and n are the values

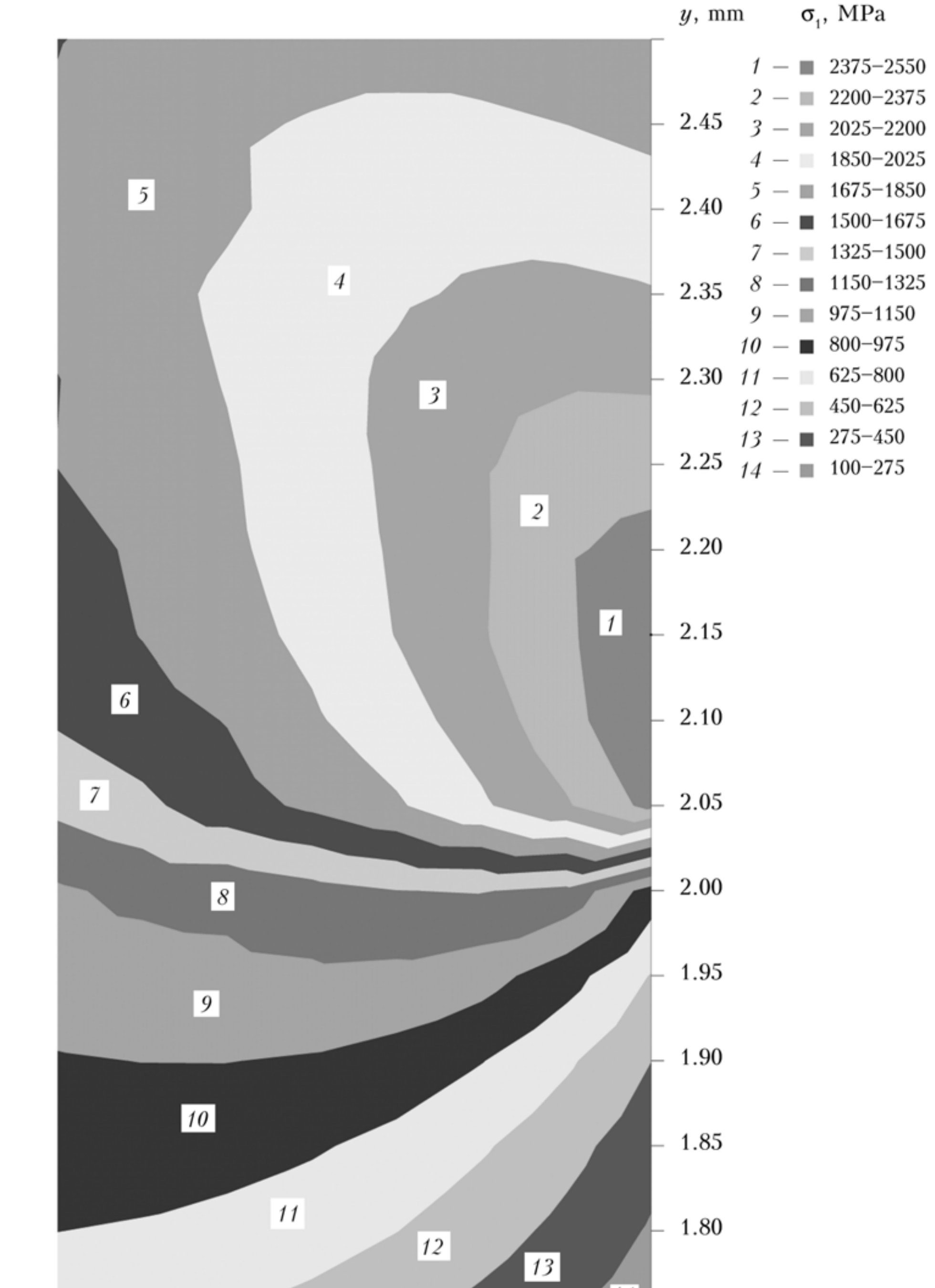

Figure 2, *c*. The same as in Figure 1, *a*, but for section $z = 4.95$ mm

that determine the degree of strain hardening and are the functions of temperature.

According to study [9], $r = 510$ MPa, $c = 0$, $b = 1083$ MPa and $h = 9.309\cdot10^{-3}$ 1 / K for the above steel in the initial state; and $r = 867$ MPa, $c = 0.0305$ MPa·1 / K, $b = 975$ MPa and $h = 1.04\cdot10^{-2}$ 1 / K for the steel in the embrittled state.

The D_0 and n values given in the Table were taken from study [9]. The values of critical stress S_{cr} for the above steel were assumed to depend upon the strain hardening, according to [9], in the following form:

$$S_{cr}(\omega) = [C_1^* + C_2^2 \exp(-D_*\omega)]^{-0.5}, \tag{8}$$

where the constants are given for the initial state ($C_1^* = 2.01\cdot10^{-7}$ MPa^{-2}, $C_2^* = 3.90\cdot10^{-7}$ MPa^{-2}, $D_* = 1.71$) and for the embrittled state ($C_1^* = 1.92\cdot10^{-7}$ MPa^{-2}, $C_2^* = 3.04\cdot10^{-7}$ MPa^{-2}, $D_* = 2.92$) of the steel. Accordingly, $S_{cr}(0) = 1420$ MPa at $\omega = 0$, and $S_{cr}^{max} = 2282$ MPa at $\omega \to \infty$.

In fact, S_{cr}^{max} can be achieved at $\omega = 3 / D_*$, which corresponds to $\omega = 1.71 = 171$ % in the initial state

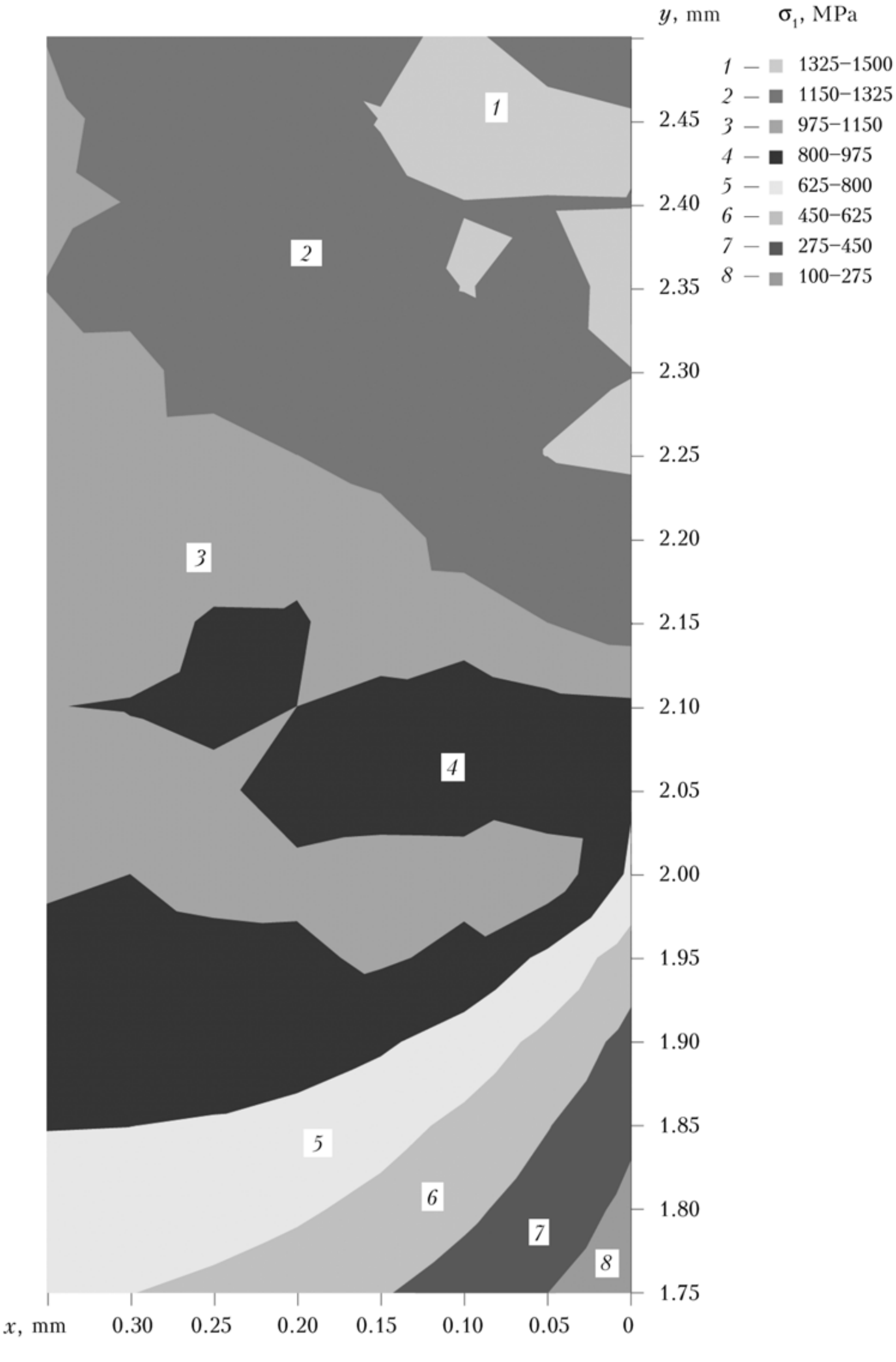

Figure 2, *d*. The same as in Figure 1, *a*, but for section z = 5.00 mm

of the steel, and at 1.027 = 102.7 % in the embrittled state.

According to the data of study [9], parameter σ_{d0} in a local criterion of microcleavage (1) is at a level of $r + b$, i.e. it is equal to 1593 MPa for the initial state of the steel considered, and 1842 MPa for the embrittled state.

Therefore, the condition of local criterion (1), $\sigma_1 > A$, turn into $\sigma_1 > \sigma_{d0}$, if the ω value is lower than the determined values of ω = 0.436 (initial state of the steel) and ω = 0.338 (embrittled state), and into $S_{cr}(\omega)$ at the high values of the strain hardening parameter (high plastic strains).

In other words, at the developed plastic flow (high values of $S_{cr}(\omega)$), other conditions being equal, the probability exists that the given value of K_I (load P) is critical and decreases, which is confirmed by practice.

The above-said was taken into account in processing the experimental data generated for small-section specimens (10 × 10 mm) in the embrittled state at three-point bending and temperature T = –100 °C:

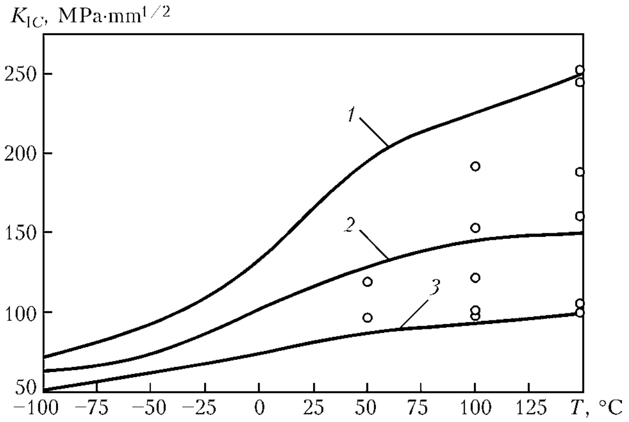

Figure 3. Calculation curves for probability values of $K_{IC}(T)$: *1* — P_f = 0.95; *2* — 0.50; ○ — experimental data

$$K_{IC} = 62 \text{ MPa·m}^{1/2} \text{ at } P_f = 0.05;$$
$$K_{IC} = 83.5 \text{ MPa·m}^{1/2} \text{ at } P_f = 0.50;$$
$$K_{IC} = 101 \text{ MPa·m}^{1/2} \text{ at } P_f = 0.95.$$

Figure 2 shows the results of calculation of main stresses σ_1 for the specimen under consideration at K_{IC} = 62 MPa·m$^{1/2}$, which corresponds to fracture probability P_f = 0.05 at different sections and z = = const. It can be concluded from the given data that the stressed state varies through thickness of the specimen from most rigid at $z = 0$ in the $z = 0$ symmetry plane to softest on the free surface at $z = B / 2 = 5$ mm. Characteristically, the quantity of elementary cells with a volume of $\Delta z \times \Delta x \times \Delta y = (0.05 \text{ mm})^3$, for which, as shown in Figure 2, the microcleavage condition of $\sigma_1 > A \approx 1843$ MPa is satisfied, decreases with increase in distance from the symmetry plane. Thus, at $z = 0$ the number of such volumes is 44 (Figure 2, *a*), at z = 4.95 mm — 19 (Figure 2, *c*), and at z = 5 mm — 0 (Figure 2, *d*).

Naturally, the growth of the P_f and K_{IC} values leads to increase in the quantity of elementary volumes. The values of P_f^{calc} were calculated on the basis of values obtained for P_f (0.05, 0.50 and 0.95) from dependence (5) at different combinations of Weibull parameters η and σ_d at σ_{d0} = 1842 MPa and $S_{\text{cr}}(\omega)$ from (8). The value of $E = \sum_{P=0.05}^{0.95} (P_f - P_f^{\text{calc}})^2$ was determined for each combination. The combination of parameters σ_d and η was found, at which E had a minimal value. This yielded $\eta = 11.2$ and σ_d = = 1715 MPa at σ_{d0} = 1842 MPa and $S_{\text{cr}}(\omega)$ from (8).

The probability curves for K_{IC} at a temperature of –100 to 150 °C were calculated using the above data for the specimen with a section of $B = W = 50$ mm, a = 15 mm and L = 220 mm (Figure 3). The data obtained are in a sufficiently good agreement with the experimental data of [9] in a range of working temperatures (T > 50 °C) for the embrittled material of casing of the WWER-1000 type reactors.

Characteristically, the above peculiarity in distribution of stresses σ_1 in a small-section specimen of the wire type persists also for a large-section specimen, e.g. no conditions exist for initiation of brittle fracture on the $z = B / 2$ free surface. A brittle crack may propagate onto this surface, while its initiation occurs inside a specimen at $z < B / 2$.

CONCLUSIONS

1. The developed numerical methods, as well as the current state of computer facilities make it possible to employ a more general approach to implementation of the method suggested in studies [4–6, 9] for evaluation of fracture toughness K_{IC} of structural steels of the 15Kh2NMFA type.

2. Knowledge of the kinetics of deformation of specimens depending upon the load at constant temperature T and corresponding characteristics E, ν and $\sigma_s(T, \omega)$ enables evaluating the field of main stresses $\sigma_1(x, y, z)$ for the probability values of K_{IC}, and it is on this basis that the probability of brittle fracture in elementary cells of a specimen within the crack apex zone is determined.

3. The probability parameters of brittle fracture of elementary cells with a volume of σ_{d0}, σ_d and η can be determined, and the dependence of the probability values of K_{IC} upon the temperature can be derived from the experimental values of K_{IC} obtained at one, sufficiently low temperature on small-section specimens at the presence of the corresponding fields of stresses $\sigma_1(x, y, z)$.

1. Makhnenko, V.I. (2006) *Safe service life of welded joints and assemblies of modern structures.* Kiev: Naukova Dumka.
2. Ritchie, R.O., Knott, J.E., Rice, J.R. (1975) On the relation between critical tensile stress and fracture toughness in mild steel. *J. Mech. Phys. Solids*, **21**, 395–410.
3. *VBN V.2.3-000182001.04--2000*: Calculations of strength of operational main pipelines with defects. Kiev: Gosneftegazprom.
4. Beremin, F.M. (1983) A local criterion for cleavage fracture of a nuclear pressure vessel steel. *Metallurgical Transaction*, **144**, 1277–2287.
5. Margolin, B.Z., Karzov, G.P., Shvetsova, V.A. (1977) Brittle fracture of nuclear pressure vessel steels. Part 2: Prediction of fracture toughness. *Int. J. Pressure Vessels Piping*, **72**, 89–96.
6. Margolin, B.Z., Gulenko, A.G., Shvetsova, V.A. (1988) Improved probabilistic model for fracture toughness prediction based for nuclear pressure vessel steels. *Ibid.*, **75**, 843--855.
7. (1988) *Fracture mechanics and strength of materials*: Refer. Book. Vol. 2: Savrukh, M.P. Stress intensity factors for bodies with cracks. Ed. by V.V. Panasyuk. Kiev: Naukova Dumka.
8. Korn, G., Korn, T. (1968) *Handbook on mathematics for scientists and engineers.* Moscow: Nauka.
9. Margolin, B.Z., Shvetsova, V.A., Gulenko, A.G. et al. (2002) Prediction of crack resistance of casing reactor steel on the basis of the «Master curve» conception and probabilistic model. *Problemy Prochnosti*, **1**, 5--21.

MATHEMATICAL MODEL OF ARC PLASMA GENERATED BY PLASMATRON WITH ANODE WIRE

M.Yu. KHARLAMOV[1], **I.V. KRIVTSUN**[2], **V.N. KORZHIK**[2], **S.V. PETROV**[2] and **A.I. DEMIANOV**[2]
[1]V. Dal East-Ukrainian National University, Lugansk, Ukraine
[2]E.O. Paton Electric Welding Institute, NASU, Kiev, Ukraine

Mathematical model has been developed, describing turbulent flow of the electric arc plasma and formation of the plasma jet under conditions of plasma-arc spraying. Detailed analysis of the effect of working parameters of a plasmatron using an anode wire and conditions of blowing about a low-turbulent plasma jet it generates with a laminar gas flow on electric parameters of the arc discharge, thermal and gas-dynamic properties of the plasma flow has been conducted on the basis of numerical modelling.

K e y w o r d s : electric arc spraying, wire material, arc plasmatron, mathematical model, software, characteristics of plasma flow

Methods based on utilisation of the electric arc for thermal spraying of coatings have gained wide acceptance in modification of surfaces of machine parts and mechanisms. Currently, one of the most advanced methods providing high-quality coatings is supersonic electric arc spraying of wire materials in a flow of natural gas plus air combustion products [1, 2]. At the same time, modern engineering imposes increasingly high requirements on the coatings, which can be met only on the basis of new approaches. These are, e.g. the requirements for ensuring a near-zero porosity, necessary strength of a coating close to that of a compact material, minimal losses in spraying in a case of using expensive materials and large volumes of production of coated parts, precision of the process, and reproducibility of quality indices in long-time operation of the equipment. An example can be the process of spraying molybdenum or amorphous coatings on synchromesh rings of automatic lines.

The process of plasma-arc wire spraying using the argon arc blown about with an intensive cocurrent air flow also holds promise for addressing the above problems. In this case, the arc burns between the tungsten cathode blown about with a low-rate argon flow and the consumable current-conducting wire fed behind the exit section of the double nozzle of a plasmatron, air being fed into the gap between the nozzles. This process is characterised by the fact that melting and jet flowing of a wire material occur in the shielding atmosphere of argon, while atomisation of the melt and acceleration of the dispersed particles take place in the plasma jet compressed with the cocurrent air flow emitted from the annular gap between the plasmatron nozzles.

As a result, the process provides minimal evaporation losses of the wire material and its saturation with air oxygen and nitrogen, optimal particle size composition of the dispersed phase, near-sonic velocity of the spraying material particles reached at the moment of their incidence on the substrate, maximal possible volume concentration of the spraying particles, and minimal opening angle of the two-phase flow, amounting to no more than a few degrees. This creates preconditions for bringing the resulting coatings to the modern competitive level.

When upgrading designs of the plasmatrons with an anode wire and selecting rational parameters for their operation, it is very important to have the possibility to predict characteristics of the plasma and two-phase flows being formed. These problems can be successfully solved through development of appropriate physical-mathematical models and software for their computer implementation and numerical modelling of the arc plasma flows being studied.

There are many studies [3–6] dedicated to investigation of the arc discharge and its utilisation for heating and acceleration of gas using arc plasma generators. However, most publications consider only the indirect-action electric arc burning inside the anode nozzle of the plasmatron. The processes of thermal, gas-dynamic and chemical interaction of the plasma jet with the backing gas flow and ambient gas environment, which accompany plasma spraying of the anode wire, have been insufficiently studied as yet. This makes it necessary to develop a unified physical-mathematical model of the above processes, which can be applied for a wide range of plasma technologies and account for interaction of the electric arc and plasma jet with a backing gas flow. And it is this development that was the purpose of this study.

Modelling of the process of formation of the plasma flow was performed under the following conditions (Figure 1). The DC arc burns between the refractory water-cooled cathode and current-conducting wire located behind the exit section of the plasmatron nozzle. The plasma gas fed into the nozzle at volume flow rate G_1 is heated by the electric arc and flows out of the electrode nozzle with radius R_n. An exposed region of the discharge (outside the plasma-shaping channel) is blown about with the gas at volume flow rate G_2, which is fed through annular channel $R_1 \le r \le R_2$ at

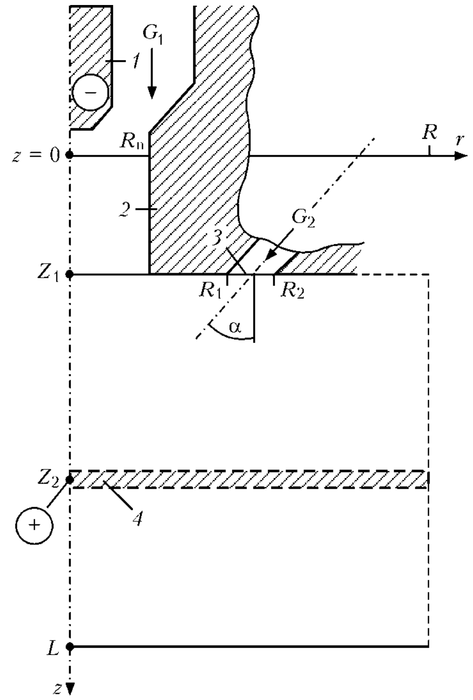

Figure 1. Schematic of calculation region of plasmatron: *1* — refractory cathode; *2* — plasmatron nozzle; *3* — channel for feeding the backing gas; *4* — anode wire

angle α to the plasmatron axis. The ambient pressure is atmospheric. The anode wire is located at distance Z_2 from the beginning of the calculation region. It is assumed that further on the no-current plasma has an inertia motion (at $z > Z_2$).

Therefore, the calculation region can be conditionally subdivided into three regions (see Figure 1) for theoretical analysis of the processes of heating and motion of gas under conditions of plasma-arc spraying: flowing of the arc plasma inside the plasmatron nozzle ($0 \le z \le Z_1$), external flowing of the arc plasma and its interaction with the backing gas flow ($Z_1 \le z \le Z_2$), and inertia motion of the no-current plasma ($z > Z_2$).

Plasmatrons of the type under consideration provide for purging of small amounts of the plasma gas (argon). As a rule, they realise a low-turbulent mode of the plasma flow, as viscosity of the gas grows with increase in temperature. So, the subjects of the investigations are addition of the cocurrent laminar flow of the backing gas into the exposed region of the plasma flow and its interaction with the low-turbulent plasma jet.

Make the following assumptions for mathematical description of the processes occurring in formation of the plasma arc and emission of the arc plasma from the plasmatron nozzle:

• the plasma system under consideration has a cylindrical symmetry, while the occurring processes are assumed to be stationary;

• the backing gas is fed axi-symmetrically through the annular channel, and flow of this gas is assumed to be laminar;

• the plasma is in the state of local thermodynamic equilibrium, and natural radiation of the plasma is volumetric;

• the main mechanism of heating of the plasma is the Joule heat generation (energy of the pressure forces and viscous dissipation can be ignored), and energy transfer in the plasma occurs as a result of thermal conductivity and convection (natural convection is ignored);

• the plasma flow is viscous and sub-sonic, and the flow mode is turbulent;

• there are no external magnetic fields.

As in plasmatrons of the design considered the gas flows primarily in the axial direction, and radial gradients of temperature and velocity are much higher than the axial ones, we will use an approximation of the boundary layer for calculation of thermal and gas-dynamic characteristics of the plasma [7]. Assuming that turbulence is hydrodynamic (i.e. ignoring pulsations of electromagnetic values) and considering the pressure pulsations to be low, we can show that the system of MHD equations in an approximation of the turbulent boundary layer for the time averaged values of temperature and velocity of the plasma has the following form [6, 8]:

$$\frac{\partial}{\partial z}(\rho u) + \frac{1}{r}\frac{\partial}{\partial r}(r\rho\bar{v}) = 0, \qquad (1)$$

$$\rho\left(u\frac{\partial u}{\partial z} + \bar{v}\frac{\partial u}{\partial r}\right) = \frac{1}{r}\frac{\partial}{\partial r}\left(r\bar{\eta}\frac{\partial u}{\partial r}\right) - \frac{\partial}{\partial z}\left(p + \mu_0\frac{H^2}{2}\right), \qquad (2)$$

$$\rho C_p\left(u\frac{\partial T}{\partial z} + \bar{v}\frac{\partial T}{\partial r}\right) = \frac{1}{r}\frac{\partial}{\partial r}\left(r\bar{\chi}\frac{\partial T}{\partial r}\right) + \sigma E^2 - \psi, \qquad (3)$$

where T is the averaged temperature of the plasma; $\bar{v} = (\rho v + \rho' v')/\rho$ (v and ρ are the averaged radial velocity and density of the plasma, respectively; ρ' and v' are the pulsations of the density and radial velocity); u is the averaged axial velocity of the plasma; p is the pressure; C_p is the specific heat under constant pressure; σ is the specific thermal conductivity of the plasma; ψ is the volume power density of natural radiation; $\bar{\eta}$ and $\bar{\chi}$ are the total coefficients of the dynamic viscosity and thermal conductivity of the plasma, respectively (sum of the molecular and turbulent viscosity and thermal conductivity, respectively); E is the axial component of intensity of the electric field; μ_0 is the universal magnetic constant; and H is the azimuthal component of the magnetic field of the arc current:

$$H = \frac{1}{r}E\int_0^r \sigma r dr. \qquad (4)$$

Within the framework of the boundary layer approximation used, the axial component of intensity of the electric field of the arc is almost constant across the section of the channel [6], and determined from the condition of conservation of the total current:

$$I = 2\pi E\int_0^{R_\sigma(z)} \sigma r dr, \qquad (5)$$

where $R_\sigma(z)$ is the radius of the current-conducting region.

Given that conductivity of the plasma outside the current-conducting region is almost equal to zero, radius of the calculation region can be used as an upper limit of integration in formula (5), i.e. $R_\sigma(z) = R_n$ at $0 \le z \le Z_1$, and $R_\sigma(z) = R$ at $z > Z_1$ (see Figure 1).

The distribution of pressure within the nozzle channel is determined with allowance for the magnetic component of the pressure:

$$p = p_{\text{ext}} - \int_z^{Z_1} \frac{dp_n}{dz}\, dz + \mu_0 E \int_r^{R_n} \sigma H dr, \tag{6}$$

where p_{ext} is the ambient pressure. The gradient of gas-static pressure, dp_n / dz, in the boundary layer approximation is also constant across the section of the channel [7], and can be determined from the condition of conservation of the total mass flow rate of the plasma gas:

$$\rho_0 G_1 = 2\pi \int_0^{R_n} \rho u r dr, \tag{7}$$

where ρ_0 is the mass density of the gas under normal conditions.

Pressure in the exposed region of the discharge ($z > Z_1$) can be determined using the following expression:

$$p = p_{\text{ext}} + \mu_0 E \int_r^{R} \sigma H dr. \tag{8}$$

The system of equations (1) through (8) is supplemented with the following relationships:

$$\begin{gathered} \rho = \rho(T, p), \quad C_p = C_p(T, p), \\ \chi = \chi(T, p), \quad \eta = \eta(T, p), \\ \sigma = \sigma(T, p), \quad \psi = \psi(T, p), \end{gathered} \tag{9}$$

which determine dependencies of thermodynamic characteristics, molecular transfer coefficients and optical properties of the plasma upon the temperature and pressure. Detailed tables of the said values for the plasma gases employed are given, e.g. in studies [6, 9].

The same system of the gas-dynamic equations can also be used for description of the no-current (inertia) region of the plasma flow behind the wire ($z > Z_2$) in the approximation of the turbulent boundary layer, assuming that $E = H = 0$.

To close the system of equations (1) through (3), it is necessary to set relationships for determination of turbulent components of the transfer coefficients. The coefficients of dynamic viscosity and thermal conductivity of the plasma used in the above equations have the following form:

$$\overline{\eta} = \eta + \eta_t, \quad \overline{\chi} = \chi + \chi_t, \tag{10}$$

where η and χ are the coefficients of molecular viscosity and thermal conductivity; and η_t and χ_t are the coefficients of turbulent viscosity and thermal conductivity.

The two-parameter k–ε model [10] widely applied in the world practice was used to describe turbulence. Distinctive features of the model include allowance for prehistory of the flow and commonness for different conditions of the flow. With this model, the coefficients of turbulent viscosity and thermal conductivity can be determined by the following formulae:

$$\eta_t = \frac{C_\mu \rho \overline{k}^2}{\varepsilon}, \quad \chi_t = \eta_t \frac{C_p}{\mathrm{Pr}_t}, \tag{11}$$

where $\overline{k}$ and ε are the kinetic energy and rate of dissipation of turbulence, respectively; C_μ is the empirical constant equal to 0.09; and Pr_t is the Prandtl number of turbulence, which is selected according to recommendations [11] or assumed to be equal to one [6].

The first relationship (11) is closed by the transfer equations for the kinetic energy of turbulence and dissipation rate:

$$\rho\left(u\frac{\partial \overline{k}}{\partial z} + \overline{v}\frac{\partial \overline{k}}{\partial r}\right) = \frac{1}{r}\frac{\partial}{\partial r}\left[r\left(\eta + \frac{\eta_t}{\mathrm{Pr}_k}\right)\frac{\partial \overline{k}}{\partial r}\right] + S - \rho\varepsilon, \tag{12}$$

$$\begin{gathered} \rho\left(u\frac{\partial \varepsilon}{\partial z} + \overline{v}\frac{\partial \varepsilon}{\partial r}\right) = \frac{1}{r}\frac{\partial}{\partial r}\left[r\left(\eta + \frac{\eta_t}{\mathrm{Pr}_\varepsilon}\right)\frac{\partial \varepsilon}{\partial r}\right] + \\ + C_1 S \frac{\varepsilon}{\overline{k}} - C_2 \rho \frac{\varepsilon^2}{\overline{k}}, \end{gathered} \tag{13}$$

where $S = \eta_t \left(\frac{\partial u}{\partial r}\right)^2$ is the source term; C_1, C_2, Pr_ε and Pr_k are the constants of the k–ε model of turbulence equal to 1.44, 1.92, 1.3 and 1.0, respectively.

The following boundary and initial (starting) conditions were set for solving the system of differential equations (1) through (3), (12) and (13). Conditions given below were assumed to be valid for the axis of symmetry ($r = 0$):

$$\frac{\partial T}{\partial r} = 0, \quad \frac{\partial u}{\partial r} = 0, \quad v = 0, \quad \frac{\partial \overline{k}}{\partial r} = 0, \quad \frac{\partial \varepsilon}{\partial r} = 0. \tag{14}$$

Condition of «adherence» was specified, and cooling wall temperature T_w was set for the channel wall (at $r = R_n$ and $0 \le z \le Z_1$), i.e.

$$u = 0, \quad T = T_w. \tag{15}$$

To set the $\overline{k}$ and ε values in the vicinity of the channel wall, it is necessary to use the wall function [10, 12] by defining the above values as follows:

$$\overline{k} = \frac{u_*^2}{\sqrt{C_\mu}}, \quad \varepsilon = \frac{u_*^3}{k_0(R_n - r)}, \tag{16}$$

where $k_0 = 0.41$; and u_* is the solution of the transcendental equation (logarithmic law of the wall)

$$\frac{u}{u_*} = \frac{1}{k_0} \ln\left(\frac{\Lambda \rho u_* (R_n - r)}{\eta}\right); \tag{17}$$

$\Lambda = 9.0$ is the parameter of roughness of the wall.

Expressions (16) and (17) are used to correctly allow for a viscous sub-layer in determination of $\overline{k}$ and ε in the wall region, i.e. at $y^+ =$

$= \rho(R_n - r)u_*/\eta < f^+$, where f^+ is selected from a range of 20 to 100 [12]. Equations (12) and (13) of the completely developed turbulent flow are used to describe the internal region of the flow ($y^+ \geq f^+$).

Conditions of smooth interfacing with the environment are assumed to take place at the external boundary of the calculation region (exposed region):

$$T = T_{ext}, \quad u = 0, \quad \bar{k} = 0, \quad \varepsilon = 0, \tag{18}$$

where T_{ext} is the temperature of the environment.

Distributions of the velocity of the plasma gas, values $\bar{k}$ and ε [10] and current density in the cathode region [13, 14] are set as initial conditions for the inlet section of the plasma-shaping channel ($z = 0$):

$$u(r,\ 0) = u_0 \left[1 - \left(\frac{r}{R_n}\right)^n\right], \tag{19}$$

$$\bar{k}(r,\ 0) = i_t(u^2 + \bar{v}^2), \quad \varepsilon(r,\ 0) = 3\,\frac{\bar{k}(r,\ 0)^{3/2}}{R_n}, \tag{20}$$

$$j(r,\ 0) = j_0 e^{-r/r_c}, \tag{21}$$

where $n = 15$; u_0 is selected from the condition of conservation of the mass flow of the plasma gas through the plasmatron nozzle (7); $i_t = 0.003$ is the intensity of turbulence; j is the electric current density; j_0 is the constant depending upon the amperage ($j_0 = 1.2 \cdot 10^8$ A / m^2 at $I = 200$ A [14]); r_c is the radius of the cathode region of the arc determined from the condition of conservation of the total current (5) and Ohm's law:

$$j = \sigma E. \tag{22}$$

Temperature of the plasma gas in the initial section is selected from an empirical dependence of the current density near the cathode (21) using dependence $\sigma = \sigma(T, p)$ and relationship (22). In this case, electric field intensity E at $z = 0$ is assumed to be independent of coordinate r and corresponding to j_0 and $\sigma(T_c)$, where T_c is the maximal temperature of the plasma near the cathode surface, which is approximated according to experimental data [14] for a range of $I = 100$–300 A by polynomial

$$T_c(I) = -250 \cdot 10^{-4} I^2 + 32.5I + 15300. \tag{23}$$

The boundary conditions at the channel outlet for feeding the backing gas (at $z = Z_1$ and $R_1 \leq r \leq R_2$) are set allowing for assumptions of the character of flow of this gas. In this case, temperature of the gas is assumed to be equal to ambient temperature T_{ext}, and components of its rate are described by model dependencies

$$u = u_1 \left[1 - \left(\frac{2r}{R_1 + R_2}\right)^2\right], \quad \bar{v} = u \operatorname{tg} \alpha, \tag{24}$$

where u_1 is selected from the condition of conservation of the total rate of the gas flowing through the channel considered

$$\rho_0 G_2 = 2\pi \int_{R_1}^{R_2} \rho u r dr. \tag{25}$$

The boundary conditions for $\bar{k}$ and ε at the outlet of the channel for feeding the backing gas are selected from the dependencies similar to (20) according to condition (24).

The problem posed was solved numerically by the finite difference method [15, 16]. The use was made of the main difference scheme for integration of the systems of equations of the type of the boundary layer equations [17]. Second-order differential equations (2), (3), (12) and (13) were approximated according to the implicit two-layer six-point difference scheme, and first-order equation (1) — according to the explicit four-point difference scheme. The resulting algebraic system of difference equations was solved by the sweep method using iterations.

Corresponding software was developed on the basis of the resulting calculation scheme, and numerical analysis of characteristics of the low-turbulent flow of the argon plasma generated by the plasmatron with an anode wire under different conditions of its operation was conducted. Thermal and gas-dynamic characteristics of this plasma were calculated both for the arc region of the flow, i.e. from the plasmatron cathode to the anode wire, and for the inertia region, i.e. in the no-current plasma jet. The stationary plasma-arc flow blown about with the axi-symmetric annular flow of cold gas, and flow into the stationary environment (submerged jet) under the atmospheric pressure were studied.

Parameters of the plasmatron and its working conditions selected for all the calculations were as follows: radius and length of the nozzle channel — 1.5 and 3.0 mm, respectively; location of the anode wire — at $z = Z_2 = 9.3$ mm; annular channel for feeding the gas blowing about the flow — having in outlet section an external radius of 4.78 mm and internal radius of 7.22 mm in its exit section, and inclined at an angle of 37.5° to the plasmatron symmetry axis (see Figure 1); temperature of cold walls of the channels and surrounding gas — 300 K; range of variations in the arc current — $I = 160$–260 A; plasma gas (argon) flow rate — $G_1 = 1.0$–1.5 m^3 / h; and backing gas (argon) flow rate — $G_2 = 20$ (0) m^3 / h. Length of the external part of the calculation region, L, was assumed to be equal to 250 mm, and radius R — equal to 12 mm.

The results of computer modelling of thermal, gas-dynamic and electric characteristics of turbulent plasma-arc flows under the conditions considered are shown in Figures 2–5. The basic calculation variant selected was the variant corresponding to arc current $I = 200$ A and plasma gas flow rate $G_1 = 1$ m^3 / h in blowing about the exposed flow region with cold gas. Results of all the calculations were compared with this variant, and effect of this or other working parameter of the plasmatron on spatial distributions of thermal and gas-dynamic characteristics of the plasma

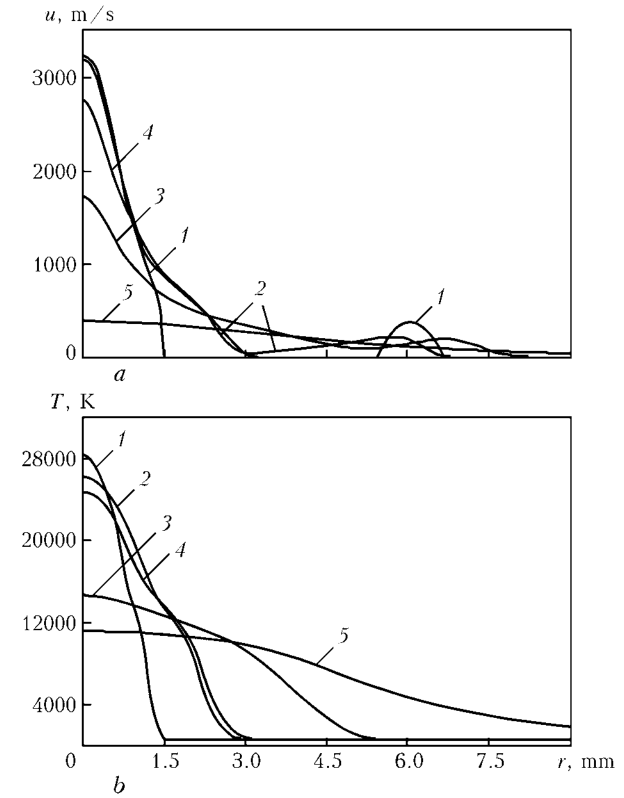

Figure 2. Radial distributions of velocity (*a*) and temperature (*b*) of the plasma at I = 200 A, G_1 = 1 m^3 / h, G_2 = 20 m^3 / h (*1–3*), G_2 = 0 (*4, 5*): *1* — region of the plasmatron exit section (z = = 3 mm); *2, 4* — region of the anode wire (z = 9.3 mm); *3, 5* — same at z = 50 mm

jet, as well on characteristics of the arc discharge was evaluated.

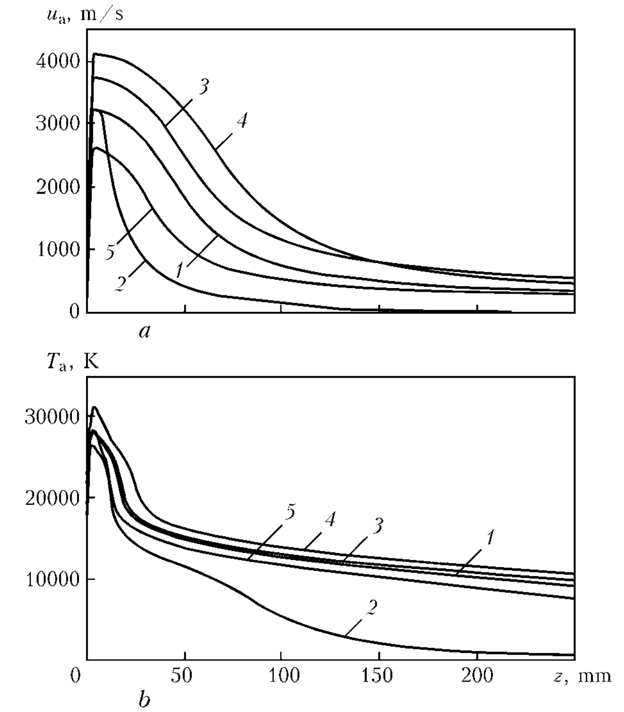

Figure 3. Longitudinal variations in axial values of velocity (*a*) and temperature (*b*) of the plasma under different conditions of operation of the plasmatron: *1* — I = 200 A, G_1 = 1 m^3 / h, G_2 = = 20 m^3 / h; *2* — I = 200 A, G_1 = 1 m^3 / h, G_2 = 0; *3* — I = 200 A, G_1 = 1.5 m^3 / h, G_2 = 20 m^3 / h; *4* — I = 260 A, G_1 = 1 m^3 / h, G_2 = 20 m^3 / h; *5* — I = 160 A, G_1 = 1 m^3 / h, G_2 = 20 m^3 / h

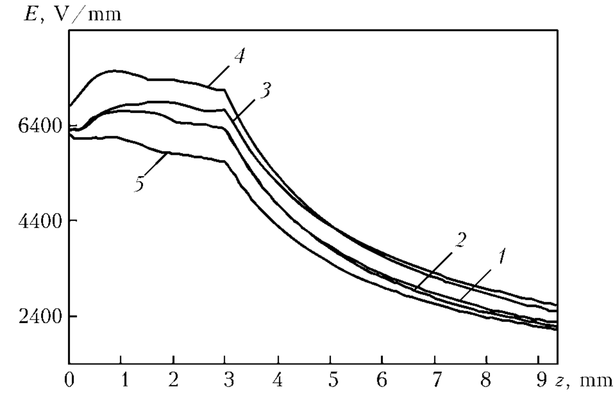

Figure 4. Longitudinal variations in intensity of the electric field under different conditions of operation of the plasmatron: *1–5* — same as in Figure 3

Consider now the effect of the backing gas flow on spatial characteristics of the plasma jet. The calculation results for the backing gas flow and corresponding submerged jet are shown in Figure 2. As seen, blowing about the plasma jet with the annular flow of the cold gas has a substantial effect on its thermal and gas-dynamic characteristics. Parameters of the arc flow in the initial region of the external flow remain almost identical in both cases. Further on, the flow of the gas blowing about the plasma jet prevents its broadening, and at a distance of about 50 mm from the plasmatron exit section the width of the plasma flow core not blown about with the shielding gas exceeds almost twice the width of the jet that is blown about (Figure 2, curves *5* and *3*).

Figure 3 shows the corresponding dynamics of variations in the velocity and temperature of the plasma along the axis of the system. Here curves *1* and *2* correspond to the submerged and blown about jet at I = 200 A and G_1 = 1 m^3 / h. As seen, a substantial decrease in the velocity and temperature of the unshielded jet begins from a distance of 35–40 mm from the exit section of the plasmatron nozzle. And starting from a distance of 150 mm from the exit section of the nozzle the single jet breaks down almost completely because of its unlimited broadening, while even at a distance of 250 mm from the exit section the shielded jet has a velocity of about 400 m / s and temperature of about 5500 K. Therefore, the plasma

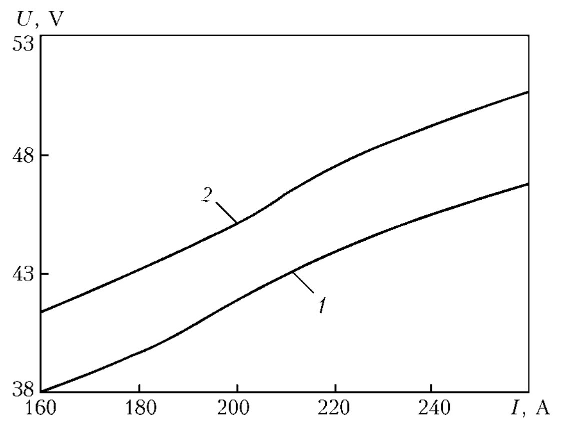

Figure 5. Volt-ampere characteristic of the arc column at different plasma gas flow rates G_1 = 1.0 (*1*) and 1.5 (*2*) m^3 / h

jet blown about with the cocurrent flow of the cold gas preserves an impulse and energy for a much longer time, and hardly mixes with the backing gas.

Figure 3 also shows axial profiles of the velocity and temperature of the shielded plasma jet at different values of the arc current and plasma gas flow rate. It can be seen from comparison of the calculation curves that at high values of the arc current the velocity and temperature of the plasma are higher, which is associated with a higher level of energy released in the arc plasma and more intensive effect of the electromagnetic forces accelerating the plasma.

As the plasma gas flow rate is increased, the velocity of the plasma increases almost proportionally to G_1, and for a flow rate of 1.5 m^3 / h it exceeds the gas flow rate for the basic calculation variant by 500 m / s on the average over the entire flow distance investigated (Figure 3, curve *3*). The temperature of the plasma in a case of a higher plasma gas flow rate grows insignificantly, i.e. from 3 to 15 % (depending upon the distance passed by the jet), and practically copies the corresponding dependence at $G_1 = 1$ m^3 / h.

In general, analysis of the modelling results shown in Figure 3 makes it possible to distinguish three flow regions described above: flow of the arc plasma inside the plasmatron nozzle, external region of flow of the arc plasma, and region of inertia motion of the nocurrent plasma. The initial region corresponding to the flow of the plasma inside the nozzle is characterised by substantial axial gradients of thermal and dynamic parameters of the plasma. The axial velocity dramatically grows, and temperature at the axis substantially decreases in this region. After the arc moves beyond the limits of the nozzle, axial gradients of the above values are gradually smoothed out. The role of viscous friction forces grows, some broadening of the arc and its slight interaction with the backing gas flow take place. However, electromagnetic forces in the external arc region continue to substantially contribute to formation of the flow. Inertia motion of the plasma occurs in the third region, and axial gradients of gas-dynamic and thermal characteristics of the plasma flow decrease almost exponentially.

Electric characteristics of the arc in the plasmatron under consideration are shown in Figures 4 and 5. They include distribution of the intensity of the electric field along the axis of the discharge and volt-ampere characteristic of the arc column. Increase in the intensity of the electric field within the nozzle channel (see Figure 4) results from the fact that at the selected values of the channel radius, arc current and plasma gas flow rate the intensity of the field near the cathode is lower than in the asymptotic region of the channel. This is also favoured by a gradual decrease in temperature of the plasma associated with energy losses for radiation and removal of heat to the channel walls, which leads to decrease in electrical conductivity and, accordingly, to increase in the intensity of the electric field required for maintaining the set discharge current. Upon leaving the channel, the plasma flow broadens to some extent, which leads to an insignificant decrease in the intensity of the field.

The calculated volt-ampere characteristic of the arc column within the ranges of currents under consideration (see Figure 5) is growing, the rate of growth of voltage with increase in the current substantially depending upon the plasma gas flow rate.

CONCLUSIONS

1. The mathematical model is suggested for description of gas-dynamic, thermal and electric processes occurring in arc plasmatrons. The model can be used for qualitative and quantitative evaluation of main characteristics of a turbulent flow of the arc plasma in direct- and indirect-action plasmatrons, including at the presence of cocurrent backing gas flow. Detailed numerical modelling was conducted for describing characteristics of the arc plasma flow under conditions of plasma spraying of a current-conducting wire.

2. Blowing about the plasma jet with a cocurrent flow of cold gas prevents its broadening and leads to a substantial increase in its length. For example, at a distance of about 50 mm from the exit section of the plasmatron nozzle the width of the plasma flow core not blown about with a shielding gas exceeds approximately twice the width of the shielded jet. As a result, the shielded plasma jet preserves an impulse and energy for a much longer time, and hardly mixes with the backing gas.

1. Petrov, S.V., Karp, I.N. (1993) *Plasma air-gas spraying*. Kiev: Naukova Dumka.
2. *Model TSR300H HVAF-ARC spray system*. http: / / www.uniquecoat.com / index-ARC.html
3. Engelsht, V.S., Asanov, D.S., Gurovich, V.Ts. et al. (1983) *Mathematical modelling of the electric arc*. Frunze: Ilim.
4. Borisov, Yu.S., Krivtsun, I.V., Muzhichenko, A.F. et al. (2000) Computer modelling of the plasma spraying process. *The Paton Welding J*., **12**, 40–50.
5. Favalli, R.C., Szente, R.N. (1998) Physical and mathematical modeling of non transferred plasma torches. *Brazilian J. of Physics*, **1**, 25--34.
6. (1990) *Theory of electric arc column*. Ed. by M.F. Zhukov. Novosibirsk: Nauka.
7. Lojtsyansky, L.G. (1973) *Fluid and gas mechanics*. Moscow: Nauka.
8. Borisov, Yu.S., Chernyshov, A.V., Krivtsun, I.V. et al. (1994) Computer-aided simulation and experimental study of dusted plasma jets emitting into limited space. In: *Proc. of National Thermal Spray Conf*. (Boston, 1994), 361--366.
9. Boulos, M.I., Fauchais, P., Pfender, E. (1994) *Thermal plasmas: Fundamentals and applications*. Vol. 1. New York, London: Plenum Press.
10. Launder, B.E., Spalding, D.B. (1990) The numerical computation of turbulent flows. *Computer Methods in Applied Mechanics and Engineering*, **8**, 269–289.
11. Ievlev, V.M. (1975) *Turbulent motion of high-temperature continua*. Moscow: Nauka.
12. Wilcox, D.C. (1994) *Turbulence modeling for CFD*. La, Canada, California: DCW Industries Inc.
13. Kolesnichenko, A.F. (1980) *Technological magnetohydrodynamic units and processes*. Kiev: Naukova Dumka.
14. Zhukov, M.F., Kozlov, N.P., Pustogarov, A.V. et al. (1982) *Near-electrode processes in arc discharges*. Novosibirsk: Nauka.
15. Samarsky, A.A. (1971) *Introduction into theory of difference schemes*. Moscow: Nauka.
16. Anderson, D., Tannehill, J., Pletcher, R. (1990) *Computational hydromechanics and heat exchange*. Vol. 1. Moscow: Mir.
17. Paskonov, V.M., Polezhaev, V.I., Chudov, L.A. (1984) *Numerical modelling of heat and mass transfer*. Moscow: Nauka.

KINETICS OF GROWTH OF NON-THROUGH-THICKNESS FATIGUE CRACKS IN 03Kh20N16AG6 AND 12Kh18N10T STEELS AT DIFFERENT VALUES OF THE COEFFICIENT OF STRESS CYCLE ASYMMETRY

V.V. KNYSH, S.A. SOLOVEJ and **A.Z. KUZMENKO**
E.O. Paton Electric Welding Institute, NASU, Kiev, Ukraine

Based on experimental data kinetic diagrams of fatigue fracture of steels 03Kh20N16AG6 and 12Kh18N10T at different values of the coefficient of stress cycle asymmetry are plotted. A three-parameter kinetic equation describing the regularities of development of non-through-thickness fatigue cracks in the studied steels is proposed, and its crack resistance parameters are determined. The fatigue life values calculated on the basis of the derived equation are compared with the experimental data.

Keywords: high-alloyed steels, cyclic crack resistance, fatigue life, stress intensity factor, coefficient of stress cycle asymmetry, semi-elliptical crack

Fatigue cracks in welded joints, as a rule, initiate in the zones of weld transition to the base metal in the points of action of maximum residual tensile stresses. These cracks, while developing on the metal surface and in-depth of the metal, form in their plane to have the shape close to a semi-elliptical one [1, 2]. It is known that interaction of residual stresses and alternating load cycle stresses in the welded joint concentrator zones leads to formation of a new stress cycle of the same range, as the initial one, but of another asymmetry, which is what determines the fatigue crack kinetics [3]. In this connection the regularities of development of fatigue cracks in welded joints can be readily described by kinetic equations, which contain the coefficient of stress cycle asymmetry in the explicit form.

At present there is a significant number of works devoted to investigation of the influence of stress cycle asymmetry on the rate of through thickness crack propagation in different structural materials [4–6]. As regards establishing such dependences for description of the kinetics of non-through-thickness fatigue cracks, a special independent experimental substantiation is required in view of the limited amount of published data. The experimentally established kinetic diagrams of fatigue fracture (KDFF) of base metal, produced at fixed values of the coefficient of stress cycle asymmetry, should still be the basic dependences expressing the degree of crack resistance.

To establish KDFF during fatigue testing for cyclic crack resistance of specimens with non-through-thickness fatigue cracks, it is necessary to determine the dimensions of these cracks along the entire front of their propagation. With this purpose, the E.O. Paton Electric Welding Institute developed a special procedure for determination of parameters of non-through-thickness cracks by indicator traces on their surface, which was successfully used to study the cyclic crack resistance of tee welded joints on 12Kh18N10T steel (Figure 1). This procedure includes the elements of fractographic and dye penetrant control techniques. A combination of both these methods allows tracing the movement of the crack front after complete fracture of the welded specimen.

In a specimen with a non-through-thickness crack the formed open cavity after preset time intervals (number of loading cycles) was filled with indicator liquid consisting of xylene (60 %), black electrographic toner (30 %) and acetone (10 %). As the time of contact of indicator liquid with the surface was 2–5 min, no drying up of indicator liquid was observed. Furtheron the excess liquid was removed from the crack inner surfaces by blowing compressed air through it for 1–2 min. However, a small amount of indicator liquid over the crack propagation front was contained as a result of the action of surface tension forces. Then a brush was used to itnroduce kerosene into the crack cavity, where the remains of the indicator liquid over the front of crack propagation coagulated with kerosene.

Owing to cyclic closing of the crack lips at crack closing and high viscosity of the coagulated indicator

Figure 1. Appearance of fatigue fracture of a T-joint specimen with indicator traces of growth kinetics of semi-elliptical crack surface

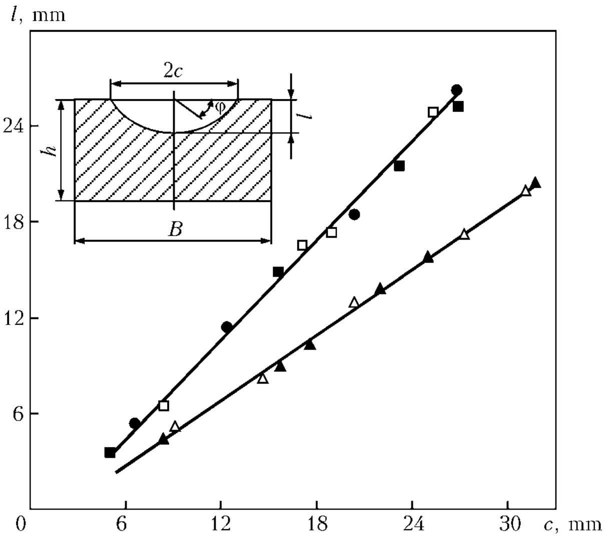

Figure 2. Dependence of depth l of semi-elliptical crack on its half-length c derived by marker lines: a — 03Kh20N16AG6 specimens at $R_\sigma = -1$ (▲), 0 (■), 0.5 (●); b — 12Kh18N10T specimens at $R_\sigma = -1$ (Δ), 0 (□); h, B — steel specimen height and width, respectively

liquid particles, its solid components penetrated into the fracture roughness over the entire front of crack propagation. Remains of kerosene were removed by compressed air, blowing it through the crack cavities for 1–2 min. The dried up coagulated particles of indicator liquid at subsequent introduction of indicator liquid and kerosene remained insoluble, forming a characteristic (indicator) trace in the form of a burrow.

Number of specimen loading cycles pertaining to completion of this stage, was fixed. The length of the crack on the specimen surface was measured with an error of ±0.1 mm in an optical microscope. After the preset time interval (number of loading cycles) was over, the above operations were repeated successively with indicator traces being recorded on the crack surface. The distances between the adjacent indicator traces were determined by the welded joint fracture, and the regularities of fatigue crack front development depending on the number of loading cycles were established.

The proposed procedure allows conducting experimental studies of the material cyclic crack resistance without disturbing the fatigue testing modes, and can be applied for different structural materials. This procedure is used in this study to experimentally establish KDFF of corrosion-resistant steels in the maximum deep point of the surface crack front.

Experimental studies of the regularities of propagation of surface semi-elliptical fatigue cracks in 03Kh20N16AG6 steel (σ_y = 335 MPa, σ_t = 685 MPa) and 12Kh18N10T steel (σ_y = 259 MPa, σ_t = 685 MPa) at different values of the coefficient of stress cycle asymmetry were conducted on 600 × 120 × 35 mm specimens. Specimen surface (in their middle part) was ground and a groove-shaped concentrator of maximum depth of 2.5 mm and width of 9 mm was milled out. Initial crack on the specimens surfaces was grown to the length of $2c$ = 12 mm at the set value of the coefficient of stress cycle asymmetry with an amplitude not higher than that of the working stress at which investigations of the growth of a non-through-thickness crack were later on performed. Specimens from steel 03Kh20N16AG6 were tested by uniaxial alternating tension-compression with the coefficient of stress cycle asymmetry $R_\sigma = -1$ (σ_{max} = 147 MPa), 0 (σ_{max} = 196 MPa) and 0.5 (σ_{max} = 249 MPa), and specimens from steel 12Kh18N10T — at $R_\sigma = -1$ (σ_{max} = 122 MPa) and 0 (σ_{max} = 192 MPa). Selection of cyclic loads of the preset asymmetry was performed so that the range of variation of the fatigue crack growth rate corresponded to KDFF linear section, and non-through-thickness cracks were developing similar to the surface semi-elliptical cracks of a stable shape [2].

Results of measurement of the c half-length of a crack on specimen surface and its maximum depth established by marker lines, at different values of the coefficient of stress cycle asymmetry, are shown in Figure 2. From the Figure it is seen that variation of the stress cycle asymmetry in non-through-thickness cracks leads to a change of the value of the coefficient of compression (ratio of crack depth l to its half-length c), but as the crack length increases it remains unchanged. In 03Kh20N16AG6 steel the compression coefficient is equal to approximately 0.9 at positive values of the coefficient of the stress cycle asymmetry (R_σ = 0 and 0.5), but decreases to 0.6 in the region of alternating stress amplitudes ($R_\sigma = -1$). The same occurs also in 12Kh18N10T steel — l / c = 0.9 and 0.6, respectively, at R_σ = 0 and –1.

Such a change of the compression coefficient can be accounted for as follows. The influence of the stress cycle asymmetry on evolution of the non-through-thickness crack contour consists in that the compressive part of the loading cycle promotes a more intensive relative opening of the tip of the crack which is in the plane-stress state (in particular, along axis c) than in the plane-strain state (in particular, along axis l), the relative crack growth rate and compression coefficient changing, respectively [2].

For plotting KDFF at propagation of semi-elliptical fatigue cracks, it is necessary to calculate the values of the stress intensity factor (SIF) corresponding to the specified loading conditions. Approaches to determination of such SIF under different conditions of load application and specimen geometry are known from publications [7–11]. The range of SIF for prismatic specimens under the conditions of uniaxial alternating tension-compression in the maximum deep point ($\varphi = \pi / 2$) of the front of development of a semi-elliptical fatigue crack was calculated by formula [7]

$$\Delta K = \frac{\Delta\sigma\sqrt{\pi l}}{\Phi}\,[M_1 + M_2(l/h)^2 + M_3(l/h)^4]\,g f_\varphi f_B, \quad (1)$$

where

$$M_1 = 1.13 - 0.09(l/c);\quad M_2 = -0.54 + 0.89(0.2 + l/c)^{-1};$$

$$M_3 = 0.5 - (0.65 + l/c)^{-1} + 14(1 - l/c)^{24};$$

$$g = 1 + [0.1 + 0.35(l/h)^2]\,(1 - \sin\varphi)^2;$$

$$f_\varphi = [(l/c)^2 \cos^2\varphi + \sin^2\varphi]^{1/4};$$

$$f_B = [\sec((\pi c)/B\sqrt{l/h})]^{1/2};$$

$\Delta\sigma$ is the range of nominal stresses in the gross section of a cyclically loaded specimen, which coincides with the crack plane; Φ is the elliptical integral of the second kind, which is calculated usually with the use of its approximate expressions, for instance in the following form:

$$\Phi = \left[1 + 1.464\left(\frac{l}{c}\right)^{1.65}\right]^{1/2}.$$

Equation (1) allows for the form of the crack on the rear, front and side surfaces of a specimen on SIF value.

Current values of the rate of crack propagation at the i-th step of their calculation $v_{li} = (\Delta l_i)/(\Delta N_i) = (l_i - l_{i-1})/(N_i - N_{i-1})$. were matched to the values of SIF range derived from (1) at $l = l_i - \Delta l_i/2$.

Dependences of the rate of fatigue crack growth in specimens of 03Kh20N16AG6 and 12Kh18N10T steels on SIF range in the maximum deep point of the crack front ($\varphi = \pi/2$) at different values of the stress cycle asymmetry coefficient are given in the form of the respective KDFF in Figure 3. The caption gives the equations of regression lines of experimental points corresponding to the above R_σ values.

It follows from KDFF that with increase of fixed R_σ values the angle of inclination of the regression lines of experimental points rises. It is proposed to describe such a nature of variation of KDFF by an equation with three constants:

$$\frac{dl}{dN} = C_{-1}(\Delta K)^{m_{-1} + \lambda\sqrt[3]{1 + R_\sigma}}, \tag{2}$$

where C_{-1} and m_{-1} are the material crack resistance characteristics at $R_\sigma = -1$; λ is the constant value characterizing the material sensitivity to stress cycle asymmetry.

The exponent $\varphi(R_\sigma) = \lambda\sqrt[3]{1 + R_\sigma}$ can be determined through crack resistance parameters C_{R_σ} and m_{R_σ} in Paris exponential dependence $dl/dN = C_{R_\sigma}(\Delta K) m_{R_\sigma}$ established from experimental KDFF, corresponding to the preset value of coefficient R_σ. So, for values $R_\sigma = 0$ and 0.5 the respective exponents $\varphi(0)$ and $\varphi(0.5)$ are found from the following relationship

$$\varphi(0) = \frac{\lg\,[C_0(\Delta K)]^{m_0} - \lg\,[C_{-1}(\Delta K)]^{m_{-1}}}{\lg \Delta K},$$
$$\varphi(0.5) = \frac{\lg\,[C_{0.5}(\Delta K)]^{m_{0.5}} - \lg\,[C_{-1}(\Delta K)]^{m_{-1}}}{\lg \Delta K}, \tag{3}$$

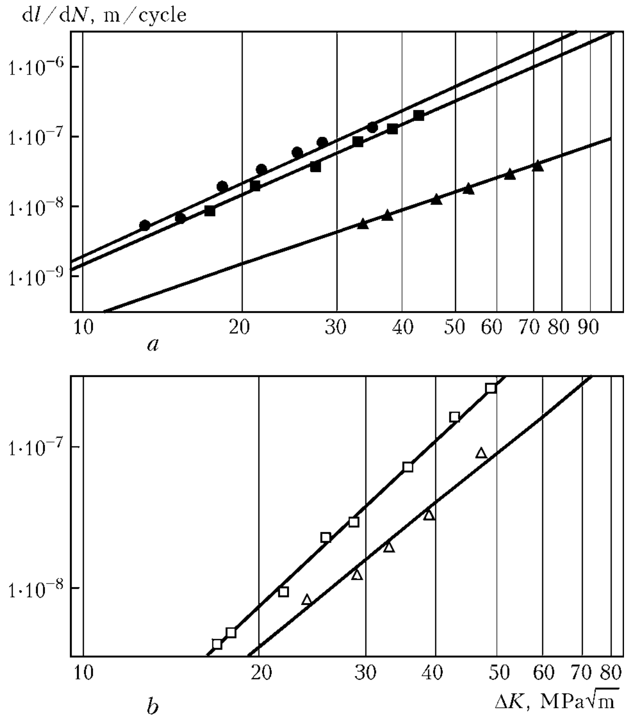

Figure 3. Kinetic diagrams of fatigue fracture and regression lines of experimental points of 03Kh20N16AG6 (*a*) and 12Kh18N10T (*b*) steels in the maximum deep point of semi-elliptical crack front: *a* — ▲ — $R_\sigma = -1$ (σ_{max} = 147 MPa), lg (dl / dN) = 2.414002·lg (ΔK) + (–11.6969); ■ — $R_\sigma = 0$ (σ_{max} = 196 MPa), lg (dl / dN) = 3.159111·lg (ΔK) + (–11.73748); ● — $R_\sigma = 0.5$ (σ_{max} = 249 MPa), lg (dl / dN) = 3.341055·lg (ΔK) + (–11.80641); *b* — Δ — $R_\sigma = -1$ (σ_{max} = 122 MPa), lg (dl / dN) = 3.421973·lg (ΔK) + (–12.83322); □ — $R_\sigma = 0$ (σ_{max} = 192 MPa), lg (dl / dN) = 3.997881·lg (ΔK) + (–13.29316)

the values of which vary in narrow ranges with increase of the front of development of a semi-eliptical fatigue crack (Figure 4) ($\varphi_{av}(0) = 0.72$, $\varphi_{av}(0.5) = 0.84$ for 03Kh20N16AG6 steel and $\varphi_{av}(0) = 0.27$ for 12Kh18N10T steel). With the known values $\varphi_{av}(R_{\sigma i})$ constant λ is found by the least squares method from the following equation:

$$\lambda = \frac{\sum_{i=1}^{n} \varphi_{av}(R_{\sigma i})\sqrt[3]{1 + R_{\sigma i}}}{\sum_{i=1}^{n} (\sqrt[3]{1 + R_{\sigma i}})^2}. \tag{4}$$

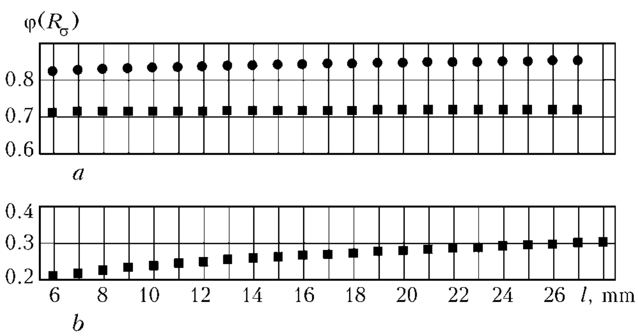

Figure 4. Dependence of exponential factor $\varphi(R_\sigma) = \lambda\sqrt[3]{1 + R_\sigma}$ of equation (2) on maximum depth of the surface crack in 03Kh20N16AG6 (*a*) and 12Kh18N10T (*b*) steels at $R_\sigma = 0$ (■) and 0.5 (●)

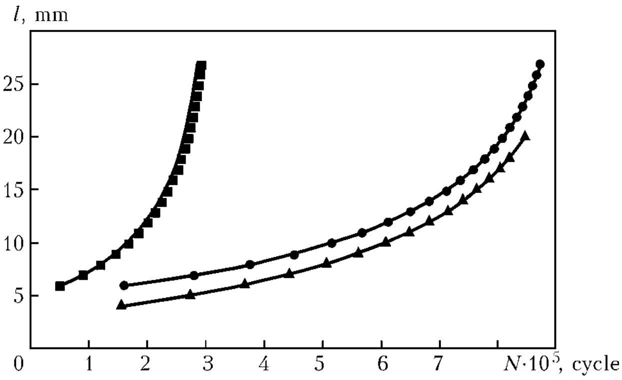

Figure 5. Dependence of maximum depth of surface crack on the number of stress alternation cycles in 03Kh20N16AG6 steel: ▲, ■, ● — experimental data for R_σ = –1, 0 and +0.5, respectively; curves — calculated data

Proceeding from the experimental data the following values of constants of ratio (2) were established for the studied steels: $C_{-1} = 0.2.10^{-11}$, $m_{-1} = 2.41$, $\lambda =$ $= 0.73$ (03Kh20N16AG6); $C_{-1} = 0.15\cdot10^{-12}$, $m_{-1} =$ $= 3.42$, $\lambda = 0.27$ (12Kh18N10T).

Fatigue life values calculated by integration of equation (2) showed that for the established crack resistance characteristics, the maximum deviation of calculated fatigue life values from the experimental ones is not more than 10 % for 03Kh20N16AG6 and 12Kh18N10T steels at different values of the coefficient of stress cycle asymmetry (Figures 5 and 6). Thus, kinetic equation (2) containing three material constants, can be applied in engineering practice to describe the kinetics of fatigue fracture of the studied steels at development of non-through-thickness cracks in the range of variation of the coefficient of stress cycle asymmetry of $-1.0 \le R_\sigma \le 0.5$.

CONCLUSIONS

1. Coefficient of compression of non-through-thickness cracks does not depend on the strength properties of corrosion-resistant steels 03Kh20N16AG6 and 12Kh18N10T steels, but is determined by the value of the coefficient of stress cycle asymmetry R_σ.

2. Diagrams of fatigue fracture of 03Kh20N16AG6 and 12Kh18N10T steels have been established experimentally for a maximum deep point of the front of a semi-elliptical crack at different R_σ values.

3. A three-parameter kinetic equation has been substantiated which describes the regularities of development of semi-elliptical fatigue cracks in 03Kh20N16AG6 and 12Kh18N10T steels, and explicitly allows for the value of the coefficient of stress cycle asymmetry R_σ. Values of the parameters (crack resistance characteristics) of the proposed equation have been established for the studied steels.

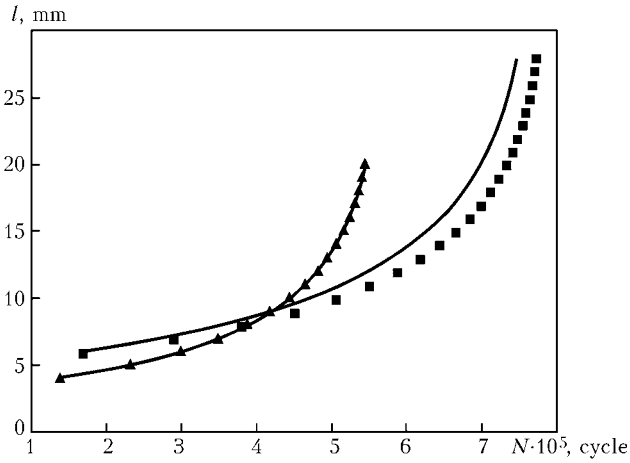

Figure 6. Dependence of maximum depth of surface crack on the number of stress alternation cycles in 12Kh18N10T steel: ▲, ■ — experimental data derived for R_σ = –1 and 0, respectively; curves — calculated data

1. Panasyuk, V.V., Sushinsky, A.I., Katsov, K.B. (1991) *Fracture of structure components with non-through-thickness cracks*. Kiev: Naukova Dumka.
2. Krasovsky, A.Ya., Orynyak, I.V. (2000) Assessment of residual life of welds in the first loop piping of nuclear power stations damaged by intercrystalline corrosion. *The Paton Welding J.*, **9/10**, 54–62.
3. Trufyakov, V.I. (1990) *Strength of welded joints at alternative loads*. Kiev: Naukova Dumka.
4. Trufyakov, V.I., Knysh, V.V., Mikheev, P.P. et al. (1987) Relationship between the rate of fatigue crack propagation and cycle asymmetry. *Problemy Prochnosti*, **3**, 5–7.
5. Troshchenko, V.T., Pokrovsky, V.V., Podkolzin, V.Yu. et al. (1991) Influence of loading cycle asymmetry and strength characteristics on cyclic crack resistance of structural alloys taking into account the phenomenon of fatigue crack closing. *Ibid.*, **10**, 17–25.
6. Pinyak, I.S. (2001) Analytical description of fatigue crack growth rate in metals at various asymmetries of loading cycle. *Ibid.*, **5**, 111–119.
7. (1990) *Reference book on stress intensity factors*. Ed. by Yu. Murakami. Vol. 2.
8. Letunov, V.I., Kramarenko, I.V., Shulginov, B.S. et al. (1985) Features of surface crack propagation in low-alloy steel at asymmetric cyclic bending. Report 1. *Problemy Prochnosti*, **11**, 17–20.
9. Ovchinnikov, A.V. (1986) Approximate formula for determination of stress intensity factors in bodies with surface cracks. *Ibid.*, **2**, 44–47.
10. Kopsov, I.E. (1990) Calculation of stress intensity factors for semi-elliptical surface crack in inhomogeneous stress field. *Ibid.*, **7**, 38–41.
11. Makhnenko, V.I., Makhnenko, O.V. (2000) Development of calculation procedures for assessment of admissibility of detected defects in welded joints of critical structures. *The Paton Welding J.*, **9/10**, 79–87.

EFFECT OF DISTRIBUTION OF MANGANESE IN STRUCTURAL COMPONENTS ON PROPERTIES OF LOW-ALLOY WELD METAL

V.F. GRABIN and **V.V. GOLOVKO**
E.O. Paton Electric Welding Institute, NASU, Kiev, Ukraine

The effect of oxygen potential and alloying ability of welding fluxes on distribution of manganese in the weld metal between non-metallic inclusions MnO and solid solution $Mn_{s.s}$ has been studied. The (MnO) / [$Mn_{s.s}$] ratio can be used for differential evaluation of the efficiency of alloying of the welds with manganese, allowing for a different character of its effect on strengthening of solid solution, composition of non-metallic inclusions, and structure and mechanical properties of the weld metal.

Keywords: submerged-arc welding, low-alloy steel, alloying of weld metal, macrostructure, distribution of manganese, mechanical properties

Steels remain the most common type of structural materials used for the fabrication of welded structures and apparatuses. This situation will persist for another 20–30 years. High- and increased-strength low-alloy steels have received the widest acceptance in the last years. Many investigations conducted in the field of metallurgy and development of new technologies for production of this class of steels made it possible to substantially improve their strength, toughness and ductility properties. This combination of properties was achieved owing to decrease in the carbon content of metal and refining it from oxygen, sulphur and phosphorus.

Decrease in the carbon content of low-alloy steels is accompanied by some deterioration of their strength properties, which is compensated for, as a rule, by an increased content of other alloying elements. Manganese is most often employed for these purposes. There are a large number of publications on the effect of this element on structure and strength of low-alloy steels [1–3]. Results of recent investigations [4] show that an increased manganese content of the weld metal with the ferritic-pearlitic structure may lead to increase in the content of the pearlitic component, and in some cases may promote its embrittlement. As reported in study [5], depending upon the distribution of alloying elements in metal, they may have a different effect on the structure formation conditions and properties. It can be seen from the results of these investigations that for adequate evaluation of the effect of manganese on structure and properties of the weld metal it is necessary to differentiate its content in solid solution and non-metallic inclusions. The data obtained can help to define the optimal range of the content of this alloying element in metal of the welds on low-alloy steels.

Investigations were conducted on samples of the weld metals produced in submerged-arc welding by using fluxes differing in basicity index (BI) and MnO content (Table 1), and wires Sv-08A and Sv-08GA. Welding of the butt joints was performed under the conditions and by the procedure specified in standard ISO 14171 (production of deposited metal) [6].

Specimens for chemical analysis and metallography were made from the deposited metal. Chemical composition was determined by the spectral analysis method using the «Baird» unit equipped with the IBM PC for processing analysis results. From three to five measurements were made for each specimen, and then the results were averaged. The content of individual components of microstructure, content of alloying elements in solid solution and element composition of non-metallic inclusions were determined by metal-

Table 1. Chemical composition (wt.%) and basicity of welding fluxes used in investigations

Designation of flux	BI	Na_2O	CaO	MgO	CaF_2	MnO	Al_2O_3	Fe_2O_3	SiO_2	Other elements
À	0.60	2.7	3.1	2.7	5.8	30.2	3.8	0.9	46.8	4.0
B	0.74	3.1	5.6	3.8	6.4	30.9	2.1	0.7	45.3	2.1
C	0.83	2.0	4.1	9.8	19.5	--	33.7	0.1	25.8	5.0
D	2.09	--	17.0	–	40.0	10.0	15.9	0.2	15.5	4.0
E	2.22	2.3	4.5	29.4	19.0	--	33.2	--	8.0	4.0
F	2.12	2.0	4.1	20.0	19.1	11.0	30.6	--	8.6	5.0

Table 2. Chemical composition (wt.%) of weld metal

Specimen No.	Designation of flux	Welding wire	C	Si	Mn	S	P
1	D	Sv-08À	0.041	0.156	0.30	0.015	0.015
2	E		0.062	0.132	0.37	0.015	0.015
3	D	Sv-8GA	0.051	0.226	0.63	0.013	0.004
4	À	Sv-08À	0.034	0.209	0.77	0.025	0.007
5	E	Sv-8GA	0.057	0.130	0.85	0.007	0.006
6	À		0.032	0.279	0.99	0.027	0.006
7	B	Sv-08À	0.040	0.251	1.00	0.028	0.028
8	F	Sv-8GA	0.045	0.250	1.13	0.013	0.007
9	B		0.036	0.421	1.41	0.022	0.027
10	C	Sv-08À	0.045	0.486	1.45	0.018	0.021
11	C	Sv-8GA	0.041	0.630	1.84	0.018	0.026

lographic examinations. Microstructure was investigated by the methods of optical and electron metallography using light microscope «Neophot-32» and the Jeol scanning electron microscope JSM-840 equipped with the MicroCapture board for capturing of images and subsequent display of images on the computer screen. The content of microstructure components was determined according to the IIW procedure [7], and the content of alloying elements in solid solution and that of non-metallic inclusions were determined by the X-ray microanalysis using the Link System energy-dispersive spectrometer Link 860 / 500 and wave-dispersive spectrometer Ortec.

Table 2 gives chemical composition of metal of the welds investigated, and Tables 3 and 4 give composition of structural components of the weld metal and its mechanical properties, respectively. As can be seen from the data presented, the manganese content of metal of the welds investigated varied approximately 6 times (from 0.30 to 1.84 wt.%), whereas the contents of carbon and silicon in metal of welds 1–8 varied within the narrow ranges (0.032–0.062 and 0.130–0.279 wt.%, respectively). Metal of welds 9–11 had an increased weight content of silicon (0.421–0.630 wt.%). To reveal the character of the effect of manganese on structure formation conditions and mechanical properties of the weld metal, the latter was alloyed with silicon. The sulphur and phosphorus content of metal of all the welds varied from 0.007 to 0.027 and from 0.004 to 0.027 wt.%, respectively.

Microstructure of metal of the investigated welds is shown in Figure 1. Fracture resistance of the weld metal was evaluated on the basis of true rupture resistance indicator S_k calculated according to GOST 1497 by the following formula:

$$S_k = P_k / F_k,$$

where P_k is the load at the moment of rupture of a specimen, and F_k is the area of a minimal cross section of the specimen after rupture.

It can be seen from Figure 2 that, whereas the certain relationship exists between the level of alloying of the weld metal with manganese and its strength properties, it is impossible to find such a relationship

Table 3. Content (vol.%) of structural components in weld metal

Specimen No.	PF	P	AF	OSPF	UOSPF	B	MAC phase	V_{NMI}
1	77.0	23.0	0	0	0	0	0	0.44
2	84.0	11.3	0	0	0	0	4.7	0.40
3	51.0	5.0	0	22	25	0	1.3	0.37
4	90.0	10.0	0	0	0	0	0	2.20
5	21.0	11.0	5	21	30	0	1.2	0.45
6	90.0	10.0	0	0	0	0	0	2.50
7	80.9	19.1	0	0	0	0	0	0.59
8	25.0	9.0	7	41	20	13	2.5	0.39
9	50.0	6.0	11	14	11	0	1.5	1.26
10	87.0	12.9	0	0	0	0	0	0.74
11	23.0	8.0	60	15	10	0	2.5	0.44

Notes. PF — polygonal ferrite; P — pearlite; AF — acicular ferrite; OSPF — ordered second phase ferrite; UOSPF — unordered second phase ferrite; B — bainite; V_{NMI} — content of non-metallic inclusions.

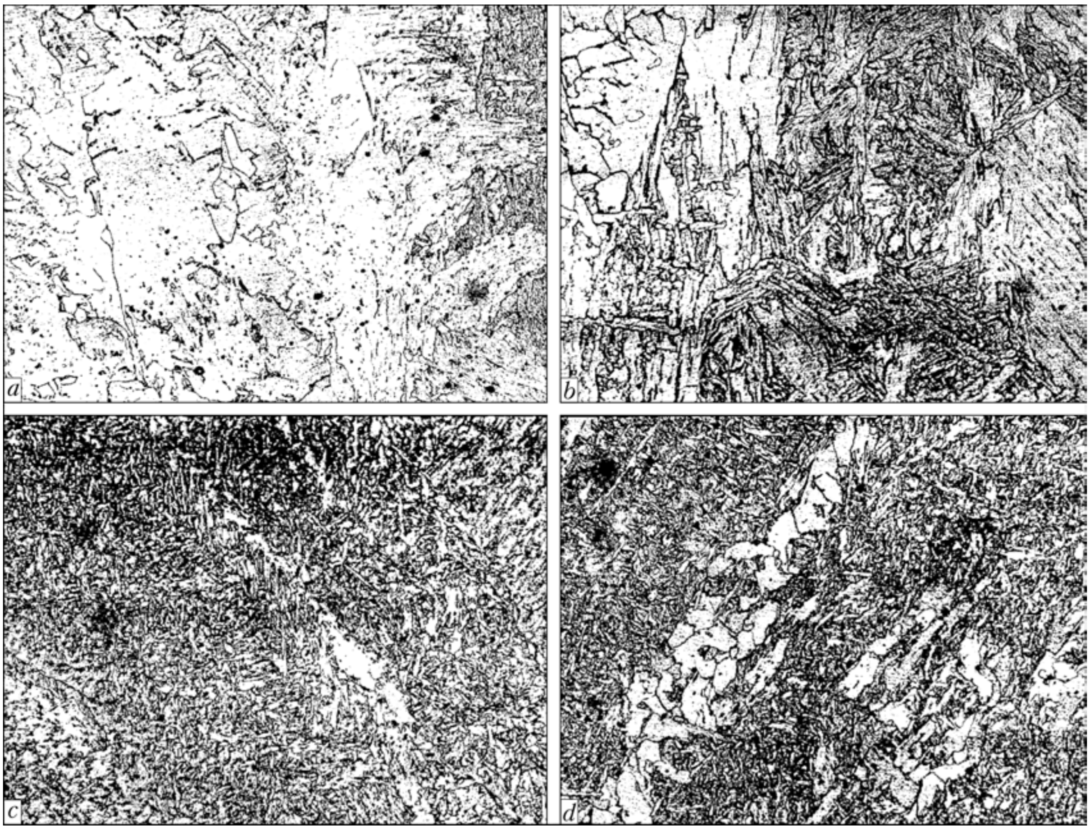

Figure 1. Microstructure of the weld metal in specimens 2 (*a*), 4 (*b*), 8 (*c*) and 9 (*d*) according to Table 2 (×400)

for rupture resistance indicator of the weld metal specimens.

Alloying the weld metal on carbon and low-alloy steels may have a marked effect on the content of PF in them [1–3]. Results of investigations of structure of the weld metal shown in Figure 3 are indicative of the absence of such a relationship in the specimens studied. In our opinion, this is attributable to the fact that manganese has an ambiguous effect on the weld metal. As reported in study [5], depending upon the interaction conditions, manganese that transfers to the weld pool metal from slag may concentrate in non-metallic inclusions, or enter into solid solution. Based on these assumptions, it is expedient to evaluate the effect of manganese on structure and properties of the weld metal by using an indicator that allows for the content of manganese both in non-metallic inclusions MnO and in solid solution $[Mn_{s.s}]$. For example, the $(MnO) / [Mn_{s.s}]$ ratio can be used as such an indicator. To derive such relationships, we determined chemical composition of non-metallic inclusions and content of manganese in solid solution using the investigation procedure described above. Results of the investigations are given in Table 5.

Based on the generated data, we calculated dependencies shown in Figure 4. As can be seen from the Figure, variation of the $(MnO) / [Mn_{s.s}]$ ratio from 60 to 90 leads to a substantial decrease in values

Table 4. Mechanical properties of weld metal

Specimen No.	$\sigma_{0.2}$, MPa	σ_t, MPa	δ, %	ψ, %	S_k, MPa
1	329.1	407.5	30.4	63.9	1128.8
2	325.6	402.4	28.0	58.7	974.3
3	367.1	466.3	34.2	74.1	1800.4
4	314.6	433.6	26.3	63.8	1197.8
5	348.5	490.6	36.0	74.9	1954.6
6	351.2	454.5	25.3	65.7	1325.1
7	344.4	432.9	28.5	59.7	1074.2
8	356.8	473.2	32.0	74.8	1877.8
9	385.4	508.0	29.2	64.9	1447.3
10	418.1	523.8	25.0	58.7	1268.3
11	437.4	589.0	22.9	62.9	1587.6

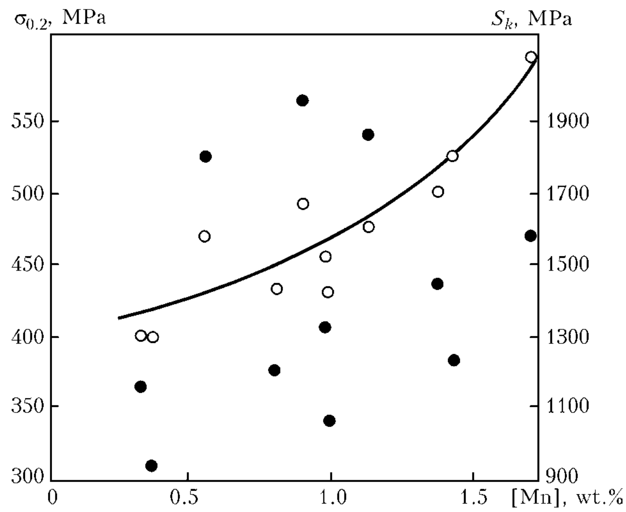

Figure 2. Effect of alloying of the weld metal with manganese on temporary $\sigma_{0.2}$ (○) and true S_k (●) rupture resistance

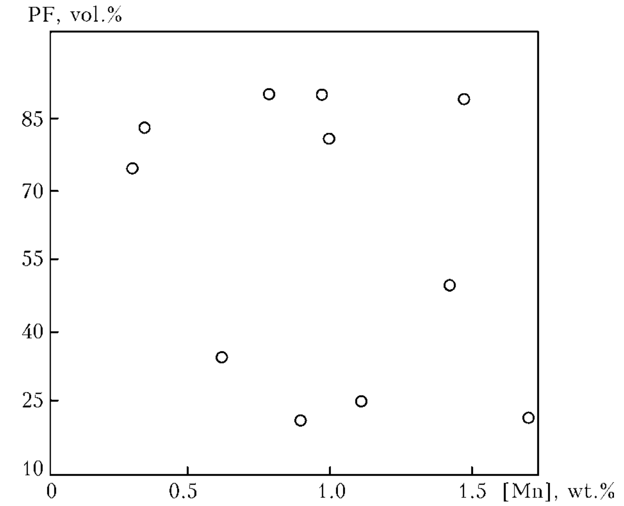

Figure 3. Effect of alloying of the weld metal with manganese on the PF content of its structure

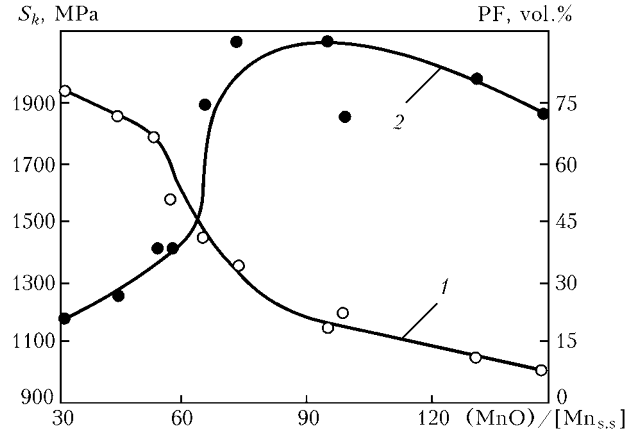

Figure 4. Effect of the (MnO) / [$Mn_{s.s}$] ratio on true rupture resistance S_k (*1*) and content of PF (*2*) in structure of the weld metal

of the true rupture resistance of the weld metal, which is associated with a dramatic increase in the volume content of PF. The use of the (MnO) / [$Mn_{s.s}$] ratio to describe the effect of alloying of the weld metal with manganese on its structure and mechanical properties makes it possible to study this process in more detail. So, it can be concluded from Figure 4 that alloying of the solid solution with manganese at a low (MnO) / [$Mn_{s.s}$] ratio (30–60) promotes strengthening of the weld metal, thus resulting in improvement of its strength properties. At a high (MnO) / [$Mn_{s.s}$] ratio (90--150), manganese in the weld metal is contained mostly in non-metallic inclusions. In such cases, structure of the weld metal is characterised by a high content of PF, while the solid solution is insufficiently alloyed with manganese, thus leading to decrease in the true rupture resistance.

Table 5. Content of non-metallic inclusions and manganese (wt.%) in solid solution

Specimen No.	Al_2O_3	SiO_2	MnO	[$Mn_{s.s}$]
1	16.09	34.78	48.82	0.30
2	35.27	23.64	38.82	0.25
3	19.42	29.10	42.61	0.82
4	0.32	45.64	51.47	0.52
5	60.63	4.73	31.53	1.03
6	1.05	41.39	61.18	0.85
7	1.26	33.33	64.07	0.47
8	13.99	22.39	58.25	1.30
9	1.32	29.82	68.15	1.02
10	9.37	30.66	65.15	1.30
11	6.23	21.74	76.71	1.38

Therefore, the investigations conducted showed the possibility of using the (MnO) / [$Mn_{s.s}$] ratio for evaluation of the effect of the manganese content of the weld metal on its structure and mechanical properties.

Allowance for the effect of the (MnO) / [$Mn_{s.s}$] ratio on properties of the weld metal permits a differential evaluation of the efficiency of alloying of the welds with manganese on the basis of a different character of its effect on strengthening of the solid solution and content of non-metallic inclusions, as well as on structure and mechanical properties of the weld metal.

1. Grabin, V.F., Denisenko, A.V. (1978) *Metals science of welding of low- and medium-alloy steels*. Kiev: Naukova Dumka.
2. Livshits, L.S., Khakimov, A.N. (1989) *Metals science of welding and heat treatment of welded joints*. Moscow: Mashinostroenie.
3. Court, S.A., Pollard, G. (1989) The effects of Mn and Si on the microstructure and properties of SMA steel weld metal. *IIW Doc. II-A-789--89*.
4. Grabin, V.F., Golovko, V.V., Solomijchuk, T.G. et al. (2003) Analysis of structural state of weld metal produced by using welding wires of the ferritic-pearlitic grade. *The Paton Welding J.*, **8**, 17--22.
5. Golovko, V.V. (2006) *Interaction of metal with slag in submerged-arc welding of low-alloy steels using agglomerated fluxes*: Syn. of Thesis for Dr. of Techn. Sci. Degree. Kiev.
6. *ISO 14171*: Welding consumables — Wire electrodes and wire-flux combinations for submerged arc welding of non alloy and fine grain steels — Classification. Introd. 01.02.2007.
7. (1986) Guidelines for the classification of ferritic steel weld metal microstructural constituents using the light microscope. *Welding in the World*, 24(**7 / 8**), 144--148.

THERMAL ANALYSIS OF MICROLAMINATE FILLERS BASED ON INTERMETALLIC-FORMING ELEMENTS

A.E. SHISHKIN[1], **E.A. SHISHKIN**[1] and **A.I. USTINOV**[2]
[1]G.V. Kurdyumov Institute for Metal Physics, NASU, Kiev, Ukraine
[2]E.O. Paton Electric Welding Institute, NASU, Kiev, Ukraine

Microlaminate Ni / Al fillers were used as an example to determine by the method of differential thermal analysis the temperature ranges and intensity of running of reaction diffusion processes depending on their heating rate, and evaluation of the specific amount of heat evolving at running of the reaction of high-temperature self-propagating synthesis triggered by an electric spark discharge in these materials, was performed.

Keywords: diffusion welding, microlaminate foils of Ni/Al system, self-propagating high-temperature synthesis, heat, reaction diffusion, differential thermal analysis

Microlaminate foils, consisting of alternating interlayers of components capable of reaction diffusion with formation of intermetallics, are regarded as promising materials for producing permanent joints. The possibility of application of such laminated materials as fillers, is based on that the reaction of synthesis between the components as a result of their diffusion mixing at heating [1] is accompanied by heat evolution, which can greatly activate the diffusion mobility of atoms in the joint zone and thus provide the conditions for formation of the joint in the solid state [2–5].

According to theoretical calculations depending on the heating rate, the process of the intermetallic compound formation in a composite material consisting of components capable of the synthesis reaction, can develop along three paths: as a result of continuous heating (process of reaction diffusion (RD)), reaction of high-temperature self-propagating synthesis (HTSPS) and explosion [6].

The process of optimization of the structure of such a filler material and thermal cycle of its heating to ensure welded joint formation can be greatly simplified, if parameters characterizing the thermal processes running in it at different heating modes are known. In a number of works optical methods were used, which allow assessment of the velocity of HTSPS wave propagation [7]. Pyrometric methods were applied to determine the maximum temperature of foil heating in the front of HTSPS wave propagation [7, 8]. The amount of heat evolving at running of RD process was determined by calorimetry methods [9]. High-speed radiography was also used to study the dynamics of variation of phase composition of the sample during running of HTSPS reactions [8].

These methods, however, do not provide the full set of data required to assess the processes of heat evolution and temperature ranges of their running in microlaminate foil under the conditions close to heating parameters characteristic for the thermal cycle of welding. For calorimetric methods there exist limitations on the rate of sample heating, while the optical methods of determination of the rate of HTSPS wave propagation do not allow determination of quantitative characteristics of thermal effects.

For analysis of the processes running with heat evolution or absorption, the method of differential thermal analysis (DTA) is highly efficient [10]. Considering the high efficiency and relative simplicity of hardware realization, DTA method was used to study the reactions, running in microlaminate foils in the mode of HTSPS and RD process. This method was used to assess the heat evolving at HTSPS and determine the temperature ranges of running of RD process in the case of microlayered foils consisting of interlayers of nickel and aluminium produced by layer-by-layer deposition of component vapour phases in vacuum using the electron beam method [5].

Thermal analysis of RD process. At determination of the heat of phase transformations in materials, the DTA method is based on comparison of temperatures of the studied sample and standard at their continuous heating under identical conditions. VDTA-8 instrument was used in the work [10]. The block diagram of measurement of sample temperature and temperature difference of the sample and standard using thermocouples is shown in Figure 1. The high sensitivity of this method is achieved by thermocouples being connected «in opposition» and recording the differential signal (temperature difference of the sample and standard), one of the thermocouples being used

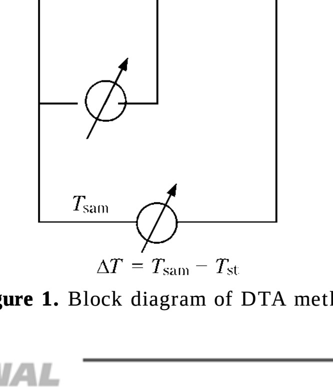

Figure 1. Block diagram of DTA method

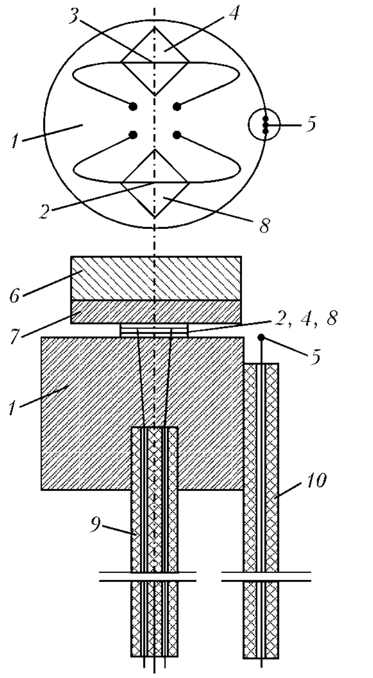

Figure 2. Schematic of DTA sensor: *1, 7* — block and cover from foamed quartz; *2, 3* — thermocouples of the sample and standard; *4* — sample; *5* — controlling thermocouple; *6* — clamp-down cover; *8* — standard; *9, 10* — ceramic insulators

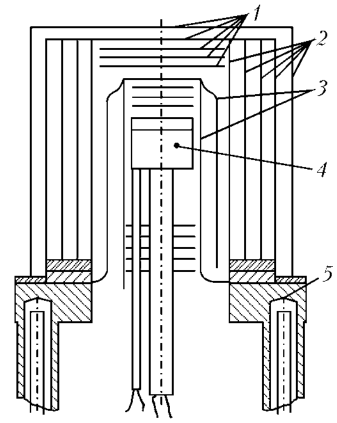

Figure 3. Schematic of low-voltage resistance furnace: *1, 2* — shields; *3* — heater; *4* — sensor block; *5* — current conduits

for measurement of the temperature of the sample, and the other — of that of the standard.

The design of low-temperature (maximum heating temperature of up to 1000 °C) highly sensitive DTA sensor is shown in Figure 2, and its location in the heating chamber — in Figure 3.

Measurments were performed with chromel-alumel thermocouples with electrode diameter of 0.2 mm. Thermocouple *2* was used to measure the sample temperature, and thermocouple *3*, connected by the differential schematic (see Figure 2) measured the temperature difference between the sample and standard. Copper foil was used as the standard. Thermocouple *5* was used to measure the furnace temperature, and control the furnace temperature at heating rates of up to 400 °C / min.

When studying the processes running with high rates and heat evolution, for instance, reaction of explosion, burning or decomposition, the so-called DTA method with a «dilutant» [11] is used for measurement of the evolving heat. In our case thin foils of the studied material were placed between the plates of heat-conducting material («dilutant»), which was 0.1 mm copper foil. Foamed quartz having low heat conductivity was applied for sample heat insulation [12], the same copper foil equal in weight and size to the foil into which the sample was placed, being used as the standard.

The sensor was placed into a low-voltage resistance furnace with a heater of «double tube» type from molybdenum tin (Figure 3). Low-inertia furnace which allowed heating to be performed at up to 400 °C / min rates, was placed into the water-cooled vacuum chamber. Investigations were conducted in helium of grade «A» at the pressure of 0.5 atm.

To control heating, recording and documenting the data, a system of automation of thermal methods of analysis based on IBM computer with special software was used.

Figure 4, *a* shows that heating leads to running of exothermal reactions in multilayer foil, occurring in three stages, judging by heat evolution peaks. It may be assumed that these processes are associated with certain stages of running of RD between the aluminium and nickel layers. As the foil composition in the phase equilibrium diagram corresponds to the two-phase region of NiAl and Ni_3Al, and at the initial stages of RD process Al_3Ni compound forms in Ni / Al microlaminate foils [9], it may be assumed that the observed RD stages and the corresponding thermal effects may be due to $Al + Ni \rightarrow Al_3Ni + Ni \rightarrow AlNi + AlNi_3$ sequence. The first stage of RD process starts at a relatively low temperature (about 240 °C), and

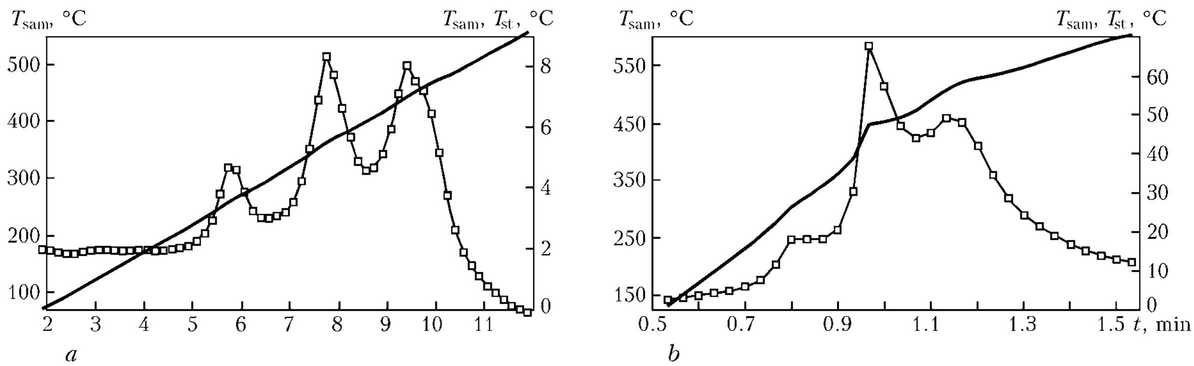

Figure 4. Thermograms of Ni–Al alloy (31.2 at.% Al) derived at continuous heating at the rate of 50 (*a*) and 400 (*b*) °C / min

is accompanied by minor heat evolution, and the subsequent stages — by more intensive heat evolution.

At increase of heating rate (Figure 4, *b*) of the sample the appearance of thermograms does not change qualitatively at the same three-stage nature of heat evolution. However, the height of the peak of temperature difference between the sample and standard rises significantly, and a certain change of the proportion of values of the second and third peaks is observed. This leads to the conclusion that increase of the rate of microlaminate foil heating greatly intensifies the rate of RD running at the second and third stages of the process. Just sample temperature, at which the processes of heat evolution begin, i.e. aluminium and nickel layers come into diffusion interaction remains unchanged.

The obtained data showed that at continuous heating of microlaminate fillers based on Ni / Al system in the heating rate range from 50 to 400 °C / min, the exothermal reactions between the elements forming the laminated structure start at the temperatures of about 240 °C, and are practically completed when the temperature of 500–550 °C has been reached. The heat evolution process has several stages, the intensity of running of which essentially depends on the sample heating rate — with its increase the intensity of heat evolution (peak height in DTA curves) rises significantly, while the temperature interval of the second and third stages of RD process shifts to the region of higher temperatures, whereas the temperature of the start of solid-phase reactions in the laminated structure (first stage of RD) remains practically unchanged. From the obtained data it is seen that use of Ni / Al system based microlaminate materials as fillers can be highly effective when producing permanent joints on the basis of materials, for which heating up to temperatures of 250–500 °C provides a high diffusion mobility of atoms. In this case, heat evolution due to RD in a microlaminate material, will promote activisation of diffusion mobility of atoms in the joint zone, i.e. joint formation in the solid state (without local melting of the materials being joined).

Evaluation of specific heat of HTSPS reaction. It is known that at increase of heating rate of laminated materials based on intermetallic-forming elements the HTSPS process can be initiated in them. When such laminated materials are used as fillers, such HTSPS characteristics as value of heat effect and combustion wave propagation rate, are important. In this work laminated foil of Ni / Al system was used to conduct evaluation of heat evolved due to HTSPS reaction. HTSPS reaction was initiated by local heating of a small part of the sample from room temperature to the temperature of the start of a high-rate reaction as a result of an electric spark discharge. In this case, the velocity of propagation of the combustion front was equal to about 0.5–1.0 m / s.

To determine the amount of heat of HTSPS reactions, the heating temperature of a pack consisting of several layers of multilayer foils placed between two

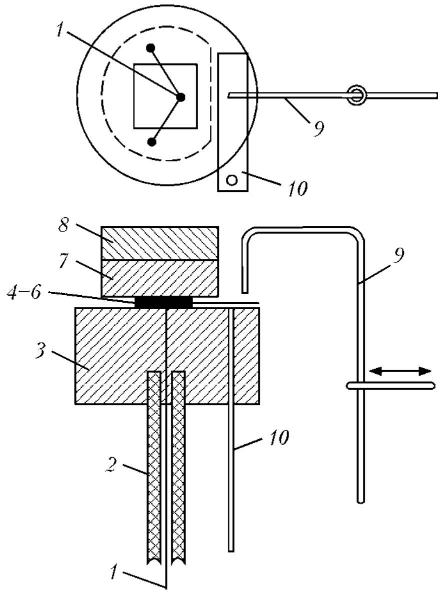

Figure 5. Schematic of measuring block with electric spark ignition: *1* — thermocouple; *2* — ceramic post; *3*, *7* — foamed quartz block; *4–6* — pack from copper foil with sample; *8* — cover-load; *9*, *10* — mobile and stationary electrodes for firing

copper foils 0.2 mm thick, was measured. The pack was placed into a foamed quartz block. One of the sample foils of a greater length was placed directly on a stationary electrode of the discharge device under the mobile electrode. The pack temperature was measured by a chromel-alumel thermocouple (electrode diameter of 0.1 mm) contacting the copper plates (Figure 5).

After pumping down the chamber with the measuring block (~ $1 \cdot 10^{-1}$), HTSPS was initialized in microlaminate foil by a capacitor discharge using a mobile contact and electromagnetic relay. Recording was performed by a quick-action potentiometer. It is seen in the thermogram (Figure 6) that after initiation of HTSPS process the pack temperature rises quickly

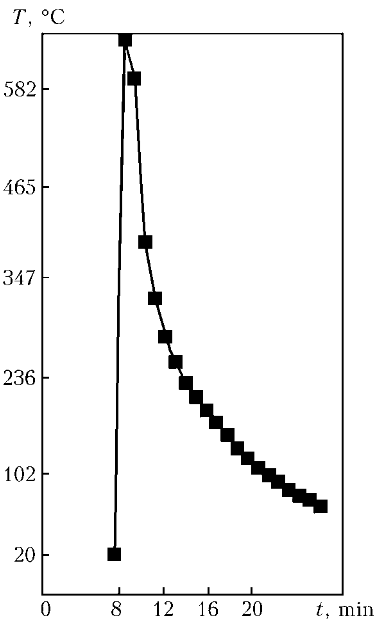

Figure 6. Thermogram of HTSPS reaction in Ni–Al sample (61.2 at.% Al)

(for about 1 s) up to a certain maximum value, dependent on the amount of evolving heat, weight of the sample and copper foil, which were selected so that heating of the entire pack did not exceed the copper melting temperature. As a rule, this temperature was in the range of 500–700 °C.

Assuming that as the reaction progressed the heat exchange between the microlaminate foil and «dilutant» occurred rather quickly, the equation for calculation of adiabatic temperature of the pack (microlaminate foil + «dilutant») can be written as follows:

$$\Delta H_{298}(Ni_aAl_b)m_{Ni/Al} + Q^T_{Ni_aAl_b} + Q^T_{Cu} = 0,$$

where $\Delta H_{298}(Ni_aAl_b)$ is the specific heat evolution due to formation of Ni_aAl_b compound (for single-phase state of HTSPS reaction product the specific heat evolution corresponds to specific enthalpy of this compound formation); $m_{Ni/Al}$ is the weight of microlaminate foil; $Q^T_{Ni_aAl_b} = m_{Ni_aAl_b}\int_{T_R}^{T} C_p(Ni_aAl_b)dT$ is the heat required for heating Ni_aAl_b compound from room temperature to temperature T; $C_p(Ni_aAl_b)$ is the heat capacity of Ni_aAl_b compound; $m_{Ni_aAl_b}$ is the weight of $Ni_aAl_b(m_{Ni/Al} = m_{Ni_aAl_b})$ compound formed as a result of HTSPS, $Q^T_{Cu} = m_{Cu}\int_{T_R}^{T} C_p(Cu)dT$ is the heat required for heating the copper foil («dilutant») from room temperature to temperature T; m_{Cu} is the copper foil weight; $C_p(Cu)$ is the heat capacity of copper.

Determining the temperature to which the pack was heated as a result of running of HTSPS reaction in microlaminate foil, and assigning the values of microlaminate and copper foil weights, the above equation was used to calculate the specific heat evolved at Ni_aAl_b formation.

For evaluation of applicability of the proposed procedure microlaminate foil was selected, in which the proportion of nickel and aluminium corresponds to Ni_2Al_3 single-phase region in the equilibrium diagram of Ni–Al system. At the weight of microlaminate and copper foils of 0.0265 and 0.0865 g, respectively, the pack was heated up to the temperature of 700 °C during HTSPS. Substituting these values into the above equation and performing the calculations, we obtain* specific heat evolution of microlaminate foil equal to $268.2\cdot10^6$ J / (kg·mol). By the data of [13] the value of specific enthalpy of the reaction of synthesis of Ni_2Al_3 compound is equal to $282.4\cdot10^6$ J / (kg·mol). Allowing for deviation of the studied foil from the stoichiometric composition and possibility of partial running of RD along the layer boundaries in the laminated material before the start of HTSPS process, it may be concluded that the obtained values of specific heat evolution in microlaminate foil agree well with the value of specific enthalpy of the compound synthesis reaction under the conditions when this interaction is practically ruled out.

On this basis, the data on specific heat evolution due to running of HTSPS reaction initiated by electric spark ignition in microlaminate foil and obtained by the above procedure can be used for evaluation of the characteristics of heat evolution in microlaminate foils.

In terms of practical application of such materials in the form of foils for activation of diffusion processes in welding in the mode of initiation of HTSPS reaction, experimental determination of specific heat evolution of laminated materials using the proposed method can provide an express evaluation of energy characteristic of the fillers.

CONCLUSIONS

1. DTA method with a «dilutant» was used to establish that at heating of microlaminate foils based on Ni / Al system RD runs with heat evolution in several stages differing by temperature ranges, in which non-monotonic variation of RD running rate is observed.

2. It is shown that the rate of heating of microlaminate foils in the range of 50–400 °C / s essentially influences the intensity of RD running at all the stages of the process. With increase of the heating rate the start of the reactions of transformation corresponding to the second and third stage, shifts towards the region of higher temperatures. The start of running of the first stage of RD process in microlaminate Ni / Al foils is practically independent on the foil heating rate. The process of heat evolution at continuous heating of microlaminate foils is completed at sample heating to 500–550 °C.

3. A method is proposed for determination of the specific amount of heat evolving in microlaminate foil, which is based on determination of the temperature of heating of microlaminate foil with a «dilutant» at initiation of HTSPS reaction in it using an electric discharge. The case of Ni / Al microlaminate foil is used as an example to show that specific enthalpy of formation of Ni_2Al_3 compound during HTSPS reaction in microlaminate foil produced by electron beam process is equal to about 95 % of the value theoretically calculated for this compound.

The work was performed with the financial support under the Program of the NAS of Ukraine «Nanosystems. Nanomaterials. Nanotechnologies» (Project #106).

1. Merzhanov, A.G. (1993) Theory and practice of SHS: worldwide state-of-the-art and the newest results. *Int. J. SHS*, 2(**2**), 113–158.
2. Matsuura, K., Ohsasa, K., Sueoka, N. et al. (1998) In-situ joining of nickel monoaluminide to iron by reactive sintering. *ISIJ Int.*, 38(**3**), 310–315.
3. Pascal, C., Martin-Ayrel, R.M., Tedenac, J.C. (2002) Joining of nickel monoalumide to a superalloy substrate by high

*At $Q^T_{Ni_aAl_b}$ calculation value of heat capacity of Ni_2Al_3 compound at temperature T was determined by an analytical dependence given in [13].

pressure self-propagating high-temperature synthesis. *J. Alloys and Compounds*, **337**, 221--225.
4. Yushchenko, K.A., Zadery, B.A., Zvyagintseva, A.V. et al. (2006) Application of nano-structured materials for diffusion bonding of heat-resistant nickel alloys. *The Paton Welding J.*, **11**, 2–8.
5. Ishchenko, A.Ya., Falchenko, Yu.V., Ustinov, A.I. et al. (2007) Diffusion welding of finely-dispersed AMg5–27 % Al_2O_3 composite with application of nanolayered Ni / Al foil. *Ibid.*, **7**, 2–5.
6. Chashchina, A.A., Knyazeva, A.G. (2005) Conditions of material joining using the solid-phase synthesis. *Khimiya v Interes. Ustojch. Razvitiya*, **13**, 343--350.
7. Rogachev, A.S., Grigoryan, A.E., Illarionova, I.G. et al. (2004) Gas-free burning of bimetal Ti / Al nanofilms. *Fizika Goreniya i Vzryva*, 40(**9**), 45–51.
8. Gras, C.H., Charlton, F., Gaffet, E. et al. (1999) In situ synchrotron characterization of mechanically activated self-propagating high-temperature synthesis applied in Mo–Si system. *Acta Mater.*, 47(**7**), 2113--2123.
9. Ma, E., Thompson, C.V., Clevenger, L.A. (1991) Nucleation and growth during reactions in multilayer Al / Ni films: The early stage of Al_3Ni formation. *J. Appl. Phys.*, 69(**4**), 2211--2218.
10. Kocherzhinsky, Yu.A. (1974) Pilot specimens of equipment for physical-chemical analysis at high temperatures. In: *Equipments for examination of physical properties of materials*. Kiev: Naukova Dumka.
11. Vilyunov, V.N. (1984) *Theory of ignition of condensed material*. Novosibirsk: Nauka.
12. Shmykov, A.A. (1961) *Handbook of heat-treater*. Moscow: Mashgiz.
13. Morsi, K. (2001) Review: reaction synthesis processing of Ni--Al intermetallic materials. *Mater. Sci. and Eng.*, **299**, 1--15.

THE E.O. PATON BRIDGE HALF A CENTURY LATER

V.A. KOVTUNENKO
E.O. Paton Electric Welding Institute, NASU, Kiev, Ukraine

Presented is the information on requirements to steel, joining technologies and welding equipment specified by designers for fabrication of an all-welded road bridge. The forthcoming reconstruction of the bridge is based on up-to-date achievements of metallurgy and welding engineering.

Keywords: arc welding, low-alloyed steels, motor-road bridge, all-welded structure, span structures, technology, equipment, mounting

The first all-welded motor-road bridge named after E.O. Paton was built more than fifty years ago. During this time the load on its structures increased seven times. Further operation of the bridge is possible on condition of its substantial reconstruction.

Construction of an all-welded structure was preceded by a large volume of engineering and research work, which was performed successfully under the leadership of Evgeny Oskarovich Paton, bridge-building expert.

It was necessary to substantiate and prove that a welded structure cannot be an imitation of a riveted one. Not only the principles of design, calculation, and engineering, but also material selection differed by other, fundamentally new approaches.

Initially the standard low-carbon unkilled steel applied for riveted bridges, was used for the bridge span structure. Control of metal used for fabrication of welded span structures was not given enough attention. The found cases of cracking in the weld metal and sometimes also in the base metal, necessitated development of special steel for welded bridges.

The main requirements made of steels applied for bridge span structures, were as follows:

• steel should be less prone to transition into the brittle state under the conditions of low temperatures and stress concentration, which is due to bridge operation at the temperature down to –40 °C, as well as impossibility of development of structures without rather abrupt change of the section and other stress raisers;

• span structures of bridges require steel not susceptible to ageing, i.e. change of the strength and ductility properties because of work hardening, the impact of the temperature cycle of welding and operation time;

• the steel should enable production of a welded joint, which would have a high resistance to cracking in the weld, HAZ and base metal. The welded joint should have sufficient strength and ductility.

Steel 16D (wt.%: 0.10–0.18 C; 0.12–0.25 Si; 0.4–0.7 Mn; 0.20–0.35 Cu) developed and used in the structures of the E.O. Paton bridge, mainly satisfied these requirements, and was included into GOST 6713 «Low-alloyed structural rolled stock for bridge-building».

In 1950s the main technological welding processes were coated-electrode manual arc welding and submerged-arc automatic (semiautomatic) welding. The period of preparation for bridge construction was characterized by intensification of design work to develop the equipment to perform welding in fabrication and mounting of metal structures, improvement of welding technology and welding consumables.

The main requirements to the quality of welding equipment included:

• stability of the set mode under the production conditions (mode correction during welding usually leads to deterioration of weld quality);

• possibility of precise guidance of the electrode along the weld (depends on the welding mode, weld type and other conditions);

• possibility of welding fillet and butt welds;

• reliability of the hardware in operation and simplicity in service;

• light weight and transportability of the automatic welding machine, no need for cumbersome devices for its displacement.

In 1950s these requirements were the best satisfied by TS-17-M tractor, DSh-5 and DSh-27 semi-automatic holders, which were widely applied for welding span structures in the plants and mounting sites. TS-17-M tractor for submerged-arc welding is quite widely accepted even now in mechanical engineering and construction, owing to its reliability and easy maintenance.

For the first time in the world practice, a new submerged-arc welding process was developed for making vertical butt welds in site, which was called welding with forced formation of the weld, thus allowing mechanization also of the vertical and inclined welds.

The approaches used in development of motor-road and railway bridge structures by welding elaborated in 1950s are still valid.

Low-carbon steels with low strength and technological properties are now replaced by a new generation of low-alloyed steels of a higher and high strength. New sparsely-alloyed steels of 355–490 MPa grades 06GBD, 06G2BD, and 09G2SYuCh have passed in-

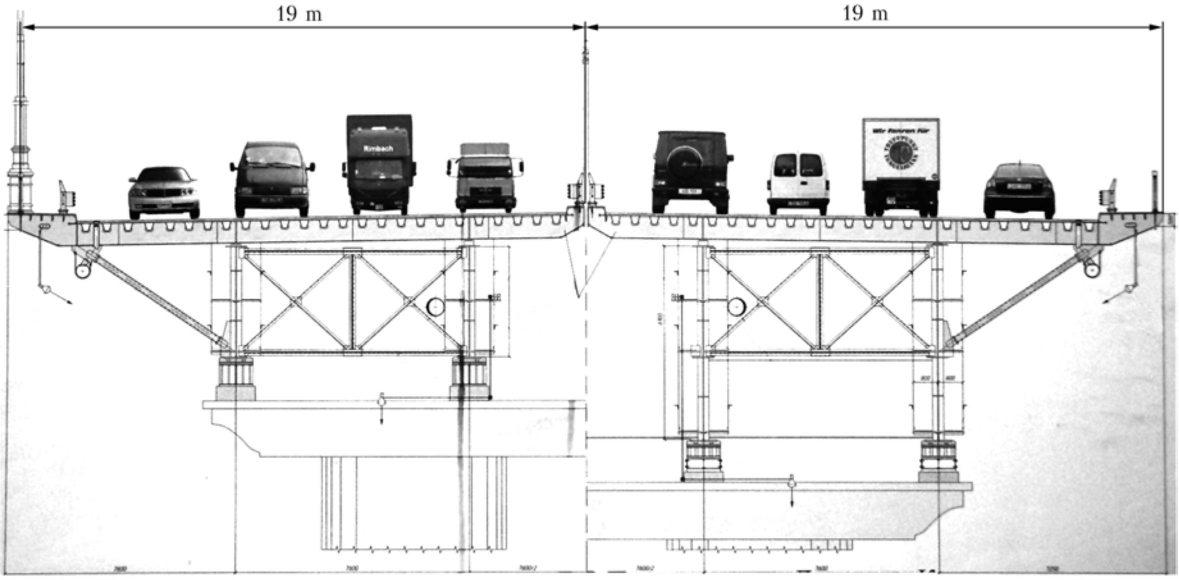

Schematic of the bridge after reconstruction

dustrial trials and are being introduced into bridge construction.

Welding in CO_2 or gas mixtures (CO_2 + Ar) with solid or flux-cored wire, contact-arc welding for joining flexible rests to steel-concrete span structures are used in fabrication of bridge metal structures and in site alongside automatic submerged-arc welding.

An attempt is made in site to apply electroslag welding (where it is rational). R-bars of concrete structures are connected by explosion welding. Welding and allied technologies became indispensable processes in fabrication of practically all types of metal structures.

Considerable progress in the field of bridge construction coincides with half a century jubilee of operation of the E.O. Paton bridge. Its reconstruction will begin in the near future with direct participation of specialists of the E.O. Paton Electric Welding Institute. In order to shorten the reconstruction period, it is proposed to supply maximum large blocks for mounting. The bridge will be divided into two halves. In one half the work on replacement of the roadway will be performed, and the other will be open to traffic, and then vice versa. Bridge width will be increased from 28 to 38 m, thus allowing four-lane traffic in each direction (Figure). The bridge will become wider, will be capable of standing the current loads and intensity of traffic, while preserving its grand architectural style.

TWO-OPERATOR MACHINE FOR TIG WELDING OF COPPER

N.A. GRANOVSKY[1], **V.V. TIMCHENKO**[2], **V.M. ILYUSHENKO**[3] and **G.A. BUTAKOV**[3]
[1]Priazovsky State Technical University, Mariupol, Ukraine
[2]SC «UkrNIIImetallurgmash», Slavyansk, Ukraine
[3]E.O. Paton Electric Welding Institute, NASU, Kiev, Ukraine

Two-operator machine for TIG welding of copper in helium was developed. The machine consists of the main module (power source) and two remote modules powered by 3×36 V voltage and having a self-sufficient system of antifreeze cooling. The machine ensures an independent adjustment of welding current of each of the two stations, welding current stabilization, reliable and fast arc excitation and stable arcing in helium in copper welding.

Keywords: TIG welding, copper, helium, current pulses, power transistor, choke, inductance, welding current adjustment, two-operator power source

In current engineering the products from copper and its alloys are used in manufacture of moulds of ESR units, continuous casting machines, etc. It is rational to make large-sized items by welding, thus allowing saving the expensive copper. Various methods are used for welding copper — automatic submerged-arc [1], electroslag [2], plasma [3] welding, as well as gas-shielded welding in the atmosphere of shielding gases such as argon, nitrogen or helium with nonconsumable tungsten electrode (TIG) [4].

It is rational to apply TIG welding for short welds, in welding complex-shaped items, as well as when joining thin parts (up to 12 mm). The simplicity of the welding process and possibility of visual control make this process preferable to other processes. On the other hand, TIG welding of massive copper items requires preheating, this lowering the efficiency of the welding process. Process efficiency can be increased by using shielding gas, namely nitrogen or helium. However, pores are often found in welds made by arc welding in nitrogen [5]. In this connection nonconsumable tungsten electrode helium-arc welding is used in fabrication of copper items. The industry does not make specialized equipment for nonconsumable (tungsten) electrode welding in helium. The enterprises usually use for these purposes the equipment designed for argon-arc welding (UPS 301, UDGU 501), or additionally fit DC power sources with torches for nonconsumable (tungsten) electrode welding. High currents required for welding copper more than 10 mm thick, necessitate application of water-cooled torches, which is not always possible in winter in unheated shops. Large dimensions of the parts being welded require designing equipment, allowing welding to be performed at a considerable distance from the point of its connection to 380 V mains. It is also necessary to ensure remote adjustment of the welding current directly from the work site. It should be noted that the control cable connecting the welding station with the power source, should have a smaller diameter compared to the power cable as far as possible, should be light-weight and flexible, which is important considering its great length. In view of the above, development of a machine for helium-arc welding meeting the above requirements, is an urgent task.

Figure 1. Main module of the machine

The above machine is designed for welding on flanges from 60 mm copper to ESR mould with 30 mm thick wall. In order to speed up the work on the mould fabrication, the machine was made to have a two-operator circuit, this allowing welding to be performed simultaneously in two different places, while saving the power used for preheating the mould case both due to shortening of welding time, and due to increase of heat input into the mould from two simultaneously running welding arcs.

The machine has the main (Figure 1) and two remote modules (Figure 2) which can be removed for a distance of up to 50 m each from the main module. The main module (Figure 3) includes a power welding transformer, rectifier module, two chokes, two current-limiting ballast resistances, and an auxiliary three-phase transformer 380 / 36 V for powering the control circuits and cooling systems of remote modules.

The unit realizes the principle of current adjustment through variation of inductance connected in series into the welding circuit. Both the remote modules are assembled by the same circuit (Figure 4).

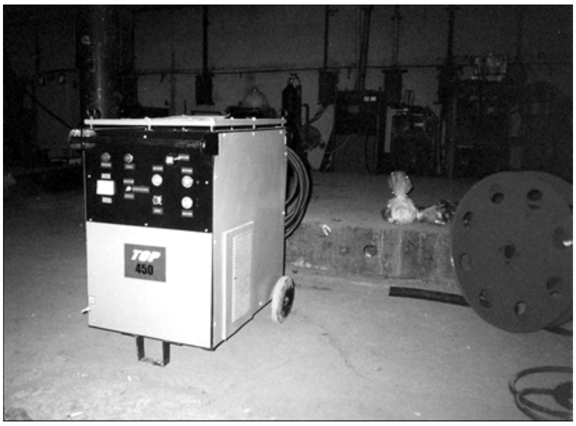

Figure 2. Remote module of the machine

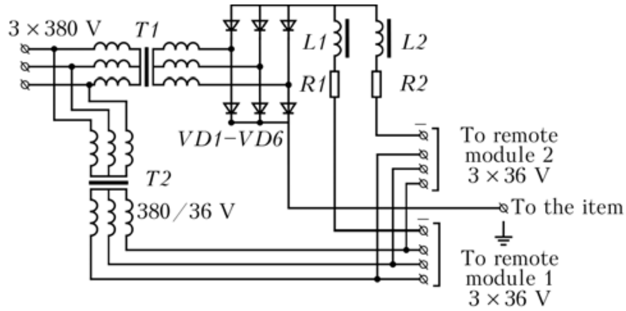

Figure 3. Simplified block diagram of the main module: *T1*, *T2* — power and auxiliary transformers, respectively; *VD1–VD6* — three-phase bridge rectifier module; *L1*, *L2* — chokes; *R1*, *R2* — current-limiting resistors

They have a self-sufficient system of anti-freeze cooling, which is circulated by a centrifugal pump driven by motor *M1*. The latter also drives the fan blowing air through the cooling radiator.

Power transistor *VT1* operating in the key mode, is connected in series into the welding circuit. Current adjustment is performed by variation of the repetition rate of pulses unblanking the transistor, with changing of the choke inductance.

Stabilization of current I_{st} means stabilization of an averaged integral value of the pulsed welding current.

The following relationship is valid for alternating sinusoidal current:

$$\tilde{O}_L = 2\pi f L, \quad (1)$$

where X_L is the choke inductive reactance; f is the current frequency; L is the choke inductance.

In the case of pulsed current in order to apply formula (1) it is necessary to decompose the measured signal into Fourier series and determine the inductive reactance components of each of the harmonics separately. It is obvious that at the change of the pulse repetition rate the choke inductive reactance will also change, I_{st} decreasing at increase of frequency, and vice versa.

A simple proportional adjustment law was used for welding current stabilization:

$$\Delta f = k(I_{st} - I^*), \quad (2)$$

where I^* is the set value of averaged welding current (resistance *R4* in Figure 4); k is the coefficient of regulator gain selected experimentally with regard to system stability.

Variation of the welding current pulse frequency using power transistors allows varying frequency f, this allowing the required value X_L to be obtained at smaller values of choke inductance L, i.e. an essential reduction of the choke weight, overall dimensions and cost. To improve the stability of arcing in helium [6], power transistor *VT1* is shunted by ballast resistance *R3* through which the direct component of arc current runs. During pauses in welding contactor *K* breaks up the pilot arc circuit, while control circuit *SU* does not send control pulses to transistor *VT1*, this leading to zeroing of torch *G* (see Figure 4). Water-cooled torches of Abicor Binzel, Germany, are used as the latter. They are designed for up to 450 A direct current required for welding copper [4, 5]. Control of *VT1* transistor is performed by control circuit *SU* and the welding current is set by potentiometer *R4*. Current feedback is provided through voltage read from a standard shunt (500 A, 75 mV).

At the moments of accidental short-circuiting of the tungsten electrode to the item the voltage between taps *6* and *7* of control circuit *SU* drops to several volts. The circuit is interlocked and stops issuing unblanking pulses to transistor *VT1*, thus preventing failure of the latter; ballast resistances *R1* and *R2* are used for limiting the short-circuit current, if it occurred at the moment of time when transistor *VT1* is open.

Block-diagram of the process control system (Figure 5) consists of two loops: loop of stabilization of the mean integral value of arc current and loop of voltage control to determine the accidental short-circuiting of tungsten electrode to the item. $I_w(t)$ feedback signal read from R_{sh} after the integrating block (formula (1)) is compared with set value I^*, and depending on mismatch value and sign ΔI pulse generator *PG* generates correction Δf, summed up with carrier frequency f. Change of pulse repetition rate leads to

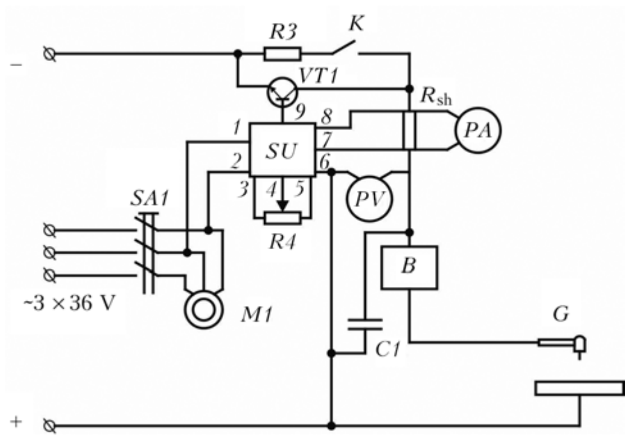

Figure 4. Simplified diagram of the remote module: *SA1* — automatic switch; *M1* — asynchronous motor 3 × 36 V of self-sufficient cooling system; *R3* — ballast resistance; *VT1* — power transistor; *R4* — potentiometer for setting welding current; *SU* — control circuit; R_{sh} — shunt; *C1* — protection capacitor; *B* — arc exciter; *PV* — voltmeter; *PA* — ammeter; *G* — torch

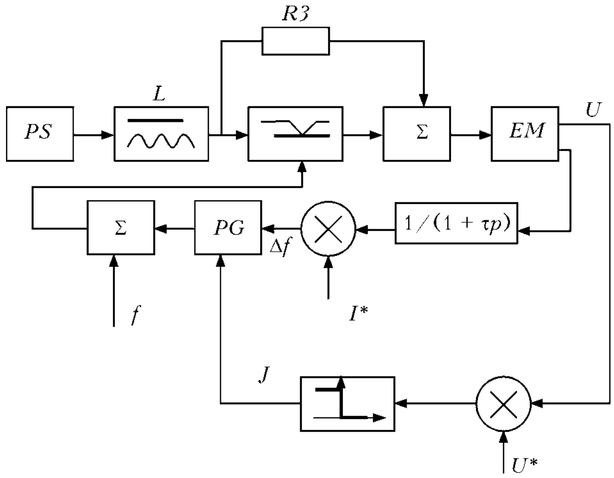

Figure 5. Block-diagram of process control system

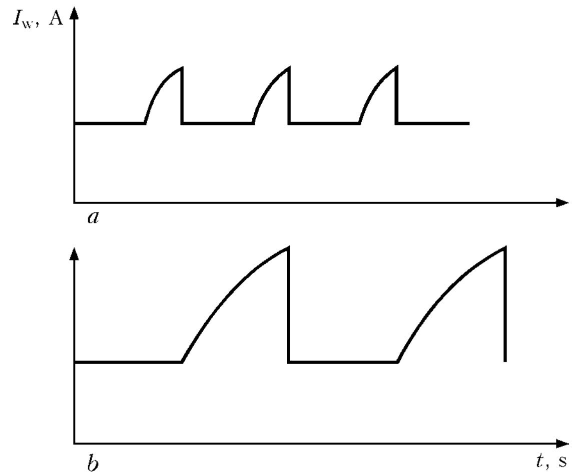

Figure 6. Welding current oscillograms: *a* — I_w = 240; *b* — 420 A

a change of choke inductive reactance, i.e. current stabilization in the welding circuit.

Loop of welding voltage monitoring is designed for protection of power transistor *VT1*. At short-circuiting of the electrode to the item, the welding current rises which may lead to an abrupt increase of pulse frequency. Function of switching off pulse generator *J* can be presented as follows:

$$\begin{aligned} &J = 1 \text{ at } U \le U^*, \quad (U - U^*) \le 0, \quad \Delta U \le 0, \\ &J = 0 \text{ at } U > U^*, \quad (U - U^*) > 0, \quad \Delta U > 0. \end{aligned} \qquad (3)$$

Figure 6 gives oscillograms of welding current in welding at medium and high currents.

It should be noted that at the moments of accidental short-circuiting transistor *VT1* is blanked, but current continues flowing in the welding circuit. This current is determined by ballast resistances *R1* and *R3* connected in series, so that the arc is excited at tungsten electrode separation from the item being welded.

Initial arc excitation is performed by arc exciter *B*. It is experimentally established that the firing pulse energy of 0.8 J is required for a reliable excitation of the arc, which is much higher than the requirements (0.2 J) for an arc in argon [7]. The latter is attributable to a higher potential of helium ionization [8], and higher values of near-electrode voltage drops in helium [6] due to higher energy characteristics of the welding arc in helium [4, 6].

The machine was tested in manufacture of ESR copper moulds at SC «UkrNIImetallurgmash» (Slavyansk, Donetsk region). It features reliability in operation and good welding-technological characteristics. It should be noted that with the selected machine circuit a standard three-wire cable of 3 × × 4 mm^2 cross-section is used as the control cable, this allowing easy transportation of the remote modules mounted on carriages, in the shop. Fitting the machine with torches with 8 m length of the hose assembly allowed welding upper welds on 2870 mm high mould without lifting the remote module.

CONCLUSIONS

1. For TIG welding of massive items it is rational to apply two-operator units with a common power source, this lowering their cost, improving the efficiency of the welded item fabrication and reducing the power consumption for preheating.

2. Stabilization of an averaged integral value of pulsed current in nonconsumable electrode welding of copper in helium is performed by variation of the frequency of welding current pulses, generated by the power transistor, this allowing variation of the inductive resistance of the choke connected in series into the welding circuit, without changing its inductance.

3. For an effective excitation of the arc in tungsten-electrode welding of copper in helium, the energy of the firing pulse should be not less than 0.8 J.

4. Mounting the transistor pulse generator in the remote module, and the current-limiting ballast resistance and choke in the power source allows reduction of the weight and overall dimensions of the remote module, this allowing elimination of remote control of the power source and improving the remote module mobility.

1. (1974) *Technology of fusion electric welding of metals and alloys*. Ed. by B.E. Paton. Moscow: Mashinostroenie.
2. Lychko, I.I., Ilyushenko, V.M., Alekseev, A.P. (1967) Electroslag welding of copper plate. *Avtomatich. Svarka*, **10**, 80--83.
3. Vennekens, R., Shevers, A.A. (1977) Plasma MIG welding of copper alloys. *Welding and Metal Fabr.*, 45(**4**), 227–235.
4. (1978) *Welding in machine-building*: Refer. Book. Vol. 2. Ed. by A.I. Akulov. Moscow: Mashinostroenie.
5. Gurevich, S.M. (1981) *Reference book on welding of non-ferrous metals*. Kiev: Naukova Dumka.
6. Lenivkin, V.A., Dyurgerov, N.G., Sagirov, Kh.N. (1989) *Technological properties of shielded-gas welding arc*. Moscow: Mashinostroenie.
7. Belinsky, S.M., Kagansky, B.A., Temkin, B.Ya. (1975) *Equipment for consumable-electrode inert-gas welding*. Leningrad: Energiya.
8. (1976) *Properties of elements*. Ed. by G.V. Samsonov. Moscow: Metallurgiya.

COMPARATIVE EVALUATION OF WEAR RESISTANCE OF ELECTRODE MATERIALS APPLIED FOR RECONDITIONING TRAM RAILS

Ya.P. CHERNAYK
E.O. Paton Electric Welding Institute, NASU, Kiev, Ukraine

Tribotechnical characteristics of metal deposited with flux-cored wires of austenitic (PP-AN202) and ferritic (PP-AN203) classes and M76 steel have been evaluated. It is established that at dry friction at metal sliding over metal the best set of service properties is found in the deposited metal of austenitic class, which is also capable of strengthening in service.

Keywords: arc surfacing, flux-cored wires, tribotechnical characteristics, wear-resistance, reconditioning tram rails

In service of tram wheels and rails, working as a pair, mainly the inner side surfaces of the head or rail jaws are worn. The wear process is the most intensive in the curvilinear sections of the track, where girder rails are usually mounted, the service life of which is between 5 and 8 years, depending on traffic intensity.

PWI developed the technology of reconditioning of rails directly on the track [1], which significantly reduces their operating cost. This became possible due to development of new flux-cored wires of austenitic (PP-AN202) and ferritic (PP-AN203) classes for surfacing difficult-to-weld high-carbon steels without preheating.

The requirements made of tram rails are highly contradictory. They should have sufficient strength, increasing with the increase of the cross-sectional area, and on the other hand, it is rational to try to reduce the rail weight from the viewpoint of cost. To improve the wheel adhesion with the rail, the rolling surface should be sufficiently rough, although it should be smooth to improve the resistance to motion. Rail rigidity is required for higher resistance to bending, while flexibility is needed to lower the impact-dynamic action on the wheels. The rail metal should be hard, so as to resist crumpling and friction, while being tough to avoid fracture [2].

Composition (wt.%) of rail steel M76 and metal deposited by experimental wires

Material (wire grade)	C	Si	Mn	Cr	Ni + Mo + V	Ti
M76 steel base metal	0.780	0.20	1.00	–	–	–
Deposited metal						
austenitic (PP-Np-OP1)	0.450	1.28	1.10	–	1.31	2.55
ferritic (PP-Np-OP2)	0.504	0.45	10.04	9.82	2.15	–

Having determined the wear resistance characteristics of the developed electrode materials, it is possible to evaluate their performance in the first approximation, without having to do long-time and expensive service trials. With this purpose the tribotechnical characteristics of the metal deposited with PP-AN202, PP-AN203 flux-cored wires and M76 steel applied for fabrication of tram rails and wheels, were studied.

Evaluation of wear resistance and friction properties of the deposited metal was performed using an all-purpose component of the friction machine, designed for laboratory-experimental evaluation of tribotechical characteristics of friction pairs at room temperature [3]. Testing was conducted by the method of pit wear by shaft–plane schematic without any additional feeding of lubrication into the friction zone. Test samples cut out of the upper beads of deposited metal, had the size of 3×20 mm. The mating body of 40 mm diameter and 12 mm width is made of steel M76 of hardness *HB* 180. At sample testing its wear by the volume of the worn pit, mating body wear by the difference in its weight before and after testing, as well as the force of friction between the sample and mating body were determined.

By the results of preliminary experiments the following testing mode was selected: sliding rate of 0.06 m/s, load of 29.5 N, duration of testing after running-in — 35 min. Such a mode ensured stabili-

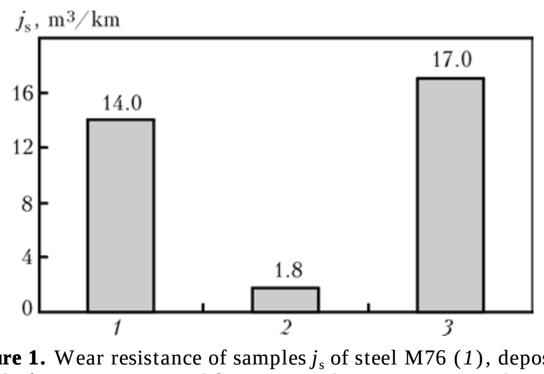

Figure 1. Wear resistance of samples j_s of steel M76 (*1*), deposited metal of austenitic (*2*) and ferritic (*3*) classes in a pair with mating body of M76 steel

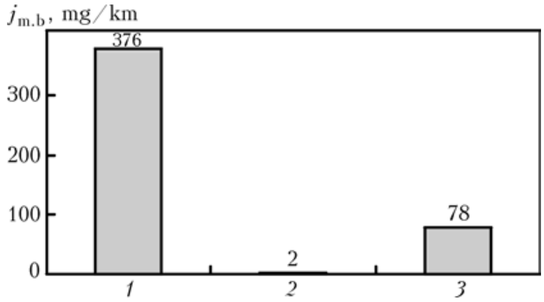

Figure 2. Wear resistance of mating body $j_{m.b}$: *1* — M76 + M76; *2* — M76 + austenitic metal; *3* — M76 + ferritic metal

zation of tribotechical characteristics of all the studied metals. Application of the system of sample positioning allowed repeating testing of each sample not less than three times in the new section of the sample friction surface and new friction path of the mating body.

Samples were cut out of the metal deposited with model flux-cored wires PP-Np-OP1, PP-Np-OP2 of 2.6 mm diameter (Table) in the modes, ensuring good bead formation directly at rail cladding (current of 400–450 A, voltage of 24–26 V, deposition rate is not less than 30 m / h). Experimental wires ensured metal composition similar to that produced at one-layer surfacing of rails from M76 steel with PP-AN202 (PP-Np-OP1) and PP-AN-203 (PP-Np-OP2) wires. Samples of steel M76 were cut out of tram rail head.

Analysis of the derived results shown in Figures 1–3, leads to the conclusion that metal of the austenitic class deposited with flux-cored wire PP-Np-OP1 has the highest wear resistance values. Wear of mating body after its testing is minimum.

Wear resistance of metal of the ferritic class deposited with PP-Np-OP2 wire, is close to that of rail steel M76. However, wear of mating body in a pair with the deposited metal sample is 4–5 times lower than that of a mating body in a pair with a sample of M76 steel. It may be assumed that when PP-AN203 wire is used for surfacing, wear resistance of all the reconditioned parts of steel M76 operating at friction of metal over metal, will be on the level of that of the new parts, while wear of the mating part will be significantly reduced.

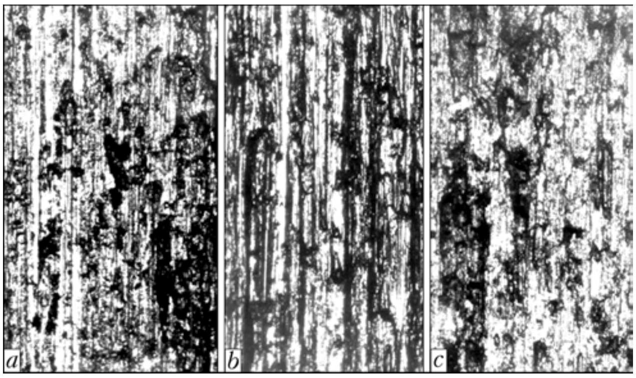

Figure 4. Appearance of friction surface of samples of steel M76 (*a*), deposited metal of ferritic (*b*) and austenitic (*c*) classes (×80)

Investigation results are indicative of the absence of a direct dependence between friction coefficient and wear resistance. In terms of improvement of adhesion of tram wheels and rails the best result is given by deposited metal of the austenitic class, produced using flux-cored wire PP-Np-OP1, as it has the highest friction coefficient in a pair with metal of M76 steel.

Comparison of friction surfaces after testing showed that there are no significant differences between samples of steel M76 and those clad by wires of the ferritic class. Wear surfaces have deep scratches (Figure 4, *a*, *b*). Surface roughness measured by a probe optico-mechanical profile meter is 50–60 μm.

On samples clad by PP-Np-OP1 wire of austenitic class and having a high wear resistance, a minimum number of scratches is found on the friction surface (Figure 4, *c*), and their roughness is on the level of 5–10 μm.

Investigations showed that metal deposited with PP-Np-OP1 wire has an austenitic structure (Figure 5, *a*), and that deposited by PP-Np-OP2 wire has a ferritic structure with inclusions of fine titanium carbonitrides (Figure 5, *b*).

Hardness of the austenitic deposited metal is *HV* 200–230, but under the impact loads applied to rails in service it rises to *HV* 500–530. Ferritic deposited metal has hardness *HV* 170–195, and its values

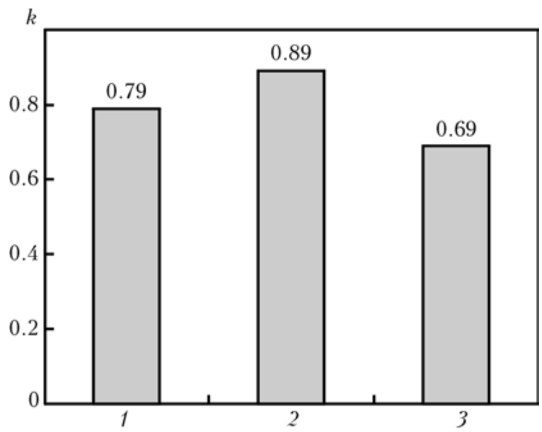

Figure 3. Friction coefficients of mating body of steel M76 + M76 (*1*), M76 + austenitic metal (*2*), and M76 + ferritic metal (*3*)

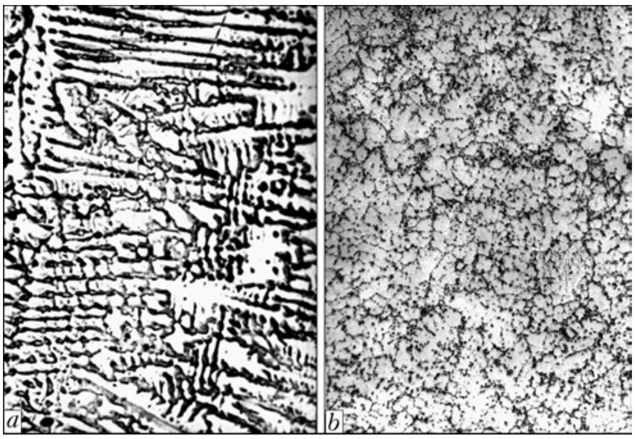

Figure 5. Mictrostructure of metal deposited by flux-cored wires PP-Np-OP1 (*a*) and PP-Np-OP2 (*b*) (×500)

are unchanged after the impact load application. The higher wear resistance of austenitic deposited metal is attributable to its ability to strengthen in service.

Thus, investigations of tribotechnical characteristics at dry friction of metal sliding over metal showed that deposited metal of austenitic class has the best set of properties. A possible cause for a higher wear resistance of austenitic metal is its ability to strengthen in operation.

1. Kalensky, V.K., Chernyak, Ya.P., Pritula, S.I. (1999) Repair hardfacing of worn tramway rails. *Svarshchik*, **2**, 5.
2. Sosyants, V.G. (1965) *Urban tracks and roads*. Moscow: Strojizdat.
3. Ryabtsev, I.I., Chernyak, Ya.P., Osin, V.V. (2004) Modular unit for testing deposited metal. *Svarshchik*, **1**, 18–19.

SANITARY AND HYGIENIC CHARACTERISTICS OF COVERED ELECTRODES FOR WELDING HIGH-ALLOY STEELS

K.A. YUSHCHENKO, O.G. LEVCHENKO, A.V. BULAT, O.N. BEZUSHKO, V.I. SAMOJLENKO and **V.V. MISECHKO**

E.O. Paton Electric Welding Institute, NASU, Kiev, Ukraine

Results of investigation of hygienic characteristics of fumes formed in covered-electrode welding of high-alloy chromium-nickel steels are presented. It is shown that they are determined by the content of alloying elements in electrode rod and covering, type of electrode covering, method of deoxidising-alloying of the weld metal, and composition of a gas-slag forming base of coverings. The level of emissions and toxicity of welding fumes can be decreased by changing the above factors.

Keywords: arc welding, high-alloy steels, covered electrodes, welding fumes, chemical composition, toxicity

Arc welding of high-alloy chromium-nickel steels is characterised by pollution of air of the work zone with the welding fumes (WF), which contain materials of different hazard classes (GOST 12.1.005–88) that are harmful for human organism: I — hexavalent chromium and nickel, II — manganese and soluble fluorides, III — trivalent chromium and insoluble fluorides. Minimising the WF emissions and their most toxic components is a pressing problem, which has to be solved both at a stage of development of new welding electrodes, and during the process of their utilisation.

This study is dedicated to hygienic evaluation of known and new grades of covered electrodes intended for welding of high-alloy steels, as well as to finding of methods for decreasing toxicity of WF.

Sampling of WF for the hygienic evaluation of electrodes was made during the deposition of beads on plates of steel Kh18N10T using known electrodes. Rectifier VDU-504 was utilised as a power source for the welding arc. The deposition was performed at a direct current of reversed polarity under optimal conditions. Welding fumes were entrapped by using a special cover that isolated the welding zone. According to technical specifications [1, 2], WF were precipitated on the FPP-15-1.5 fabric filters to evaluate the level of emissions, and on the AFA-KhA-18 filters for further chemical analysis of the WF samples. Mass of the emitted WF and their components was determined by the gravimetric method, for which not less than five WF samples were taken. The investigation results were subjected to statistical processing [3].

The level of WF emissions is determined by two indicators: intensity of their formation V_f (g / min) and specific emission G_f (g / kg). Toxicity of WF was calculated by the IIW procedure [4, 5] using such an indicator as the maximum permissible concentration of WF, TLV_f (mg / m^3):

$$TLV_f = \frac{100}{\dfrac{C_1}{TLV_1} + \dfrac{C_2}{TLV_2} + \ldots + \dfrac{C_i}{TLV_i}},$$

where $C_1, C_2, \ldots, C_i$ are the contents of the 1st, 2nd, ... and i-th component in WF, wt.%; and TLV_1, TLV_2, ..., TLV_i are the maximum permissible concentrations of these components in air of the work zone (toxicity indicator), mg / m^3.

Note that toxicity of WF decreases with increase in TLV_f. Such an indicator as the nominal hygienic limit of air exchange, NHL (m^3 / h), was used as a general criterion of the level of WF emission and toxicity:

$$NHL = V_f / TLV_f.$$

According to technical specifications [2], the presence of materials containing manganese, nickel and titanium in WF compositions is presented in the form of chemical elements, i.e. chromium compounds converted into CrO_3 and Cr_2O_3, and soluble and insoluble fluorides, F_{sol} and F_{insol}, respectively, converted into fluorine. Because the procedure specified in [2] fails to determine the content of all components of the WF,

Table 1. Structural peculiarities of coverings of electrodes for manual arc welding of high-alloy corrosion-resistant steels and joints on dissimilar steels

Electrode grade (diameter, mm)	Electrode type (GOST 10052–75)	Type of electrode covering (GOST 9466–75)	Method for deoxidising-alloying of weld metal	Gas- and slag-forming base of covering
OZL-6 (3.0)	E-10Kh25N13G2	Basic	Through electrode rod and covering	CaF_2–$CaCO_3$
ANV-70B (3.0)		Same		CaF_2–$CaCO_3$
ANV-70B (4.0)		»		CaF_2–$CaCO_3$
FOX FF (4.0)		»		CaF_2–$CaCO_3$
FOX FFÀ (4.0)		Rutile-basic		CaF_2–$CaCO_3$
				ÒiO$_2$–CaF_2–$CaCO_3$
ANV-66 (3.0)	E-10Kh20N9G6S	Basic	With chromium and nickel through rod and covering, with manganese through covering, with chromium, nickel and manganese through rod	CaF_2–$CaCO_3$
ANV-66 (4.0)				CaF_2–$CaCO_3$
NII-48G (4.0)				CaF_2–$CaCO_3$
ANV017u (3.0)	E-02Kh19N18G5AM3	Rutile-basic	Through electrode rod	ÒiO$_2$–CaF_2--Cr_2O_3
ANV-17 (3.0)	E-02Kh19N18G5AM3	Same		ÒiO$_2$–CaF_2--Cr_2O_3
NZh-13 (3.0)	E-09Kh19N10G2M2B	Basic		CaF_2–$CaCO_3$
EA-400 / 10u (3.0)	E-07Kh19N11M3G2F	Same		CaF_2–$CaCO_3$
ANV-65u (3.0)	E-08Kh20N9G2B	Basic	Through electrode rod and covering	CaF_2–$CaCO_3$
TsL-11 (3.0)		Same		CaF_2–$CaCO_3$
INOX B 19 / 9Nb (3.25)		Rutile-basic		ÒiO$_2$–CaF_2–$CaCO_3$
OZL-8 (3.0)	E-07Kh20N9	Basic	Through electrode rod and covering	CaF_2–$CaCO_3$
ANV-57 (3.0)		Same	Through electrode covering	CaF_2–$CaCO_3$
ANV-29 (3.0)		Rutile-basic	Through electrode rod and covering	ÒiO$_2$–CaF_2–$CaCO_3$

Note. Electrodes NZh-13 and EA-400 / 10u are analogues to electrodes ANV-17 in their purpose.

the following assumption was made to reduce their content to 100 %: the balance of WF, except for the revealed components, consists of iron oxides.

For convenience of interpretation of the test results, the electrode characteristics given in Table 1 were divided by the type of the deposited metal, type of the gas- and slag-forming base of a covering, and method for deoxidising-alloying of the weld metal.

As shown by the results of determination of chemical composition, intensity and specific emissions of welding fumes (Tables 2–4), the total content of trivalent and hexavalent chromium, nickel, manganese and fluorides in the WF increases with increase in the content of the above elements in electrodes. At the same time, it is established that the higher the content of manganese (hazard class II) in the deposited metal and, accordingly, in WF, the lower the content of carcinogenic hexavalent chromium (hazard class I) in WF. This is attributable to a reducing effect of manganese by reaction: $CrO_3 + 3Mn \rightarrow Cr_2O_3 + 3MnO$. It can be seen by an example of electrodes ANV-17 and ANV-17u that, if the weld metal is alloyed with

Table 2. Chemical composition of welding fumes (wt.%)

Electrode grade (diameter, mm)	CrO_3	Cr_2O_3	Mn	Ni	F_{sol}	F_{insol}
OZL-6 (3.0)	4.01	4.30	2.36	0.90	5.57	4.50
ANV-70B (3.0)	4.23	6.53	3.10	0.50	5.83	4.90
ANV-70B (4.0)	–	–	–	–	--	–
FOX FF (4.0)	4.35	2.95	1.71	0.36	6.23	5.60
FOX FFÀ (4.0)	8.07	2.52	1.86	2.52	5.36	0.24
ANV-66 (3.0)	3.45	4.52	4.16	0.50	6.96	3.41
ANV-66 (4.0)	–	–	–	–	--	–
NII-48G (4.0)	4.65	0.47	5.14	1.73	6.50	6.25
ANV-17u (3.0)	1.56	4.40	6.50	1.70	5.23	1.26
ANV-17 (3.0)	1.56	4.65	6.82	3.40	4.01	2.73
NZh-13 (3.0)	5.23	1.68	2.42	1.83	4.43	5.86
EA-400 / 10u (3.0)	3.92	2.40	4.14	1.44	4.41	5.59
ANV-65u (3.0)	3.56	4.66	3.86	0.50	6.21	4.67
TsL-11 (3.0)	4.61	2.49	2.93	2.44	4.77	4.87
INOX B 19 / 9Nb (3.25)	5.10	1.32	2.84	1.43	6.27	3.78
OZL-8 (3.0)	3.80	4.25	3.30	0.49	4.94	5.70
ANV-57 (3.0)	4.00	4.20	5.87	1.21	7.50	4.71
ANV-29 (3.0)	2.90	4.21	4.03	1.26	5.94	1.66

Table 3. Intensity of formation (g / min) of welding fumes and their components

Electrode grade (diameter, mm)	CA	CrO_3	Cr_2O_3	Mn	Ni	F_{sol}	F_{insol}
OZL-6 (3.0)	0.397	0.016	0.017	0.009	0.004	0.014	0.018
ANV-70B (3.0)	0.362	0.015	0.023	0.011	0.002	0.021	0.018
ANV-70B (4.0)	0.507	0.021	0.033	0.016	0.003	0.030	0.025
FOX FF (4.0)	0.458	0.020	0.014	0.008	0.0016	0.029	0.026
FOX FFÀ (4.0)	0.624	0.051	0.016	0.012	0.016	0.040	0.0015
ANV-66 (3.0)	0.385	0.013	0.017	0.027	0.002	0.027	0.013
ANV-66 (4.0)	0.550	0.019	0.025	0.023	0.003	0.038	0.019
NII-48G (4.0)	0.462	0.021	0.003	0.028	0.001	0.036	0.034
ANV-17u (3.0)	0.305	0.005	0.013	0.020	0.005	0.016	0.003
ANV-17 (3.0)	0.369	0.006	0.017	0.025	0.013	0.015	0.010
NZh-13 (3.0)	0.309	0.016	0.005	0.007	0.006	0.014	0.018
EA-400 / 10u (3.0)	0.343	0.013	0.008	0.014	0.005	0.015	0.019
ANV-65u (3.0)	0.318	0.011	0.015	0.012	0.002	0.020	0.015
TsL-11 (3.0)	0.257	0.012	0.006	0.007	0.006	0.012	0.013
INOX B 19 / 9Nb (3.25)	0.319	0.016	0.004	0.009	0.005	0.020	0.012
OZL-8 (3.0)	0.293	0.011	0.012	0.009	0.001	0.014	0.017
ANV-57 (3.0)	0.400	0.016	0.017	0.023	0.005	0.030	0.019
ANV-29 (3.0)	0.315	0.009	0.013	0.012	0.004	0.019	0.003

manganese only through the electrode rod, its content of WF amounts to maximal values (6.50 and 6.82 wt.%, respectively), whereas the content of hexavalent chromium is minimal (1.56 wt.%).

Analysis of the obtained results shows (see Tables 2–4) that the type of the electrode covering has a substantial effect on the level of emissions of fluorides: the content of fluorides, especially insoluble, decreases for electrodes with the rutile-basic type of coverings. For example, in welding with electrodes ANV-2u, ANV-17u and ANV-17, the content of insoluble fluorides and indicators of the level of their emissions are minimal.

Utilisation of electrodes of the same grade but of a larger diameter, as well as increase of the welding current, leads to a more intensive formation of WF (see Table 2, electrodes ANV-70B and ANV-66 with 3 and 4 mm diameter).

Analysis of the results of evaluation of toxicity of the WF by the TLV_f indicator (Table 5) shows that its values vary from 0.10 to 0.35 mg / m^3 for different electrode grades. WF formed in welding with electrodes of the FOX FFA grades (TLV_f = 0.10 mg / m^3) have maximal toxicity, and those formed in welding with electrodes ANV-17u and ANV-17 (TLV_f = = 0.35 mg / m^3) have minimal toxicity. Based on the composition of the deposited metal, this can be explained, first of all, by a lower chromium content of electrodes ANV-17u and ANV-17, compared with electrodes FOX FFA. Chemical analysis results (see Table 2) confirm that the WF formed in welding with electrodes ANV-17u and ANV-17 also have a minimal

Table 4. Specific emissions (g / kg) of welding fumes and their components

Electrode grade (diameter, mm)	CA	CrO_3	Cr_2O_3	Mn	Ni	F_{sol}	F_{insol}
OZL-6 (3.0)	17.16	0.68	0.73	0.40	0.15	0.61	0.77
ANV-70B (3.0)	13.58	0.57	0.88	0.42	0.07	0.79	0.66
ANV-70B (4.0)	13.40	0.57	0.88	0.42	0.07	0.78	0.66
FOX FF (4.0)	11.40	0.50	0.34	0.19	0.04	0.71	0.64
FOX FFÀ (4.0)	14.54	1.17	0.37	0.27	0.37	0.92	0.035
ANV-66 (3.0)	12.98	0.45	0.59	0.93	0.06	0.90	0.44
ANV-66 (4.0)	13.61	0.47	0.62	0.57	0.07	0.95	0.46
NII-48G (4.0)	11.98	0.63	0.064	0.70	0.24	0.88	0.85
ANV-17u (3.0)	10.47	0.17	0.46	0.68	0.17	0.55	0.09
ANV-17 (3.0)	12.18	0.19	0.57	0.83	0.41	0.49	0.33
NZh-13 (3.0)	10.63	0.56	0.18	0.26	0.19	0.47	0.62
EA-400 / 10u (3.0)	12.05	0.47	0.29	0.50	0.17	0.53	0.67
ANV-65u (3.0)	10.81	0.38	0.50	0.42	0.05	0.67	0.50
TsL-11 (3.0)	10.48	0.48	0.26	0.31	0.26	0.50	0.51
INOX B 19 / 9Nb (3.25)	11.85	0.60	0.16	0.34	0.17	0.74	0.45
OZL-8 (3.0)	10.44	0.40	0.44	0.34	0.05	0.52	0.59
ANV-57 (3.0)	17.36	0.69	0.73	1.02	0.21	1.30	0.82
ANV-29 (3.0)	11.39	0.33	0.48	0.46	0.14	0.67	0.06

Table 5. Indicators of toxicity TLV_f of welding fumes and air exchange NHL

Electrode grade (diameter, mm)	TLV_f, mg / m^3	NHL, m^3 / h
OZL-6 (3.0)	0.20	1780
ANV-70B (3.0)	0.20	1840
ANV-70B (4.0)	0.20	2570
FOX FF (4.0)	0.20	2340
FOX FFÀ (4.0)	0.10	5670
ANV-66 (3.0)	0.20	1670
ANV-66 (4.0)	0.20	2390
NII-48G (4.0)	0.15	2700
ANV-17u (3.0)	0.35	820
ANV-17 (3.0)	0.35	1110
NZh-13 (3.0)	0.15	1920
EA-400 / 10u (3.0)	0.20	1680
ANV-65u (3.0)	0.20	1410
TsL-11 (3.0)	0.15	1480
INOX B 19 / 9Nb (3.25)	0.15	1930
OZL-8 (3.0)	0.20	1340
ANV-57 (3.0)	0.20	2060
ANV-29 (3.0)	0.25	1220

content of hexavalent chromium, which affects toxicity of the fumes. Another important factor [6] determining transfer of alloying elements to WF is the method for deoxidising-alloying of the weld metal. The point of the method is that alloying through the electrode rod provides a lower transfer of the said elements to WF, compared with alloying through the electrode covering. In the case of using electrodes ANV-17u and ANV-17, alloying of the weld metal occurs through the electrode rod, and with electrodes FOX FFA –– through the rod and covering.

As electrodes of the same grade, e.g. ANV-66, and different diameters (3 and 4 mm) have identical toxicity indicator TLV_f (see Table 5), but different indicators of the level of emissions, V_f and G_f, for a more correct comparative hygienic evaluation it is expedient to use the generalised indicator of toxicity and level of emissions of WF, i.e. NHL [4, 5]. Therefore, this indicator (Table 5) for electrodes of the same grade (ANV-66) with a diameter of 3 mm is 1670 m^3 / h, while for a diameter of 4 mm it has a higher value –– 2390 m^3 / h. For electrodes ANV-17u and ANV-17, having the identical relative toxicity (TLV_f = 0.35 mg / m^3), indicator NHL is lower for electrodes of the first grade (1110 m^3 / h) than for the second grade (820 m^3 / h).

Therefore, allowing for all hygienic indicators of the electrodes studied, it can be concluded that electrodes of the ANV-17u type are characterised by the best hygienic characteristics among the other electrodes tested.

CONCLUSIONS

1. New electrodes of the ANV-17u, ANV-65u, ANV-70B and ANV-66 grades are at a level of the best domestic and foreign analogues in their hygienic characteristics.

2. In welding of high-alloy chromium-nickel steels, the best hygienic characteristics are exhibited by the electrodes with rutile-basic coverings, when alloying of the weld metal occurs through the rod.

3. Increase of the weight content of manganese in electrode rods leads to decrease of the content of carcinogenic hexavalent chromium (hazard class I) in WF, which is caused by its reduction by manganese to the trivalent state (hazard class III).

4. The intensity of formation of WF grows with increase of the diameter of electrodes and, accordingly, welding current.

5. Selection and development of new grades of electrodes for welding high-alloy steels should be based on the mandatory primary hygienic evaluation using the IIW procedure, allowing for the indicators of chemical composition, level of emissions and toxicity of the formed WF.

6. Availability of the systems of local ventilation and general ventilation by dilution is the mandatory condition for utilisation of electrodes for welding of high-alloy chromium-nickel steels. The obtained results of hygienic evaluation of electrodes should be taken into account in selection and calculation of capacity of the ventilation systems.

1. *MU 1927–78*: Procedural recommendations. Hygienic evaluation of consumables and methods for welding, surfacing and cutting. Moscow: Minzdrav SSSR.
2. *MU 4945–88*: Procedural recommendations for determination of harmful materials in welding fume (solid phase and gases). Moscow: Minzdrav SSSR.
3. Pollard, J. (1982) *Reference book on computational methods of statistics*. Ed. by E.M. Chetyrkin. Moscow: Finansy i statistika.
4. Criteria for classification of MMA welding electrodes regarding fume. *IIW Doc. II-E-820--77; IIW Doc. II-E-256–78*.
5. Magnusson, E.J., Rosendahl, C.H. Studies of the possibilities of classifying welding electrodes according to fume generation. *IIW Doc. II-E-301–80*.
6. Golovatyuk, A.P., Lipodaev, V.N., Zakharov, L.S. (1976) Comparative hygienic evaluation of electrodes for welding of high-alloy steels. *Avtomatich. Svarka*, **3**, 61--63.

ROBOTIC STATION FOR WELDING GLOBE VALVES IN Ar + CO_2 GAS MIXTURE ATMOSPHERE

V.M. ILYUSHENKO, G.A. BUTAKOV and **A.V. GANCHUK**
E.O. Paton Electric Welding Institute, NASU, Kiev, Ukraine

Described is a robotic station for welding globe valves, which includes a workpiece rotator. Synchronising the rotator operation with the RM-01 robot manipulator is provided by using the «Sfera-36» control system devices. The station was tested by the E.O. Paton Electric Welding Institute.

K e y w o r d s : arc welding, robotic station, workpiece rotator, control system, globe valve

Five circumferential welds are required to make a globe valve. Manual welding methods fail to provide the required productivity and quality of manufacture of this structure in mass production of the valves. As the joints are in different spatial positions, and the technology provides for welding with small-amplitude oscillations of the arc across a joint, it is expedient to apply robotic work stations. Manufacturing enterprises have now a sufficiently big amount of welding robots RM-01 equipped with the «Sfera-36» control system. A drawback of this type of robots is the absence of the possibility of circular interpolation. However, in this case this drawback is insignificant, as welding is performed with orientation of the mating surfaces at an angle of 45° to the welding tool and rotation of a workpiece (gravity welding), the torch being in the fixed spatial position and oscillating across the joint at an amplitude of 1.5 mm and frequency of 3 Hz.

Workpiece manipulator (rotator) is equipped with a chuck-type clamp. Rotation is provided by the 250 W DC motor. The rotation speed is adjusted and set manually before welding.

Synchronising the time of the welding start and finish with switching on and off of rotation of a workpiece is ensured by using the robot control system. Inductive sensor of the TSL type is used as a sensor of angular position of the workpiece. For this, a metal disk with four slots is mounted on the rotator motor shaft. A pulse signal is generated when a disk blade passes through the sensitivity zone of the inductive sensor. This signal is fed to the initiator input of the robot control system and processed as an interrupt signal. The pulse repetition frequency is directly proportional to the rotation speed of the rotator motor shaft, and quantity of the pulses is proportional to the angle of turning of the workpiece relative to the welding start point. The quantity of the pulses for a complete revolution is 256 at a transfer ratio of the step-down reduction gear from the motor shaft to the clamping chuck equal to 64 / 1, i.e. an error in determination of the angular position is no more than 1.4°. The largest diameter of the circumferential weld in this structure of the valve is 60 mm.

Therefore, the error in determination of linear displacement is not in excess of 0.75 mm, which provides the required accuracy for achieving the set overlap value. Upon accumulating the set quantity of the pulses corresponding to a rotation of the workpiece to 365° (overlap of 5°), the robot control system switches off the welding process, stops the rotator and moves the welding tool from the workpiece to the

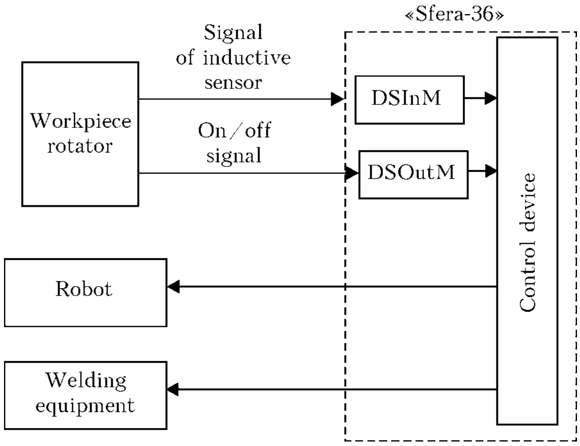

Figure 1. Structural scheme of the workpiece rotator–«Sfera-36» system: DSInM and DSOutM — discrete signal input module and discrete signal output module, respectively

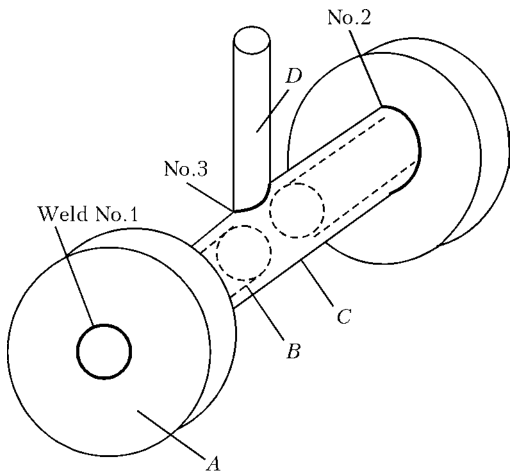

Figure 2. Schematic of globe valve and locations of joints in it

Figure 3. Appearance of the embedded tube to flange joint

initial position. Structural scheme of the workpiece rotator–«Sfera-36» system is shown in Figure 1.

Welding of a globe valve is performed in the following sequence (Figure 2): welding of flanges *A* to embedded tubes *B* (weld 1), assembly of the valve and sequential welding of welds 2 (welding of flanges *A* to casing tube *C*), and welding of stop mechanism *D* into casing tube *C* (weld 3).

Making of weld 3 causes the highest difficulties. The line of a joint is a complex spatial curve, i.e. intersection of two cylinders having different diameters. As noted above, robot RM-01 provides only linear interpolation in point-to-point movement. Therefore, 12 equidistant points were selected on the trajectory of weld 3 for teaching, and linear interpolation was used in the point-to-point movement. In welding with oscillations across the joint line, an error in movement on the linearly interpolated trajectory has almost no effect on the final result.

The following welding equipment was used to fit the robotic station: power unit VD-506 DK, welding wire feed mechanism PDGO-511 with welding torch «Binzel», and local fume suction device «Filtr-200». All the welds were made under the same conditions: current 180 A, electrode wire diameter 1 mm, oscillation amplitude 1.5 mm, oscillation frequency 3 Hz, and welding speed 12 m / h.

Robotic station RM-01 passed the tests at the E.O. Paton Electric Welding Institute in welding of globe valves (Figure 3), and showed the acceptable quality of all the welds. The time of welding one valve is about 10 min.

NEWS

NKMZ BECAME A WINNER OF THE XII NATIONAL QUALITY CONTEST

At the XVI International Forum «Days of Quality in Kiev – 2007», which was held within the frames of the European Quality Week in Ukraine, the Novokramatorsk Machine Building Works (NKMZ Company, Kramatorsk, Donetsk District) was declared a winner of the XII National Quality Contest in nomination «Large Businesses», and became a holder of certificate «Acknowledgement of Excellence in Europe — Five Stars» of the European Quality Control Foundation. Other participants of this nomination — Kryukovsky Wagon Works, Mining and Metallurgy Complex «Arcellor Mittal Krivoj Rog», and Electric Machine Building Factory «SELMA» (Simferopol) — were given the titles of laureates.

While presenting the gold mark and certificate, the President of the Ukrainian Quality Association Petr Kalita emphasised that the Novokramatorsk Machine Building Works is the only company among the Ukrainian large businesses that came right to the level of the best companies of Central and East Europe, which is determined according to the criteria of the Business Excellence Model of the European Quality Control Foundation. Now NKMZ will participate in the European Quality Contest, the participants of which are such internationally known companies as Nokia, Volkswagen, Volvo and Danieli. The purpose of the enterprise is to obtain certificate «Finalist of the European Quality Prize».

THESIS FOR SCIENTIFIC DEGREE

S.O. Admiral Makarov Shipbuilding National Institute

On the 9th of October 2007 **O.N. Druz** (The V.Dal East-Ukrainian National University) defended the thesis of Ñandidate of Sciences (Engineering) on the subject «Regulation of Welded Joint Properties by Means of Complex Shielding Medium».

The thesis is devoted to the subject of controlling the dimensions of plastic deformation zone, HAZ, weld geometry, residual deformation level, welded joint properties using a complex shielding medium (CSM). The possibility of using CSM in the form of a dispersed system, as a quenching agent and as a shielding medium, is considered in the study. Welding-technological properties of CSM, consisting of 25–10 % of surfactant water solution and 75–90 % of filler gas, were investigated. «PEGAS» substance (GOST 3789–98) was used as surfactant, which contains 1.5 % of sodium olein-sulfonates, 0.2–0.4 % of corrosion inhibitors (twice- and thrice substituted sodium phosphates), 16 % of carbamide Air, CO_2, Ar, O_2 and their mixtures were used as filler gas. Water solution minerals NaCl, KCl, KC1·NaCl, $CaCl_2$, Na_2CO_3, K_2CO_3 were added to surfactant solution to raise arc stability.

Equipment for making CSM and fixture for welding in CSM were designed on the base of L.V. Ivanov dispersion device.

Complex quality index by GOST 15467–79, with application of weightiness coefficient of each index of CSM welding-technological characteristic, was used for selection of optimal CSM composition.

Study of CSM properties showed the possibility of its use as an effective quenching agent due to the presence of the liquid phase in its composition. Here, the cooling rate of the $300 \times 200 \times 5$ mm metal plate was 21–25 °C / s in the temperature range of 800–500 °C.

Equation of the coefficient of surface heat dissipation, used for heat propagation modelling in the plate in welding in CSM with not more than 10 % error, was obtained on the base of experimental investigations. Modelling was carried out by means of applied program package based on finite element analysis. It was experimentally established that the surface heat dissipation coefficient is in the range from 0.006 to 0.025 W / ($cm^2 \cdot$°C) in CSM, depending on the multiplicity.

Design dependences between the properties of welded joint and hardness of its different parts were established. For modeling the HAZ sections hardness in welding in CSM, B.D. Lebedev's model was improved that had the error of not more than 2.5 %.

Technology of automatic welding in CSM was designed and studied. It was determined that CSM is an active oxidative medium.

CSM cooling effect allows decreasing the width of plastic deformation zone by 30 % when CSM is applied from one side. HAZ dimensions are reduced by 14 % on average when welding plug lap joints in CSM.

The effect of activation of the arc penetrability was studied. The deepest penetration was obtained with CSM of 20–30 composition ratio: No. 1 — 8 % surfactant water solution, and air as filler gas; and No. 11 — 8 % surfactant water solution, and Ar as filler gas. The lowest HAZ value was obtained with compositions: No. 13 — 10 % surfactant water solution + 5 % Cl solution, Ar as filler gas; and No. 5 — 8 % surfactant water solution + 10 % Na_2CO_3 + 10 % KCO_3 with air as filler gas. The most adaptable-to-fabrication are the arcs were determined in accordance with welding arcs classification by V.A. Lenivkin and by maximum value of complex quality index, that were obtained with the following compositions: No. 16 — 10 % surfactant water solution + 8 % Cl solution, CO_2 as filler gas; and No. 12 — 100 % surfactant water solution, and Ar as filler gas.

Mechanical properties of welded joints obtained in CSM welding were studied. It is established that the joint properties in CSM welding are not inferior to those of the joints in CO_2 welding.

Economic effect from CSM application is predicted based on decrease of shielding gas consumption and using of activation effect of arc penetrability that allows increasing the depth of penetration by 20 % without change of welding technological modes and lowering of the cost of post-welding straightening.

WELDEX / ROSSVARKA-2007

The 7th International specialized exhibition «Welding Materials, Equipment and Technologies» was held in Moscow in Center «Sokolniki» from October 30 to November 2, 2007. CJSC «International Exhibition Company» with the support of Center «Sokolniki», National Agency of Control and Welding (NACW), Moscow Interbranch Association of Chief Welders, Russian Scientific and Engineering Welding Society, Russian Union of Developers and Manufacturers of Welding Production, and «Elsvar» company were organizers of the Exhibition.

The results of the passing year and trends for future development for the coming year are traditionally summed up in Russia in Autumn. Regular Exhibition of Weldex / Rossvarka reflects, in this aspect, the achievements for the passed period and promising developments in the general system of welding production quality management, including consumables, structures, welding equipment, welding technologies, control, and personnel.

In 2006 the Weldex / Rossvarka Exhibition received the symbol of Russian Union of Exhibitions and Fairs confirming the high level of exhibition organization, its serious contribution into development of the regions economy and Russia foreign economic relations. In 2007 the Exhibition continued its development and demonstrated its leadership among welding exhibitions of Russia and CIS. It is one of the major specialized welding exhibitions in the world by right. Compared with 2006, the total exposition areas increased by more than 40 %, and practically all the leading Russian and many foreign manufacturers of welding products were presented among its participants. The number of exhibitors at the exhibition was more than 210, and they represented 14 countries from CIS, Europe and Asia, including about 50 mass media booths.

The following should be mentioned as the general impressions from the Exhibition:

• good organization, diverse booth design;

• high attendance, including managers of enterprises and companies, head and chief specialists of technical services of organizations, lecturers from Moscow institutes of higher education and from many regions of Russia;

• variety and saturation of events program, including the functioning of labor exchange for workers, engineers and welding scientists; conducting «Russia Miss Welding», «The Best Welder», «Young Welding Star», and «The Best Welding Engineer» competitions; demonstration of artistic decorative items made by forging and welding methods and other.

It is becoming a tradition that a great part of exhibitors (more than 20 %) are represented at the Exhibition by trade companies and representatives in Russia of such well known brands in the welding world as ESAB, Avesta Welding (Sweden), Fronius, Boehller Welding (Austria), Kuka Roboter, Messer Cutting and Welding, Mercle, Abicor Binzel (Germany), Polisud (France), Lincoln Electric (USA), Cebora, Telvin, Techna (Italy), Askaniak (Turkey), Kemppi (Finland) and other.

Manufacturers of diverse modern equipment for arc welding, cutting and spraying and their commercial representatives were widely represented at the last Exhibition. Abicor Binzel, Weber Comechanic, Weldtech, Gazsrtojservis, Invertor-Plus, Iskra, NPF ITS, ZONT, KZESO, Kemppi, Kuka Roboter, Linde Gas, Navko-Tekh, NGS-Complect, Midasot, Svarka i Tekhnika, Svarog, Spetselektrod, Tekhmash, Technotron, Shtorm ITS, Electric Mix, Electric-complect, ESAB and other were among them. Many of them demonstrated lines of modern welding equipment for manual, mechanized and automatic arc welding, installations for thermal and plasma cutting, surfacing and spraying.

Specimens of high quality coated electrodes, solid wires and strips, flux-cored wires and flux strips were presented in the welding consumable manufacturers' booths. Exhibits of Mezhgosmetiz-Mtsensk, Vistek, Boehler Welding, Volgodonsk, Losinoostrovsk and Zelinograd Electrode Plants, SiBES, Sudislav and Ural Plants of welding consumables, UTP, Sudokey and ESAB should also be mentioned here.

Presentation of Sudokey (Belgium) Company was held during the technical seminar at the Exhibition. The Company specializes as part of Boehler Welding Group, in scientific studies, manufacturing and sale of flux-cored wires of wide range for repair and manufacturing hardfacing of tools and mechanisms in mining, steel and cement industries, press industry, as well as metal strips of different chemical composition for electroslag and submerged-arc cladding to produce special properties of clad surfaces.

Ukraine was presented at the exhibition by the displays of PWI, ZONT and Tekhmash (Odessa), DONMET Plant (Kramatorsk), KZESO (Kakhovka) Kommunar (Kharkov), Navko-Tekh (Kiev), Vistek (Artyomovsk), Tekhvagonmash (Kremenchug). As to PWI booth, the visitors of the Exhibition expressed the highest interest in such technology developments as friction stir welding (FSW), EBW, equipment for flash-butt welding, welding of live tissues, developments in the field of surfacing consumables and other. A number of preliminary proposals were discussed on carrying out contract works with the Institute.

Reporting-Election Conference of the Russian Scientific-Technical Welding Society (RSTWS) where representatives from almost all regions of Russia were present, was held in the frame of the Exhibition.

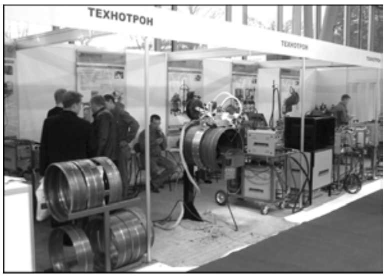

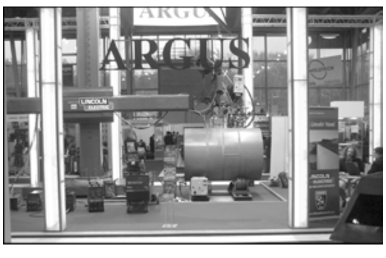

RSTWS work for the previous period was analyzed, the strong and weak points were noted and the main future goals were determined at the Conference. In addition, RSTWS President was re-elected on a competitive basis, and professor O.I. Steklov became the Society President.

Round-table meeting of NAKS took place on November 2 as part of the Exhibition, where the problems of certification and approval of welding equipment, welding consumables and personnel, as well as problems of development of national welding standards were touched upon in frank and business discussions. It was generally agreed by all the round table participants that this meeting was very useful.

A number of competitions were carried out in the frame of the Exhibition. Special mention should be made of the achievements of Dmitrii Kushniruk, the PWI welder, an artist at heart. Dmitrii rightfully took the 1st place in the competition «The Best Welder — Mister Beam 2007» in the nomination of «TIG Welding». He was awarded the Certificate of the winner and a valuable prize (power converter of ESAB company). Congratulations to Dmitrii Kushniruk! The 2nd place was awarded to G.I. Gruzdova (OJSC «Novokujbushev NPZ»).

The winners in the nomination of «Manual Arc Welding with Coated Electrodes» were: 1st place — V.V. Uteshov («RN-«Yuganskneftegaz», Nefteyugansk); 2nd place — V.A. Tudvasev (OJSC «Atommashexport», Volgodonsk). T.V. Predeina (Yurginsk Technological Institute) won in the nomination of «Young Welding Star».

The competition for «The Best Welding Engineer» was conducted in two nominations. Professor A.V. Konovalov from the N.E. Bauman MSTU was recognized as the winner for development of a «System of computer analysis of alloyed steel weldabitity» in the nomination of «The Best Welding Scientist», and A.V. Bazhanov, specialist of the K.E. Tsiolkovsky MATI — for development of compact light-beam unit «Luch-3M» in the nomination of «The Best Welding Designer».

In conclusion it should be noted that Exhibition-2007 in Sokolniki demonstrated obvious progress in the field of welding fabrication in Russia and increased interest to it both from the side of visitors and from foreign companies.

V.N. Lipodaev, Doctor of Tech. Eng. Sci.
A.T. Zelnichenko, Cand. of PhMath. Sci., PWI

Interindustry Training-Attestation Center of the E.O. Paton Electric Welding Institute of the NAS of Ukraine ITAC Professional Training Programs for 2008

Course code	Program description			Number of hours	Dates
1. Improvement of qualifications of engineering-technical personnel (with qualification for the right of technical supervision of work in fabrication of critical welded structures including those performed under control of the state supervision authorities)					
101	Technical supervision of welding operations in the facilities under state supervision		Training and certification	3 weeks (112 h)	March
102			Re-certification	18 h	January, March, June, November
103	Technical supervision of welding-mounting work in construction and repair of gas pipelines from polyethylene pipes		Training and certification	2 weeks (72 h)	May, November
104			Re-certification	1 week (32 h)	March, December
105	Training and certification of Heads of Commissions on certification of welders-experts of Ukrainian Committee on Welder Certification (UCWC)			3 weeks (112 h)	December
106	Certification of Heads of Commissions on certification of welders-experts of UCWC (examination; widening the qualification field)			8 h	Upon submission of applications and by agreement with UCWC
107	Training commission members on welder certification:	specialist of technological services responsible for organization of welder certification		2 weeks (72 h)	October
108		specialists of technical control services responsible for welded joint control (including special training for certification on visual-optical control method)		2 weeks (74 h)	Quarterly
109		specialists of enterprise labour safety service		2 week (74 h)	February
110	Certification of members of welder certification commission-specialists of welding technology services (examination, widening of qualification field)			6 h	Upon submission of applications
111	Confirmation of authorities of Commission Chairmen-UCWC specialists:		with 3 year working experience	16 h	September
112			with 6 year working experience	32 h	
113			with 9 year working experience	22 h	October
114			with 12 year working experience		October, November
115	Confirmation of authorities of members of Welder Qualification Commission:	specialists of welding technology services:	with 3 year working experience	16 h	February
116			with 6 year working experience	32 h	September
117			with 6 year working experience	22 h	October
118		technical control specialists		8 h	Quarterly
119		technical control specialists (including special training)		28 h	
120		labour safety specialists		16 h	June
121	Re-training welding production specialists by IIW programs, giving the following qualification:	International Welding Engineer		441 h (112 h[1])	April, November
122		International Welding Technologist		340 h (112 h[1])	
123		International Welding Specialist		222 h (112 h[1])	
124		International Welding Practitioner		146 h (76 h[1])	Upon submission of applications
125		International Welding Inspector (1st, 2nd, 3rd level)		108, 158, 218 h[2]	

131	Training quality control managers for welding fabrication (with issuing of a European certificate)		2 weeks (72 h)	By agreement with the Customer
132	Welding electrode manufacture: organization, technologies and systems of quality control		3 weeks (112 h)	
133	Technical supervision of welding operations in repair of operating pipelines (under pressure)	Certification	2 weeks (72 h)	
134		Re-certification	20 h	
135	Organizing non-destructive testing in railway transportation enterprises		2 weeks (72 h)	Upon submission of applications
136	Metallographic examination of metals and welded joints	Certification	2 weeks (72 h)	July
137		Re-certification	22 h	February, July, October
138	Physical-mechanical testing of materials and welded joints	Improvement of qualifications and qualification examinations	2 weeks (72 h)	May
139		Re-qualification	20 h	May, June
140	Emission spectrum analysis (steeloscopy) of metals and alloys	Certification	2 weeks (74 h)	November
141		Re-certification	22 h	
142	Repair, recoditioning and strengthening of worn parts by cladding methods		70 h	As agreed with the Customer
	Subject-oriented seminars (can be conducted at customer's facility)			
143	Status of codes and standards in the field of welding fabrication, tendencies and prospects		16 h	June, September
144	Modern welding equipment in the Ukrainian market		1 day	Quarterly
145	New technologies of professional training of welders and flaw detection operators			
2. Training and improvement of qualifications of teaching staff of the system of professional-technical training in the field of welding				
201	Training, improvement of qualification of instructors and foremen of industrial training on welding		5 weeks (192 h)	By agreement with customer
202	Improvement of qualifications of lecturers of special welding subjects		3 weeks (112 h)	
3. Professional training, re-training and improvement of personnel qualifications in the field of welding and allied technologies (with qualification in compliance with the national and international requirements)				
	Welder training courses:			
301	Manual coated-electrode arc welding		9 weeks (352 h)	On-going, upon submission of applications
302	Manual inert-gas nonconsumable-electrode arc welding (TIG)		5 weeks (192 h)	
303	Gas welding		3 weeks (116 h)	
304	Mechanized gas-shielded consumable-electrode arc welding (MIG / MAG)		3 weeks (112 h)	
305	Mechanized flux-cored wire arc welding		3 weeks (112 h)	
306	Automatic submerged-arc welding		3 weeks (112 h)	
307	Electroslag welding		3 weeks (112 h)	
308	Resistance (press) welding (rails, production and main oil and gas pipelines)		3 weeks (112 h)	By agreement with the customer
309	Welding of plastics (of pipelines from polyethylene pipes)		5 weeks (196 h)	February, April, July, November
310	By IIW programs with granting the qualification of International Welder		5–12 weeks[2]	By agreement with the Customer
315	Special training on technology and equipment of resistance welding of R-bars		2 weeks (72 h)	
	Welder re-training courses:			

316	Manual coated-electrode arc welding		152 h[3]	On-going, upon submission of applications
317			76 h[3]	
318	Manual inert-gas nonconsumable-electrode arc welding (TIG)		112 h[3]	
319			76 h[3]	
320	Gas welding		76 h	
321	Mechanized gas-shielded consumable-electrode arc welding (MIG / MAG)		76 h	
323	Mechanized flux-cored wire arc welding		76 h	
325	Automatic submerged-arc welding		76 h	
327	Electroslag welding		76 h	
	Improvement of welder qualifications:			
330	Manual coated-electrode arc welding		2 weeks (72 h)	On-going, upon submission of applications
331	Manual inert-gas nonconsumable-electrode arc welding (TIG)		2 weeks (72 h)	
332	Gas welding		2 weeks (72 h)	
333	Mechanized gas-shielded consumable-electrode arc welding (MIG / MAG)		2 weeks (72 h)	
334	Mechanized flux-cored wire arc welding		2 weeks (72 h)	
335	Automatic submerged-arc welding		2 weeks (72 h)	
336	Electroslag welding		2 weeks (72 h)	
339	Improvement of qualifications of gas welders (gas soldering of nonferrous metals)		2 weeks (72 h)	
	Flaw detection operator training courses:			
340	Ultrasonic testing		196 h	On-going, upon submission of applications
341	X-ray and gamma-inspection		188 h	
342	Magnetic inspection		180 h	
	Improvement of qualifications of flaw detection operators:			
346	Ultrasonic testing		104--128 h[4]	On-going, upon submission of applications
349	X-ray and gamma-inspection		104--168 h[4]	
352	Magnetic inspection		104--132 h[4]	
	Purpose-oriented training of flaw detection operators for railway transportation:			
355	Ultrasonic testing		120 h	October On-going, upon forming of teams
356	Magnetic inspection		120 h	
357	Training welding operation controllers		154 h	
	Other professions:			
367	Gas cutter training	Gas cutting	3 weeks (112 h)	On-going, upon forming of teams
368		Manual and mechanized air-plasma cutting	3 weeks (112 h)	
369	Training metallization operators for deposition of strengthening and protective coatings on metals	Arc spraying	3 weeks (112 h)	
370		Gas-flame spraying	3 weeks (112 h)	
371		Detonation spraying	3 weeks (112 h)	
372		Plasma spraying	3 weeks (112 h)	
373	Re-training in the profession «Metal Melter»		72 h	
	4. Certification of welding production personnel (in compliance with national and international standards)			

401	Special training and certification of welders in keeping with DSTU 2444--94, DSTU 2945–94, rules of Gosnadzorokhrantrud (DNAOP 0.00-1.16–96), rules of Gosatomnadzor (PNAEG-7-003–87)		152 h[5]	On-going, upon submission of applications
402			72 h[5]	
403	Additional and extraordinary certification of welders according to DNAOP 0.00-1.16–96		24 h	
404	Periodical certification of welders in keeping with the rules of Gosnanadzorokhrantrud (DNAOP0.00-1.16–96), rules of Gosatomnadzor (PNAE0-7-003–87)		32 h	
405	Special training and certification of welders in compliance with International (or European) standards ISO 9606 (or EN 287)		3 weeks (112 h)	
406			2 weeks (72 h)	
407	Periodical certification of welders in keeping with the International (or European) standards ISO 9606 (or EN 287)		32 h	
408	Special training and certification of welders in compliance with international standard ISO 14732, operators of automatic machines for fusion arc welding / resistance welding machine setters		2 weeks (72 h)	
409	Special training and certification of welders for the right to perform work in repair of acting main pipelines (under pressure)		3 weeks (112 h)	
410	Periodical certification of welders for the right to perform work on repair of acting main pipelines (under pressure)		32 h	
413	Certification of plastic welders (welding of pipelines from polyethylene pipes)		Conducted after completion of course 309	
414	Periodical certification of plastic welders (welding of pipelines from polyethylene pipes)		32 h	January, March, May, June, July, September, December
415	Special training of flaw detection operators for qualification in compliace with DNAOP 0.00-1.27–97	Ultrasonic testing	24 h[6]	Monthly
416–418			60, 70 or 140 h[6]	Quarterly
419		Radiation control	24 h[6]	Monthly
420–422			60, 70 or 140 h[6]	Quarterly
423		Magnetic inspection	24 h[6]	Quarterly
424–425			30 or 60 h[6]	
426			110 h[6]	Once every 6 months
427		Capilllary control	24 h[6]	Once every 6 months
428–429			110 or 60 h[6]	
430		Visual-optical inspection	24 h[6]	Quarterly
431			70 h[6]	
432	Special training and re-certification of flaw detection operators on comprehensive ultrasonic testing of carriage wheel pairs		36 h	Once every 6 months
433	Special training of flaw detection specialists to have the right of work performance in compliance with RD 07.09--97		70 h	
440	Professional aptitude tests for arc welding operators		4–8 h	On-going

[1]Training by alternative (shorter) path.
[2]Training duration is established by Authorized National Body.
[3]Program duration is determined by the results of in-coming testing.
[4]Training duration depends on trainee qualifications.
[5]Training duration is specified by Qualification Commission.
[6]Training duration is indicated in the assignment of personnel qualification body.

As requested by the customer training can be performed in other periods or by other programs not included into this list, and also at the customer facility. Assistance is provided to the trainees to get accommodation for the training period with payment in cash. The cost of training is determined when making the agreement. For enrollment kindly send an application to the Center address with indication of the course code, number of specialists and enterprise postal address.

11, Bozhenko str., 03680, Kyiv-150, Ukraine
Tel.: (+38044) 456–63–30, 456–10–74, 200–82–80, 200–81–09
Fax: (+38044) 456–48–94
E-mail: paton_muac@ukr.net
http: www.paton-tc.kiev.ua

INDEX OF ARTICLES FOR TPWJ'2007, Nos. 1–12

Composite materials

Consumables

Control systems

Controlling electromagnetic field

Evaluation procedures

Fatigue resistance

Fracture resistance

Structure-phase transformations

Surfacing

Treatment

LIST OF AUTHORS